THESIS ON NATURAL AND EXACT SCIENCES B197

Mechanoenergetics of a Single Cardiomyocyte

MARI KALDA

TUT
PRESS

TALLINN UNIVERSITY OF TECHNOLOGY
Institute of Cybernetics
Laboratory of Systems Biology

This dissertation was accepted for the defense of the degree of Doctor of Philosophy (Engineering Physics) on Acceptance time.

Supervisors:	Marko Vendelin, PhD Laboratory of Systems Biology, Institute of Cybernetics, Tallinn University of Technology, Tallinn, Estonia Pearu Peterson, PhD Laboratory of Systems Biology, Institute of Cybernetics, Tallinn University of Technology, Tallinn, Estonia
Opponents:	Alf Månsson, PhD, Prof. Department of Chemistry and Biomedical Sciences, Linnaeus University, Kalmar, Sweden Steven Niederer, PhD Division of Imaging Sciences and Biomedical Engineering, King's College London, London, United Kingdom

Defense of the thesis: December 10, 2015

Declaration:
I hereby declare that this doctoral thesis, submitted for the doctoral degree at Tallinn University of Technology, is my original investigation and achievement and has not been submitted for the defense of any academic degree elsewhere.

Mari Kalda

Colophon: This thesis was typeset with LaTeX 2$_\varepsilon$ using André Miede's *classicthesis* style with modifications by David Schryer and Ardo Illaste to conform with Tallinn University of Technology style guidelines. The main font is Libertine (Times compatible). Biolinum is used for sans-serif text.

ISSN 1406-4723
ISBN 978-9949-23-862-0 (publication)
ISBN 978-9949-23-863-7 (PDF)

LOODUS- JA TÄPPISTEADUSED B197

Ühe südameraku mehaanoenergeetika

MARI KALDA

TTÜ
KIRJASTUS

CONTENTS

SUMMARY

Cardiovascular diseases are one of the major causes of death in the world. To understand what is going on inside the heart one should be able to make conclusions that link the mechanical work done by the heart with the metabolism of the heart. This thesis focuses on that link at the single cell level. Two approaches were used to study this relationship: mathematical modeling and experiments done on isolated cells of an adult mammalian heart.

Mathematical modeling helps to understand the underlying processes involved in the contraction event. Experimental studies on different preparations, from the whole heart to the single cell level, have shown that the energy consumption depends on a certain mechanical index developed during one beat and that relation is independent of contraction mode (isometric, isotonic, physiological). Based on that knowledge, it is possible to estimate the chemical reaction rate constants and other important parameters using the mathematical model of the contracting cell. The contraction process of the cell is found to be cooperative. However, including this cooperativity into the mathematical description has been a problem. This thesis gives a solution how to include cooperativity to a deterministic cross-bridge model in a thermodynamically consistent way.

Using an isolated cell as a sample allows estimating cell properties without the influence of the connective tissue. Also, it gives an opportunity to study cells at a subcellular level. Intact cell experiments are usually performed under unloaded conditions. In this doctoral study, cell contraction experiments were performed under full control of cell lengthening and force generation and, at the same time, biochemical processes were estimated from the fluorescence signal. As part of the design of the experimental setup, an algorithm was developed to estimate the mean sarcomere length from microscopy images in real time.

In summary, the main contribution of this thesis to the field of cardiovascular research is a thermodynamically consistent mathematical description of cardiomyocyte contraction and an experimental setup for single cell experiments with full control over cell loading conditions and the ability to measure biochemical parameters in parallel.

KOKKUVÕTE

SÜDAME JA VERESOONKONNA HAIGUSED on üheks peamiseks surmapõhjuseks kogu maailmas. Sellest tulenevalt on oluline õppida paremini tundma südant töös hoidvaid mehhanisme. Selles doktoritöös on keskendutud südame poolt tehtava mehaanilise töö ja selleks kuluva biokeemilise energia seosele ühe raku tasandil.

Töös on kasutatud kahte uurimismeetodit eelneva seose uurimiseks: matemaatilist modelleerimist ja eksperimetaalsete meetodite rakendamist isoleeritud rakkudel.

Katsed, mis on läbi viidud kogu südame preparaadis, lihaskius ja isoleeritud rakus, on näidanud, et biokeemiline energia, mida tarbitakse südames ühe kokkutõmbe jooksul, on sõltuv teatud mehaanilisest indeksist. Samas ei mõjuta seda sõltuvust kokkutõmberežiim (isomeetriline, isotooniline või füsioloogiline). Kasutades seda katsetest saadud teadmist ja matemaatilise modelleerimise vahendeid, on võimalik hinnata keemiliste reaktsioonide kiirusi ja teisi olulisi parameetreid.

Katseliselt on näidatud, et raku kokkutõmbe protsess on kooperatiivne. Selle kooperatiivsuse kirjeldamine matemaatilise mudeliga on siiani olnud lahtiseks probleemiks. Antud doktoritöös on ära toodud deterministlik ristsillakeste mudel, milles on kooperatiivsust kirjeldatud termodünaamiliselt korrektsel viisil.

Et katsetest määrata ühe raku poolt sooritatud mehaanilist tööd ning selleks kulutatud biokeemilist energiat, on vajalik kasutada isoleeritud rakke. Isoleeritud südamelihasrakud on vabad sidekoest, mis võib oluliselt mõjutada mõõdetavaid mehaanilisi suurusi. Lisaks on üksikut rakku vaadeldes võimalik uurida raku sees toimuvaid protsesse. Isoleeritud rakul läbi viidud katsetes ei ole täidetud kogu südamele iseloomulikud füsioloogilised tingimused. Selleks, et üht rakku vaadelda füsioloogilistele tingimustele võimalikult lähedastel tingimustel, koostati selle doktoritöö vältel katsesüsteem, mis võimaldab kontrollida raku kontraktsiooni, kasutades süsinikfiibri tehnikat ja hinnata raku biokeemilisi omadusi fluorestsentssignaalist.

Selles doktoritöös on leitud lahendus proleemile, kuidas kaasata raku kontraheerumist kirjeldavasse matemaatilisse mudelisse kooperatiivsus, mis tuleneb kaltsiumi ja müosiinipea kooperatiivsest kinnitumisest aktiinile. Samuti on välja töötatud efektiivne ja töökindel meetod, mis hindab sarkomeri pikkust reaalajas, ja mis on aluseks, et viia läbi katseid raku mehaanilisite parameetreite hindamiseks.

LIST OF PUBLICATIONS

I **Kalda M**, Peterson P, Engelbrecht J, Vendelin M; **A Cross-Bridge Model Describing The Mechanoenergetics of Actomyosin Interaction.** *Computer Models in Biomechanics: From Nano to Macro*, Springer, 2013, 91–102.

II **Kalda M**, Peterson P, Vendelin M; **Cross-Bridge Group Ensembles Describing Cooperativity in Thermodynamically Consistent Way.** *PLoS ONE*, 2015, 10(9), e0137438.

III Peterson P, **Kalda M**, Vendelin M; **Real-Time Determination of Sarcomere Length of a Single Cardiomyocyte During Contraction.** *American Journal of Physiology - Cell Physiology*, 2013, 304(6), C519–531.

Summary of the author's contributions

I Writing the code for the cross-bridge mathematical model, preparation of all the figures presented in the article and participation in writing the manuscript.

II Participating in the designing of the model, writing the code for the cross-bridge mathematical model, preparation of all the figures presented in the article and participation in writing the manuscript.

III Participation in the designing of the study and performing all the experiments, revising the manuscript.

LIST OF CONFERENCE PRESENTATIONS

I **Kalda M**, Peterson P, Vendelin M; **Mechanoenergetics of actomyosin interaction analyzed by a cross-bridge model**; 36th International Congress of Physiological Sciences (IUPS2009), Kyoto, Japan, July 27–August 1, 2009

II **Kalda M**, Vendelin M; **Mechanoenergetics of actomyosin interaction analyzed by a cross-bridge model**; Biophysical Meeting, Boston, Massachusetts, February 28–March 4, 2009

III Vendelin M, **Kalda M**, Peterson P, Engelbrecht J; **Incorporating cooperativity into Huxley-type cross-bridge models in thermodynamically consistent way**; IUTAM Symposium on Computer Models in Biomechanics. Stanford, California, USA, August 28–September 2, 2011

IV **Kalda M**, Peterson P, Vendelin M; **Incorporating cooperativity into Huxley-type cross-bridge models in thermodynamically consistent way** Biophysical Meeting, San Diego, California, USA, February 25–29, 2012

V **Kalda M**, Vendelin M, Peterson P; **Real-time determination of sarcomere length of a single cardiomyocyte during contraction**; Biophysical Meeting 2013, Philadelphia, Pennsylvania, USA, February 2–6, 2013

VI **Kalda M**, Peterson P, Vendelin M; **Cross-bridge ensemble describing cooperativity in thermodynamically consistent way**; Biophysical Meeting 2015, Baltimore, Maryland USA, February 7–11, 2015

VII **Kalda M**, Peterson P, Vendelin M; **Cross-Bridge group ensembles describing cooperativity in thermodynamically consistent way**; 44th European Muscle Conference 2015, Warsaw, Poland, September 21–26, 2015

ACKNOWLEDGMENTS

I am grateful to my parents for always encouraging me to study. It is a privilege to have such a supporting and encouraging home.

I am thankful to Professor Jüri Engelbrecht and Professor Andrus Salupere for introducing me to the inspirational work place such as the Institute of Cybernetics. I am glad for the experience of working with Dr. Arvi Ravasoo and Dr. Andres Braunbrück in the acoustodiagnostics group, an exclusively left-handed team.

After working four years in a purely theoretical field, I was searching for an opportunity to work in an experimental laboratory. Thankfully, Dr. Marko Vendelin asked me to join the brand-new Laboratory of Systems Biology and gave me one of the most exiting projects that there was. The project was very challenging both experimentally and theoretically and without the help of my supervisor Dr. Marko Vendelin's enthusiasm, troubleshooting ability and positive thinking the project would not have been completed. I am also extremely grateful to my second supervisor Dr. Pearu Peterson for his ability to offer fresh viewpoints, his punctuality and perseverance in guiding me in my work.

I would also like to thank all the students who started this laboratory: Dr. Illaste, with whom I started my physics studies at the university and who encouraged me to join the laboratory; Dr. Sepp, with whom we discovered that trained python did not bite; Dr. Schryer, who helped me with English; and Martin, with whom we have tested all the equipment in the microscope room (at least twice). Also I am thankful to all the people who joined the laboratory later. My fellow students without whom I would not have been able to do my experiments: Niina, Jelena, Natalja, Sveta and our lab technicians Merle and Adele. Päivo, who helped me with mathematical problems and Dr. Ramay, who was the first to introduce me "Myotak". Also to Dr. Rikke Birkedal, who guided me in experimental issues. I am grateful to the whole friendly collective of the Institute of Cybernetics.

My gratitude belongs also to my siblings and friends for providing the much needed opportunity to renew my energy stores and to keep up the motivation. Without the ability to be *tädi* or to make *Kolamis Restart* and enjoy holidays in good company I would not have survived.

Lastly, special thanks to Silver for the love, support and motivation.

Thank you all for being so patient.

Financial support from the Wellcome Trust, the Estonian Science Foundation, and the European Union through the European Regional Development Fund (CENS Estonian Center of Excellence in Research) is acknowledged.

ACRONYMS

ADP	adenosine diphosphate
ATP	adenosine triphosphate
CCD	charge-coupled device
EMCCD	electron multiplying charge-coupled device
MD	molecular dynamics
NADH	nicotinamide adenine dinucleotide
NI DAQ	National Instruments Data Acquisition device
NIR	near infrared
Pi	phosphate ion
PZT	piezotranslators
SSA	stress–strain area

THESIS

1

INTRODUCTION

THE SUBJECT OF THIS DOCTORAL STUDY is a contracting cardiomyocyte: one very small, but very important component of the heart, which works incessantly and involuntarily as long as the organism lives. Because the fatigue of the heart would be fatal, myocytes are highly specialized in maintaining a high power output for a long period of time without developing energy deficiency. The energetic requirements are mainly met by mitochondrial respiration. The rate of respiration is accurately regulated so that energy production matches energy consumption. Investigating this regulation with mathematical modeling and experimental studies at a single cell level is fundamental for understanding the mechanoenergetics of the whole heart.

To pump blood, heart cells need to contract. Contraction of the cell is a result of the shortening of the basic unit of a cell called sarcomere. There are several theories that describe the process of sarcomere shortening [22]. One of the widely used theory was proposed by A. F. Huxley and R. Niedergerke and H. E. Huxley and J. Hanson about 60 years ago. Based on findings from observing the sarcomere during the shortening of the muscle tissue [9, 10], they proposed the sliding filament theory: the muscle tension is generated when the actin filament slides along the myosin filament using the energy from adenosine triphosphate (ATP) hydrolysis.

In this thesis, the contraction of the single cardiomyocyte is studied via

- mathematical modeling to describe the contraction of the cell theoretically;
- carbon fiber technique to describe the contraction experimentally.

1.1 MATHEMATICAL MODELING

Based on the sliding filament theory, a number of descriptions of cross-bridge interactions have been developed [24]. All these descriptions use slightly different assumptions, for instance a different number of biochemical states, different level of phenomenological modeling, different level of complexity to describe the cross-bridge cycle, etc.

In this work, the mathematical theory of stochastic processes is used to link the developed mechanical work of a cell to the biochemistry of different cross-bridge configurations in a thermodynamically consistent manner. In general, two approaches that are able to ensure thermodynamical consistency are molecular dynamics (MD) simulations and development of Huxley-type models. When the ultimate target is the development of a whole heart model, then Huxley-type models are preferred to describe contracting elements. The MD simulations are just too time consuming and would require too much of computer resources. In addition, Huxley-type models allow taking into account the free energy available from the hydrolysis of ATP, the amount of mechanical work performed by cross-bridges, and the free energy of different cross-bridge configurations (Publication I) when building up a thermodynamically consistent model.

One of the main assumptions in cross-bridge models is that all myosin heads are considered to act independently from one another. Based on the experimental results [33], it has become a general agreement that nearest-neighboring cooperativity exists between cross-bridges. How to include that cooperativity into the cross-bridge model has been a major problem in the field. To circumvent this problem, phenomenological models are often used. For example, cooperativity has been included in a phenomenological activation model [34] or assuming that developed force depends on sarcomere shortening velocity [15]. However, to my best knowledge, no thermodynamically consistent description of cooperativity for Huxley-type models has been developed yet.

The aim of this work is to introduce nearest-neighboring cooperativity in a cross-bridge model in a thermodynamically consistent way (Publication II). For that, ensembles of cross-bridge groups that are connected by elastic tropomyosin are defined. Within the groups, each cross-bridge is influenced by its neighbors and cooperativity is induced by tropomyosin movement. This assumption leads to a thermodynamically consistent description of cooperativity, as demonstrated in the thesis.

1.2 EXPERIMENTAL STUDY

To estimate mechanical and biochemical properties of the cardiac muscle, the whole heart or fiber preparations are often used [3, 27]. However, the use of the whole heart does not allow describing subcellular activities during contraction. Also the use of a trabecula is complicated because the experimental protocol is sensitive to tissue motion. Therefore, the use of single cells seems an ideal solution for studying subcellular mechanisms. However, most experiments on single intact cells are still performed under unloaded conditions, which are far from physiological conditions.

The aim of this work is to take advantage of the accessibility of isolated cells and at the same time apply the physiological mechanical load of tissue or heart preparation. Several research groups have elaborated experimental systems to control mechanical deformation and developed stress of a single isolated cardiomyocyte [11, 20, 23] using slightly different approaches. Within this project, an experimental setup similar to those used in [11, 20, 23] was constructed, with an additional ability to measure bioenergetics parameters in parallel with mechanical control. This is crucial for analyzing energy fluxes during cardiomyocyte contraction.

For studying the single cell contraction experimentally, it is important to accurately determine the sarcomere length of the cell. For that, an accurate and efficient computational method was developed for determining the mean sarcomere length from transmission images of a single contracting cardiomyocyte (Publication III).

1.3 LAYOUT OF THE THESIS

In this thesis, intracellular energy fluxes in contracting cardiomyocytes are studied. For that, a combination of mathematical modeling and experimental techniques is used. A mathematical description of actomyosin mechanoenergetics is composed with cross-bridge cooperativity incorporated into Huxley-type cross-bridge models in a thermodynamically consistent way. The description of the cross-bridge model is outlined in Chapter 2. The experimental part of the study involved constructing a system that allows simultaneous analysis of the mechanical contraction and bioenergetics of an isolated cardiomyocyte. This approach makes measurement of parameters describing the biochemical state of a cell at different workloads feasible. The experimental part is summarized in Chapter 3. The main conclusions are drawn in Chapter 4.

2

MODELING CELL CONTRACTION

During my doctoral study, two important aspects were introduced into the mathematical description of cross-bridge interaction

- the model of Vendelin et al. [34] was extended by incorporating the influence of the myosin head rotation into the free energy profile of myosin–actin interaction;
- cooperativity was incorporated into the Huxley-type model in a thermodynamically consistent way.

2.1 HUXLEY-TYPE CROSS-BRIDGE MODEL: THE BASIC IDEA

The basic contracting unit of a muscle, the sarcomere, consists of two types of protein filaments: a thick filament, formed mostly of protein myosin, and a thin filament, formed from three proteins called actin, troponin, and tropomyosin. According to the sliding filament theory, the thick and thin filaments slide along each other using the energy from ATP hydrolysis when the cardiomyocyte is contracting.

The model of Vendelin et al. [34] is a self-consistent Huxley-type model based on the T. L. Hill formalism [8] that links the free energy profile of the reactions with the mechanical force developed during the contraction. As MD simulations, Huxley-type models based on the T. L. Hill formalism allow of a description of the contraction process in a thermodynamically consistent way.

Cross-bridge, as defined by T. L. Hill [8], is a projection of the myosin head (attached or not) to binding sites on actin. The original Huxley-type model has two biochemical configurations for cross-bridges: detached and attached. The rate constants that describe the transition between those configurations are functions of relative distance, denoted by x, between the nearest cross-bridge equilibrium position and the actin binding site. As commonly done, we assume that a cross-bridge has exactly one head that is able to bind to one actin site. Every cross-bridge acts independently from other cross-bridges and can be in different biochemical configurations. The attached cross-bridge is assumed to produce elastic force F, which depends on the distance x, along myosin and actin filaments. According to T. L. Hill [8], this force F is related to the free energy G of the corresponding state: $F = \partial G/\partial x$. This relationship establishes the link between the mechanical force and chemical reactions. Namely, the ratio of the forward and reverse rate constants ($k_{A,B}$ and $k_{B,A}$) between states A and B is determined by the difference in the free energies of the corresponding biochemical states:

$$\frac{k_{A,B}(x)}{k_{B,A}(x)} = \exp\left(-\frac{G_B(x) - G_A(x)}{RT}\right), \tag{2.1}$$

where R is universal gas constant and T is absolute temperature.

According to T. L. Hill formalism, cross-bridges are divided into subensembles of cross-bridges with the same x. Due to the lack of register between myosin and actin, the number of cross-bridges in the subensembles is the same for any x.

Taking into account the assumption that the cross-bridges can interact only with the closest actin binding site, the state of the cross-bridges can be described by fractions $n_A(x,t)$ of cross-bridges that are in the same state A at time t in the subensemble at x. Assuming that the distance between the closest actin binding sites is d, the fractions $n_A(x,t)$ of all possible states are defined for x in the interval $(-\frac{d}{2}, \frac{d}{2})$. At any time t, all cross-bridges are in one of the states $\sum_A n_A(x,t) = 1$. Changes in cross-bridge states are induced by chemical transitions from one state to another or the sliding of actin and myosin filaments relative to each other with the rate $v(t)$ of sarcomere lengthening. For example, if A is a detached state and B is an attached state, then the governing equation for the state A is

$$\frac{\partial n_A}{\partial t} + \frac{\partial n_A}{\partial x} v(t) = k_{B,A} n_B - k_{A,B} n_A. \tag{2.2}$$

See the theory part of Publication II for a more detailed overview of the Huxley-type cross-bridge model.

2.2 OPTIMIZING FREE ENERGY PROFILES

The mathematical model of Vendelin et al. [34] comprises three biochemical configurations for cross-bridges: one weakly bound state W and two strongly bound force generating states S_1 and S_2. In [34], the locations of free energies minima of strongly bound states are assumed to be the same. However, the configuration of the cross-bridge is changed during the stroke (transition from S_1 to S_2) and that should lead to different free energy minima locations for states S_1 and S_2.

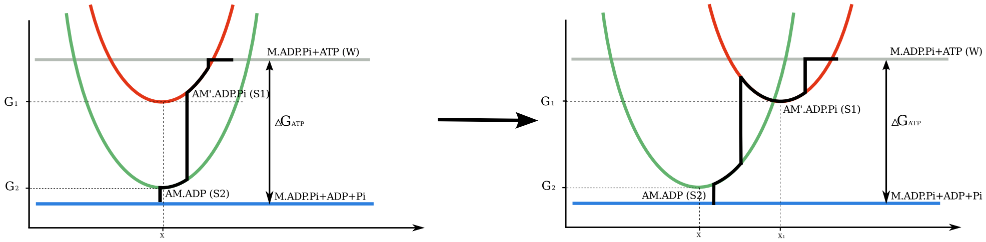

Figure 1 – Scheme of a possible set of free energy profiles and transition trajectory (black solid line) from the state where a cross-bridge is in the weakly bound state with ATP attached to myosin to the weakly bound state where ATP is hydrolyzed. G_1, G_2 and x_1 are parameters that describe the minimum points of free energy profiles for the states S_1 and S_2. Note that the left scheme describes the model of Vendelin et al. [34] and the right one the model in Publication I to illustrate the main difference between the models. In scheme A correspond to actin, M to myosin.

To adjust the model of Vendelin et al., a set of free energy profiles (shown in Figure 1) with different minimum positions for force producing states of the cross-bridge were found, so that the model would replicate the linear dependence between the oxygen consumption and the stress–strain area (SSA) in the cardiac muscle. A 3-state Huxley-type model with the phenomenological Ca^{2+}-induced activation model was used for modeling cross-bridge interaction.

The developed mathematical model was fit against experimental data [13] for isometric contraction at different half-sarcomere lengths as well as the linear dependence between the SSA and oxygen consumption. Simulation results are shown in Figure 2. Although the computed stress development of isometric contraction is underestimated compared with experimental data, twitch dynamics is mimicked well. The increase in the maximal stress with the increase in the sarcomere length is similar to experimental data. The stress development during the relaxation phase models experimental data without under- or overestimating it as other simulation results tend to do [16, 21, 25]. Prolongation of the twitch with the increase of the sarcomere length is reproduced as well.

Details of this model and the result are given in Publication I.

2.3 INCORPORATING COOPERATIVITY INTO A HUXLEY-TYPE MODEL

Huxley-type models assume that each cross-bridge acts independently from all others. Experimental evidence shows that the binding of Ca^{2+} to troponin and myosin head to actin are cooperative [33]. It has been suggested that cooperativity effects are due to the movement of tropomyosin around actin [26]. Such a

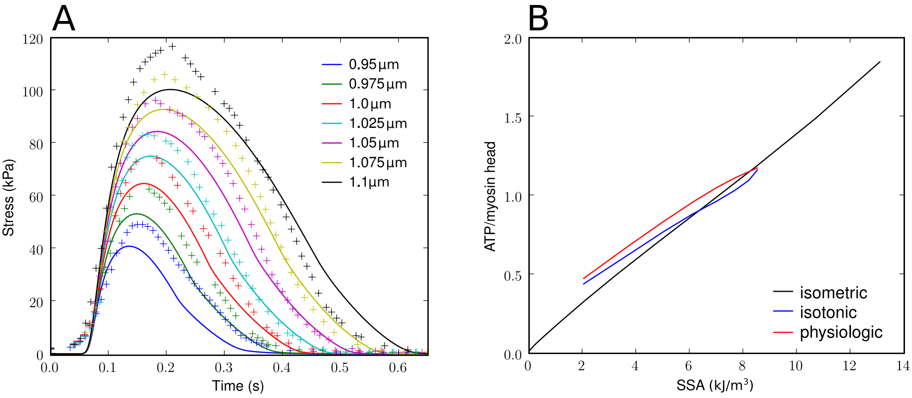

Figure 2 – Results of the simulation performed by the mathematical model. A: Stress in isometric contraction as a function of time at different half-sarcomere lengths (solid lines) compared with experimental measurements (crosses) [13]. B: Total amount of consumed ATP molecules per myosin head during a cardiac cycle as a function of SSA for isometric and shortening contractions.

displacement of tropomyosin is a result of Ca^{2+} [35] and myosin head [1] bindings.

Incorporating nearest-neighboring cooperativity into the description of cross-bridge interaction has been an open problem in the field for a long time. To my best knowledge, models that are used to describe this cooperativity have often been MD models or phenomenological models. For example, cooperativity has been included through the force–length relationship by making the developed force dependent on the sarcomere shortening velocity [15], or cooperativity from Ca^{2+} activation has been used [34].

A thermodynamically consistent description of cooperativity in deterministic cross-bridge models has been lacking so far. A thermodynamically consistent description means that the rate constants comply with the principle of microscopic reversibility. This principle declares that the lowest-energy pathway for the forward direction will be also the lowest-energy pathway in the reverse direction. In addition, there must be a link between the mechanical work and the energy available through chemical reactions, as in T. L. Hill [8], where force development depends on the free energy profile. This relationship ensures that even if the configuration of the state is not changed, the movement of the myosin head due to the shortening of the sarcomere is taken into account. Such a system does not produce more work than there is energy that the underlying chemical reaction, ATP hydrolysis, provides to do that work.

The original Huxley-type model does not include a Ca^{2+}-activation model.In Vendelin et al. [34] and Publication I, a phenomenological Ca^{2+}-activation model that included cooperativity effects of Ca^{2+} binding to tropomyosin was used. This phenomenological model describes the dynamics of Ca^{2+} binding to troponin C as a function of sarcomere length. To characterize the dynamics of Ca^{2+} during contraction, the activation function $A(t)$ was used, as in [30, 31]. The activation function describes stress development and depends on sarcomere length as well as Ca^{2+} concentration evolution during the beat. However, the kinetic mechanism of Ca^{2+} activation was not given in the phenomenological Ca^{2+}-activation model, so it can not be considered as a thermodynamically consistent model. Here an attempt is made to incorporate cooperativity into the Huxley-type cross-bridge model in a thermodynamically consistent way.

To include cooperativity into the description of actomyosin interaction

(i) the phenomenological model must be replaced with the chemical description of Ca^{2+} activation;

(ii) the assumption of cross-bridges independence must be revised so that the state change of one cross-bridge will influence at least the neighboring cross-bridges.

To avoid using phenomenological approach in the Ca^{2+}-activation model, two new states are introduced into the mathematical description. Figure 3 illustrates the difference between the descriptions in Publication I and Publication II. The

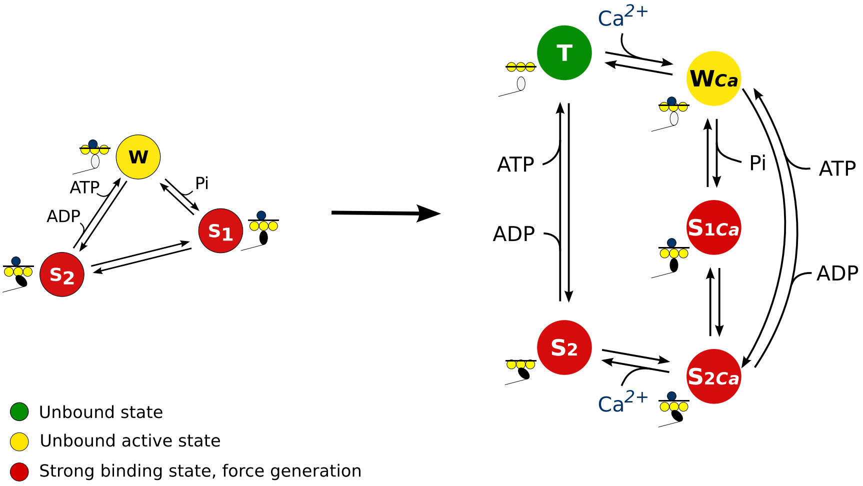

Figure 3 – Kinetic scheme of actin and myosin interaction used in the three-state Huxley-type model with phenomenological Ca^{2+}-induced activation and in five-state Huxley-type model.

description in Publication I consists of one weak binding state W and two strong binding states S_1 and S_2. The new description in Publication II introduces state T, where the myosin binding state on actin is "blocked" by tropomyosin. In addition, the second strong binding state S_2 is split into two states: state S_{2Ca}, where Ca^{2+} is bound to troponin and the cross-bridge is strongly bound, and state S_2, where the cross-bridge is strongly bound.

Huxley-type models based on the T. L. Hill formalism of ensembles assume that cross-bridges act independently from one another. The main hypothesis of the new description is that cooperativity between cross-bridges is induced by tropomyosin movement when Ca^{2+} binds to troponin or the myosin head binds to actin. In terms of the T. L. Hill formalism, an ensemble is formed from cooperative cross-bridge groups.

Publication II defines the ensemble as a group of five consecutive cross-bridges, as an example. The first and the last cross-bridge in the group are always in the unbound state (Figure 4).

Because tropomyosin connects all cross-bridges in a group, the elastic deformation of tropomyosin due to the binding of calcium to troponin or cross-bridge to actin binding state will influence the free energy of the group. Assuming that tropomyosin is an elastic string, its movement requires mechanical work. The treatment of cooperativity involves the formulation of the free energy function for a set of neighboring cross-bridges that includes the energy required to displace tropomyosin from its initial state to a new state. The transitions of cross-bridge groups can be induced either by chemical reactions or changes in the half-sarcomere length. As a result, the kinetics of cross-bridge cycling is described by

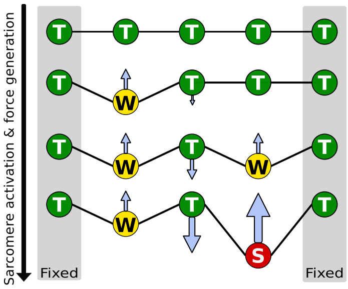

Figure 4 – Incorporating cooperativity into sarcomere activation and force generation. Arrows indicate the influences of the neighboring binding states due to elastic deformation on tropomyosin, which connects all cross-bridges in a group, on the binding of Ca^{2+} or force generation.

the following system of partial differential equations for ensemble state density functions $N_A(x_1, \ldots, x_q, t)$:

$$\frac{\partial N_A}{\partial t} + \frac{\partial N_A(x_1 + \xi, \ldots, x_q + \xi, t)}{\partial \xi}\bigg|_{\xi=0} \nu = \sum_B \left(k_{B,A} N_B - k_{A,B} N_A\right), \qquad (2.3)$$

where $k_{A,B} = k_{A,B}(x_1, \ldots, x_q, t)$ is the rate constant for the transition of the group from state A to B, $\nu = \nu(t)$ is the rate of the half-sarcomere lengthening, and $(x_1, \ldots, x_q)$ are distances of every cross-bridge from its equilibrium position.

A five-state model was optimized against measured values of active stress during a beat [13], requiring a match of the end-systolic points of isometric and physiological contraction. In addition, the linear relationship between ATP consumption and SSA for both contraction modes is requitred to match. To demonstrate that this model can be used to study cooperativity, the force production at different Ca^{2+} concentrations was also investigated. The developed formalism demonstrates that it is possible to use deterministic models such as the new five-state model to study the cooperativity of muscle contraction. Details of this model and the result are given in Publication II.

The main problem faced in describing the actin and myosin interaction is the realistic description of cooperativity. During this doctoral study, a thermodynamically consistent way to incorporate cooperativity into a Huxley-type cross-bridge model was developed. Note that this model was composed as an example to show that the developed theory was able to fit the data reasonably well. However, to increase the level of cooperativity, the model has to be developed further by for example enlarging the number of cross-bridges in the group or optimizing kinetic constants, etc.

3

MEASURING CELL CONTRACTION

One aim of my doctoral work was to build an experimental setup that would allow modification of the work loop of a single cardiomyocyte by using the carbon fiber technique and simultaneous measurement of energetics parameters. For that, an algorithm for estimating the mean sarcomere length of a cardiomyocyte in real time was developed.

3.1 SINGLE CELL EXPERIMENT

To estimate heart muscle mechanical and biochemical parameters under physiological conditions, whole heart experiments have been used [17, 28]. These experiments do not enable estimation of relevant parameters only on the subcellular level. To tackle the subcellular level heart muscle fibers are used. For example, experiments have been carried out on the cardiac trabecula [2] and the papillary muscle [32]. To measure the mechanical properties of the muscle fiber, one end of the sample is connected to a force transducer and the other end is connected to a motor or a micromanipulator. To estimate biochemical properties of the muscle fiber the fluorescence signal [4] or a micromechanocalorimeter [6] have been used. Note that the muscle fiber contains a connective tissue that modifies the mechanical properties of the sample, and therefore representative data for a single cell are harder to obtain since the corrections taking into account connective tissue properties have to be applied to the measured data. In addition, estimation of biochemical parameters of the muscle fiber from the fluorescence signal is affected by the motion artifact. However, motion artifacts can be reduced by using ratiometric correction [3].

For estimating subcellular properties, a single cell as a sample is preferred. Experiments at the muscle fiber level have shown that nicotinamide adenine dinucleotide (NADH) signal is influenced by the simulation frequency [3]. Similar experiments on an unloaded single cell did not show any influence of the frequency [5]. The difference between these experiments is that an unloaded single cell is not at physiological conditions. As the measured data show, for unloaded cells the

SSA is relatively small and the responsive oxygen consumption is low. Since the ATP consumption is not highly stimulated, the mitochondrial respiration is low and noticeable changes in the NADH signal are not expected. To be able to use a single cell also at physiological conditions, similar approaches have been used as for muscle fibers. For example the cell was connected to a force transducer and a motor to estimate the mechanical properties [7]. As a new approach, the carbon fiber technique was proposed [29, 36]. This technique uses two carbon fibers (depending of the purpose of the experiment, one thick (30–40 µm) and one thin (10 µm) or two thin fibers) attached to the cell. By connecting the carbon fiber to micromanipulators, the contraction of the cell can be controlled by applying a preload or an afterload to the cell. This technique has been used for estimating various properties of a single cell [12, 14, 18, 19]. The same technique was also used in this doctoral study.

3.2 SETUP OF THE SYSTEM

Several research groups have built systems to control the stretch and shortening of a single cardiomyocyte [11, 20]. Compared to the already existing systems, the main improvement in the system built during this study was making the system stable and fast enough to be able to replace the feed-forward control over the force and sarcomere length with feed-backward control.

In our system, shown in Figure 5, images are recorded via an Andor iXon electron multiplying charge-coupled device (EMCCD) (fluorescence) and an ImperX charge-coupled device (CCD) (transmission) mounted on a Nikon TiU microscope. By using two filter cubes mounted in the turrets on top of each other, we split fluorescence excitation, emission, and near infrared (NIR) transmission light allowing simultaneous recording of fluorescence and transmission images. The transmission image is processed in real time to estimate sarcomere length. An electrical field stimulator and carbon fibers are used to control cell contraction. The carbon fibers are connected to piezotranslators (PZT) mounted on top of micromanipulators. The PZT are controlled in real time by software using the carbon fiber position or sarcomere length as the input. The setup is controlled by software developed at the Laboratory of Systems Biology at the Institute of Cybernetics at Tallinn University of Technology.

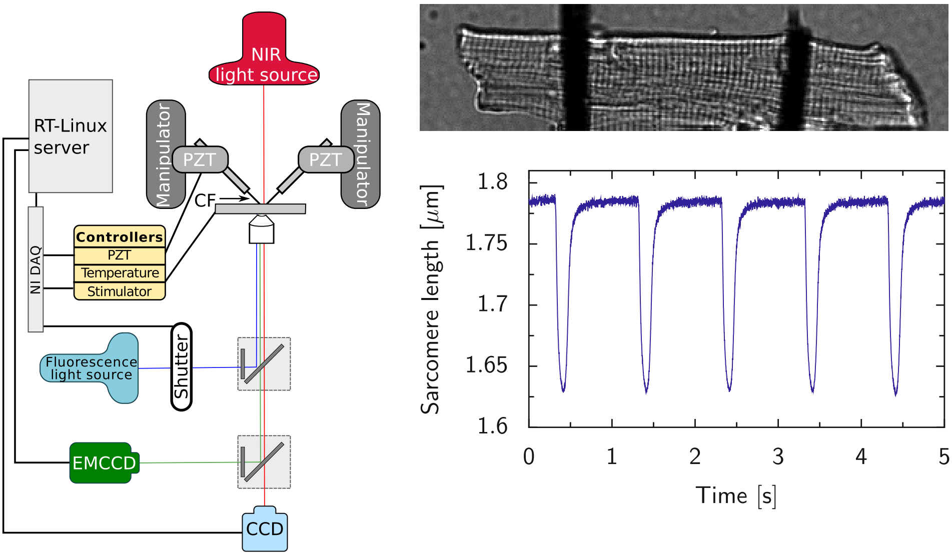

Figure 5 – A setup for studies of single cell mechanics and energetics (left) and a recorded transmission image (top right) of a cardiomyocyte with attached carbon fibers together with estimated sarcomere length dynamics during several beats (bottom right).

3.3 FLUORESCENCE MEASUREMENTS

This experimental system allows simultaneous monitoring and analysis of the transmission images to regulate the work loop of the cell and to collect data from fluorescence camera for analyzing the energetics changes in the cell.

A widefield fluorescence microscope was used instead of a confocal microscope to avoid motion artifacts. Although the confocal microscope eliminates out-of-focus light because of point illumination, the use of one plane of the contracting cell is not sufficient to describe the energy fluxes inside the cell, as during the contraction different parts of the cell are at the focal plane. When using a widefield fluorescence microscope, all of the single cell is excited at the same time and the fluorescence is collected from the whole cell. By summing up the collected signal for every image separately, we can estimate the changes of the energy fluxes in time.

The system was tested to show its ability to demonstrate the dynamics of fluorescence during a beat, as shown in Figure 6. The response of the cell to an abrupt change in stimulation frequency is shown in Figure 7.

For testing the system, the fluorescence signal was recorded in cells loaded with either di-8-ANEPPS or Mitotracker Green dyes, to demonstrate that the method allows distinguishing the signal that changes within a beat (sarcolemma potential sensitive di-8-ANEPPS) from the signal that is expected to be constant (Mito-

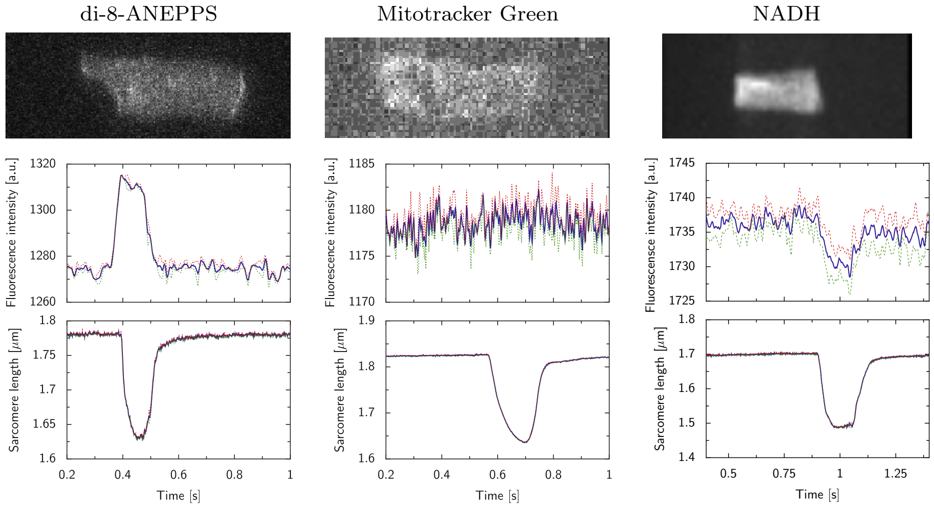

Figure 6 – Dynamics of the fluorescence signal during one contraction from a cell. Cells are simulated at 1 Hz and connected to carbon fibers. They are lifted from the cover glass and are contracting with the preload of carbon fibers. On the top, images form a cell loaded with di-8-ANEPPS, Mitotracker Green and autofluorescence of NADH are shown. In the middle, the corresponding average fluorescence signal is shown as a solid dark blue line, dashed lines denote standard deviation. At the bottom, changes in the sarcomere length during the beat are shown.

tracker Green). The fluorescence signal for NADH from the cells that are allowed to contract against a small load (only the carbon fibers are attached to the cell, no force control protocol is used), does not show any significant beat-to-beat changes. To use higher loads for cells, implementation of the isometric contraction protocol is required.

The response of the fluorescence signal for NADH to an abrupt change in the stimulation frequency indicates a change in the intensity of the signal similar to results in [3]. The change in the stimulation frequency (shown in Figure 7A) at the 60th second from 0 Hz to 4 Hz and at the 120th second back to 0 Hz leads to changes in the NADH signal with overshoots. When the simulation frequency changed from 1 Hz to 4 Hz repetitively (shown at Figure 7B) the overshoots were not so strong but still the changes in energy consumption were visible. Note that the NADH fluorescence signal decayed during experiments. This is either due to the quenching or photobleaching or indicates baseline stability problems with the fluorescence camera.

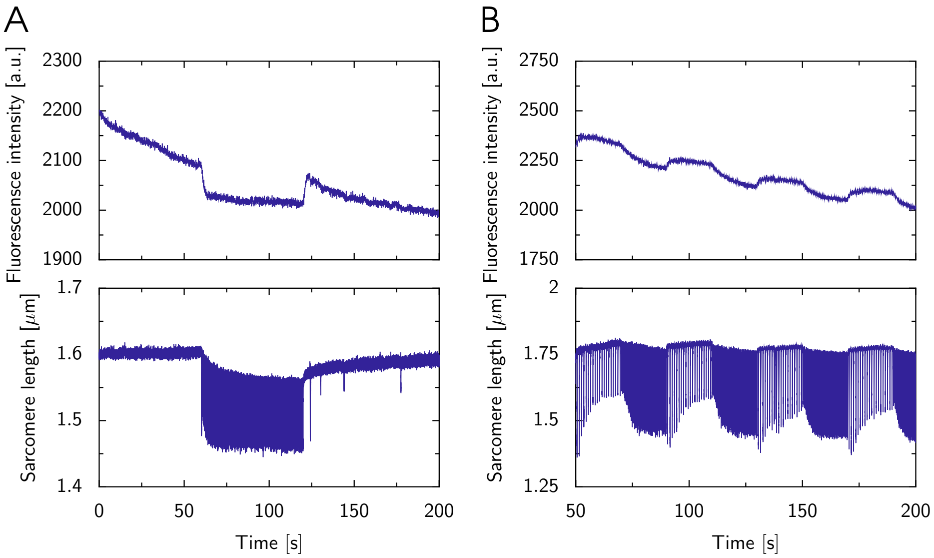

Figure 7 – Dynamics of the NADH fluorescence signal during an abrupt change in the stimulation frequency. A: The stimulation frequency changed from 0 Hz to 4 Hz and back to 0 Hz. B: The stimulation frequency changed between 1 Hz and 4 Hz.

3.4 SARCOMERE LENGTH MEASUREMENTS

For comparing the fluorescence signal changes at different workloads, it is very important to be able to measure the sarcomere length accurately. To modify the work loop, the sarcomere length has to be measured also in real time. To meet the needs of the experiment, an accurate and efficient computational method for determining the mean sarcomere length from transmission images of a single contracting cardiomyocyte was developed.

In a transmission image of the cardiomyocyte, the sarcomeres appear as repeating patterns of darker and lighter regions of Z-disks. The mean sarcomere length is defined as a spatial period of this pattern. The reason for developing a new method instead of applying the conventional autocorrelation function and spectral analysis based methods that use Fast Fourier Transform is the systematic errors of these methods caused by incorrectly handled boundary conditions.

To determine the mean sarcomere length from an image of a cardiac cell, the new method uses the least square difference between the image and its shifted copy. The minimal difference is obtained when the shift between the image and the copy is close to the mean sarcomere length. To take into account the spatial dependence of neighboring image pixels, the sarcomere striation pattern content from the microscopy images is extracted by using a detrend algorithm. All figures in this chapter use the described algorithm for calculating the sarcomere length. Details of this algorithm are given in Publication III. This algorithm is essential in using different pre- and afterload protocols to estimate the energy fluxes in isolated single cells at physiological conditions.

4

CONCLUSIONS

This thesis focused on mechanoenergetical properties of a single heart cell. The main results are given below.

CONCLUSIONS FROM MATHEMATICAL MODELING

I The model of Vendelin et al. [34] was adjusted by incorporating the influence of myosin head rotation into the free energy profile of actin and myosin interaction.

II A theory was developed to study the cooperativity of the muscle contraction in the thermodynamically consistent manner by using a Huxley-type model. This theory takes into account that each cross-bridge is influenced by its neighbors attached to the same actin filament and cooperativity is induced by tropomyosin movement. Muscle contraction is described by an ensemble of cross-bridge groups. Within a group, all cross-bridges are connected by tropomyosin. By the binding of calcium or myosin to actin, elastic deformation of tropomyosin is induced and the free energy of the cross-bridge group as well as reaction kinetics are influenced.

III A cross-bridge model was built as an example to illustrate the developed theory and its ability to reproduce experimental data.

CONCLUSIONS FROM EXPERIMENTAL STUDIES

I An experimental setup was established that allows modifications in the pre- and afterload applied to a single cardiomyocyte by using the carbon fiber technique as well as simultaneous measurement of energetics parameters.

II An accurate and efficient computational method for determining the mean sarcomere length from transmission images of a single contracting cardiomyocyte was developed. This method uses an unbiased measure of similarities, which eliminates systematic errors from conventional autocorrelation function based methods when applied to the region of interest of an image. A semianalytical seminumerical approach was used to evaluate the similarity measure in order to take into account spatial dependence of neighboring image pixels. A detrend algorithm was applied to extract the sarcomere striation pattern content from the microscopy images.

REFERENCES

REFERENCES

[1] E. Behrmann, M. Müller, P. Penczek, H. Mannherz, D. Manstein, and S. Raunser. Structure of the rigor actin-tropomyosin-myosin complex. *Cell*, 150(2):327–338, 2012.

[2] R. Brandes and D. Bers. Analysis of the mechanisms of mitochondrial nadh regulation in cardiac trabeculae. *Biophys. J.*, 77(3):1666–1682, 1999.

[3] R. Brandes and D. M. Bers. Increased work in cardiac trabeculae causes decreased mitochondrial nadh fluorescence followed by slow recovery. *Biophys. J.*, 71(2):1024–1035, 1996.

[4] R. Brandes, L. S. Maier, and D. M. Bers. Regulation of mitochondrial [NADH] by cytosolic [Ca^{2+}] and work in trabeculae from hypertrophic and normal rat hearts. *Circ. Res.*, 82(11):1189–1198, 1998.

[5] E. J. Griffiths, H. Lin, and M. S. Suleiman. NADH fluorescence in isolated guinea-pig and rat cardiomyocytes exposed to low or high stimulation rates and effect of metabolic inhibition with cyanide. *Biochem. Pharmacol.*, 56(2):173–179, 1998.

[6] J. Han, A. Taberner, R. Kirton, P. Nielsen, N. Smith, and D. Loiselle. A unique micromechanocalorimeter for simultaneous measurement of heat rate and force production of cardiac trabeculae carneae. *J. Appl. Physiol.*, 107(3):946–951, 2009.

[7] L. Hanft and K. Mcdonald. Sarcomere length dependence of power output is increased after pka treatment in rat cardiac myocytes. *AJP: Heart Circulatory Physiology*, 296(5):H1524–H1531, 2009.

[8] T. L. Hill. Theoretical formalism for the sliding filament model of contraction of striated muscle. Part I. *Prog. Biophys. Mol. Biol.*, 28:267–340, 1974.

[9] A. Huxley and R. Niedergerke. Interference microscopy of living muscle fibres. *Nature*, 173(1):13, 1954.

[10] H. Huxley and J. Hanson. Changes in the cross-striations of muscle during contraction and stretch and their structural interpretation. *Nature*, 173(4412):973–976, 1954.

[11] G. Iribe, M. Helmes, and P. Kohl. Force-length relations in isolated intact cardiomyocytes subjected to dynamic changes in mechanical load. *Am. J. Physiol. Heart Circ. Physiol.*, 292(3):H1487–H1497, 2007.

[12] G. Iribe and P. Kohl. Axial stretch enhances sarcoplasmic reticulum Ca^{2+} leak and cellular Ca^{2+} reuptake in guinea pig ventricular myocytes: experiments and models. *Prog. Biophys. Mol. Biol.*, 97(2-3):298–311, 2008.

[13] P. M. Janssen and W. C. Hunter. Force, not sarcomere length, correlates with prolongation of isosarcometric contraction. *Am. J. Physiol.*, 269(2 Pt 2):H676–H685, 1995.

[14] N. P. King, M. Methawasin, J. Nedrud, N. Harrell, C. Chung, M. Helmes, and H. Granzier. Mouse intact cardiac myocyte mechanics: cross-bridge and titin-based stress in unactivated cells. *J. Gen. Physiol.*, 137(1):81–91, 2011.

[15] A. Landesberg and S. Sideman. Coupling calcium binding to troponin C and cross-bridge cycling in skinne. *Am. J. Physiol.*, 266(3 Pt 2):H1260–H1271, 1994.

[16] A. Landesberg and S. Sideman. Mechanical regulation of cardiac muscle by coupling calcium kinetics with cross-bridge cycling: a dynamic model. *AJP: Heart Circulatory Physiology*, 267(2):H779–H795, 1994.

[17] P. Lee, P. Yan, P. Ewart, P. Kohl, L. Loew, and C. Bollensdorff. Simultaneous measurement and modulation of multiple physiological parameters in the isolated heart using optical techniques. *Pflugers Arch*, 464(4):403–414, 2012.

[18] S. Nishimura, Y. Kawai, T. Nakajima, Y. Hosoya, H. Fujita, M. Katoh, H. Yamashita, R. Nagai, and S. Sugiura. Membrane potential of rat ventricular myocytes responds to axial stretch in phase, amplitude and speed-dependent manners. *Cardiovasc. Res.*, 72(3):403–411, 2006.

[19] S. Nishimura, S. Nagai, M. Sata, M. Katoh, H. Yamashita, Y. Saeki, R. Nagai, and S. Sugiura. Expression of green fluorescent protein impairs the force-generating ability of isolated rat ventricular cardiomyocytes. *Mol. Cell. Biochem.*, 286(1-2):59–65, 2006.

[20] S. Nishimura, S. Yasuda, M. Katoh, K. Yamada, H. Yamashita, Y. Saeki, K. Sunagawa, R. Nagai, T. Hisada, and S. Sugiura. Single cell mechanics of rat cardiomyocytes under isometric, unloaded, and physiologically loaded conditions. *Am. J. Physiol. Heart Circ. Physiol.*, 287(1):H196 –H202, 2004.

[21] R. B. Panerai. A model of cardiac muscle mechanics and energetics. *J. Biomech.*, 13(11):929–940, 1980.

[22] G. H. Pollack. Muscle contraction mechanism: are alternative engines gathering steam? *Cardiovasc. Res.*, 29(6):737–746; discussion 747–757, 1995.

[23] B. Prosser, C. Ward, and W. J. Lederer. X-ros signaling: Rapid mechano-chemo transduction in heart. *Science (80-)*, 333(6048):1440–1445, 2011.

[24] J. Rice and P. de Tombe. Approaches to modeling crossbridges and calcium-dependent activation in cardiac muscle. *Prog. Biophys. Mol. Biol.*, 85(2-3):179–195, 2004.

[25] J. Rice, F. Wang, D. Bers, and P. de Tombe. Approximate model of cooperative activation and crossbridge cycling in cardiac muscle using ordinary differential equations. *Biophys. J.*, 95(5):2368–2390, 2008.

[26] J. C. Rüegg. Cardiac contractility: how calcium activates the myofilaments. *Naturwissenschaften*, 85(12):575–582, 1998.

[27] H. Suga. Ventricular energetics. *Physiol. Rev.*, 70(2):247–277, 1990.

[28] H. Suga, T. Hayashi, S. Suehiro, R. Hisano, M. Shirahata, and I. Ninomiya. Equal oxygen consumption rates of isovolumic and ejecting contractions with equal systolic pressure-volume areas in canine left ventricle. *Circ. Res.*, 49(5):1082–1091, 1981.

[29] S. Sugiura, S. Nishimura, S. Yasuda, Y. Hosoya, and K. Katoh. Carbon fiber technique for the investigation of single-cell mechanics in intact cardiac myocytes. *Nat. Protoc.*, 1(3):1453–1457, 2006.

[30] T. W. Taylor, Y. Goto, and H. Suga. Myocardial mechanics and the fenn effect determined from a cardiac muscle crossbridge model. *Med. Biol. Eng. Comput.*, 31(4):377–383, 1993.

[31] T. W. Taylor, Y. Goto, and H. Suga. Variable cross-bridge cycling-ATP coupling accounts for cardiac mechanoenergetics. *Am. J. Physiol.*, 264(3 Pt 2):H994–1004, 1993.

[32] G. H. Templeton, D. Tc, J. H. Mitchell, and L. L. Hefner. Dynamic stiffness of papillary muscle during contraction and relaxation. *Am. J. Physiol.*, 224(3):692–698, 1973.

[33] L. S. Tobacman. Thin filament-mediated regulation of cardiac contraction. *Annu. Rev. Physiol.*, 58:447–481, 1996.

[34] M. Vendelin, P. Bovendeerd, T. Arts, J. Engelbrecht, and D. van Campen. Cardiac mechanoenergetics replicated by cross-bridge model. *Ann. Biomed. Eng.*, 28(6):629–640, 2000.

[35] C. Xu, R. Craig, L. Tobacman, R. Horowitz, and W. Lehman. Tropomyosin positions in regulated thin filaments revealed by cryoelectron microscopy. *Biophys. J.*, 77(2):985–992, 1999.

[36] S. Yasuda, S. Sugiura, N. Kobayakawa, H. Fujita, H. Yamashita, K. Katoh, Y. Saeki, H. Kaneko, Y. Suda, R. Nagai, and H. Sugi. A novel method to study contraction characteristics of a single cardiac myocyte using carbon fibers. *Am. J. Physiol. Heart Circ. Physiol.*, 281(3):H1442 –H1446, 2001.

CURRICULUM VITAE

Curriculum Vitae

MARI KALDA

PERSONAL INFORMATION

DATE OF BIRTH	25. Aprill, 1983	
CONTACT	Männiku tee 98a-38, 11215	Tallinn, Estonia
	✉ mari@sysbio.ioc.ee	

EDUCATION

2007 — 2013	**Tallinn University of Technology (TUT)**	Tallinn, Estonia
SUBJECT	**PhD, Engineering Physics**	
THESIS	Mechanoenergetics of a single cardiomyocyte	
SUPERVISORS	**Dr. Marko Vendelin**, markov@sysbio.ioc.ee Head of Laboratory of Systems Biology, Institute of Cybernetics at TUT (IoC) **Dr. Pearu Peterson**, pearu@cens.ioc.ee Senior Researcher at IoC	

2005 — 2007	**Tallinn University of Technology**	Tallinn, Estonia
SUBJECT	**MSc, Engineering Physics**	
THESIS	Wave interaction in strongly inhomogeneous material.	
SUPERVISOR	**Dr. Arvi Ravasoo**	
	Senior Researcher at IoC	Tallinn, Estonia

2001 — 2005	**Tallinn University of Technology**	Tallinn, Estonia
SUBJECT	**BSc, Engineering Physics**	
THESIS	Interaction of waves in inhomogeneous materials	
SUPERVISOR	**Dr. Arvi Ravasoo**	
	Senior Researcher at IoC	Tallinn, Estonia

RESEARCH EXPERIENCE

2007 — Present	**Institute of Cybernetics at TUT** **Laboratory of Systems Biology**	Tallinn, Estonia
SUPERVISOR	**Dr. Marko Vendelin, Dr. Pearu Peterson**	

Measurement of energetic parameters in the contracting intact cardiomyocyte. Development of mathematical model of mechanoenergetics of actomyosin interaction. Programming data analysis tools.

2003 — 2007	**Institute of Cybernetics at TUT** **Center of Excellence for Nonlinear Studies**	Tallinn, Estonia
SUPERVISORS	**Dr. Arvi Ravasoo, Dr. Andres Braunbrück**	

Propagation and interaction of waves in strongly inhomogeneous elastic material.The equation of motion of the strongly inhomogeneous physically nonlinear elastic material is derived and possibility to solve this equation of motion was investigated by using Maple.

Curriculum Vitae

WORK EXPERIENCE

2007 — Present **Institute of Cybernetics at TUT** Tallinn, Estonia
Laboratory of Systems Biology
POSITION **Engineer/PhD student**

Constructing the experimental setup for system that will allow to analyze mechanical contraction and energetics of an isolated cardiomyocyte under microscope, preparing documentation for funding and annual report.

2007 **Ixonas** Tallinn, Estonia
POSITION **Software test engineer**

Planning, preparing, executing, documenting and maintaining functional, performance and regression tests. Developing test specifications.

2003 — 2007 **Institute of Cybernetics at TUT** Tallinn, Estonia
POSITION **Engineer/MSc student**
Mathematical modelling, numerical simulations.

SKILLS

- Operating Systems UNIX/Linux, Mac OS, Windows
- Day-to-day usage of Python (scipy, numpy), C++ programming languages
- Routine use of Emacs, Python(Matplotlib, PyX), LaTeX, Excel
- Maple

EXPERIMENTAL EXPERIENCE

- Experience with carbon fiber technique
- Experience with fluorescence and confocal microscopy

SCHOLARSHIPS AND AWARDS

- Archimedes/DoRa travel grants for presenting at international conferences 2009, 2012, 2013

PUBLICATIONS

- Kalda, Mari; Peterson, Pearu; Vendelin, Marko (2015). **Cross-Bridge Group Ensembles Describing Cooperativity in Thermodynamically Consistent Way.** *PLoS ONE*, **10(9)**, e0137438.

- Peterson, Pearu; Kalda, Mari; Vendelin, Marko (2013). **Real-time determination of sarcomere length of a single cardiomyocyte during contraction.** *American Journal of Physiology - Cell Physiology*, **304(6)**, C519-31.

- Kalda, Mari; Peterson, Pearu; Engelbrecht, Jüri; Vendelin, Marko (2013). **A cross-bridge model describing the mechanoenergetics of actomyosin interaction.** *Computer Models in Biomechanics : From Nano to Macro, Springer*, 91 - 102.

- Illaste, Ardo; Kalda, Mari; Schryer, David W.; Sepp, Mervi (2010). **Life of mice - development of cardiac energetics.** *The Journal of Physiology*, **588(23)**, 4617 - 4619.

CONFERENCE PRESENTATIONS

2015	**59th Biophysical Annual Meeting**	Baltimore, USA
POSTER	Kalda M, Vendelin M, Peterson P **Cross-Bridge Ensemble Describing Cooperativity in Thermodynamically Consistent Way**	
2013	**57th Biophysical Annual Meeting**	Philadelphia, USA
POSTER	Kalda M, Vendelin M, Peterson P **Real-time determination of sarcomere length of a single cardiomyocyte during contraction**	
2012	**56th Biophysical Annual Meeting**	San Diego, USA
POSTER	Kalda M, Peterson P, Vendelin M **Incorporating cooperativity into Huxley-type cross-bridge models in thermodynamically consistent way**	
2009	**36th International Congress of Physiological Sciences**	Kyoto, Jaapan
POSTER	Kalda M, Vendelin M **Mechanoenergetics of actomyosin interaction analyzed by a cross-bridge model**	
2009	**53rd Biophysical Annual Meeting**	Boston, USA

EXTRAS

Languages Estonian (mother tongue), English, Russian

Elulookirjeldus

MARI KALDA

ÜLDINFO

SÜNNIAEG	25. Aprill, 1983
KONTAKT	Männiku tee 98a-38, 11215 Tallinn, Eesti
	✉ mari@sysbio.ioc.ee

HARIDUS

2007 — 2013	**Tallinna Tehnikaülikool (TTÜ)**
ERIALA	**PhD, Tehniline füüsika**
LÕPUTÖÖ TEEMA	Ühe südameraku mehaanoenergeetika
JUHENDAJAD	**Dr. Marko Vendelin**, markov@sysbio.ioc.ee Süsteemibioloogia labori juht, TTÜ Küberneetika Instituut (KübI) **Dr. P. Peterson**, pearu@sysbio.ioc.ee KübI Vanemteadur
2005 — 2007	**Tallinna Tehnikaülikool (TTÜ)**
ERIALA	**MSc, Tehniline füüsika**
LÕPUTÖÖ TEEMA	Lainete interaktsioon tugevalt mittehomogeenses materjalis
JUHENDAJA	**Dr. Arvi Ravasoo** KübI Vanemteadur
2001 — 2005	**Tallinna Tehnikaülikool**
ERIALA	**BSc, Tehniline füüsika**
LÕPUTÖÖ TEEMA	Lainete interaktsioon mittehomogeenses elastses materjalis
JUHENDAJA	Dr. Arvi Ravasoo KübI Vanemteadur

TEADUSTÖÖ KOGEMUS

2007 — ...	**TTÜ Küberneetika Instituut** Tallinn, Eesti **Süsteemibioloogia laboratoorium**
JUHENDAJAD	**Dr. Marko Vendelin, Dr. Pearu Peterson**

Energeetiliste parameetrite mõõtmised mehaaniliselt koormatud kardiomüotsüütides. Aktomüosiini mehaanoenergeetilise interaktsiooni matemaatiline modelleerimine. Katseandmete analüüsiks tarkvara programmeerimine

2003 — 2007	**TTÜ Küberneetika Instituut** Tallinn, Eesti **Mittelineaarsete uuringute teaduse tippkeskus**
JUHENDAJAD	**Dr. Arvi Ravasoo, Dr. Andres Braunbrück**

Lainete levi ja interaktsiooni uurimine tugevalt mittehomogeenses elastses materjalis. Mittehomogeense füüsikaliselt mittelineaarse elastse materjali liikumisvõrrand tuletamine ning analüütiline ja numbriline lahendamine kasutades Maplit.

Elulookirjeldus

TÖÖKOGEMUS

2007 — … **TTÜ Küberneetika Instituut** Tallinn, Eesti
Süsteemibioloogia laboratoorium
AMETIKOHT **Insener/doktorant**

Ühe südame lihasraku eksperimentide tegemiseks vajaliku katsesüsteemi jaoks vajalike seadmete muretsemine ja käimalükkamine. Grantide finantseerimisaruandluse ja labori aastaaruannete koostamine.

2007 **Ixonos** Tallinn, Eesti
AMETIKOHT **Tarkvaratestija**

Funktsionaal, jõudlus- ja regressioontestimise planeerimine, ettevalmistamine, läbiviimine ja dokumeteerimine. Tarkvara testide spetsifikatsioonide väljatöötamine.

2005 — 2007 **TTÜ Küberneetika Instituut** Tallinn, Eesti
AMETIKOHT **Tehnik/magistrant**

Lainelevi matemaatiline modeleerimine, numbriliseld simulatsioonid.

OSKUSED

- Operatsioonisüsteemid UNIX/Linux, Mac OS, Windows
- Python (scipy, numpy paketid), C++ programeerimiskeeled
- Emacs, Python graafika (Matplotlib, PyX), LaTeX, Excel
- Maple

EKSPERIMENTAALTÖÖ

- Süsinikfiibri tehnika
- Fluorsestsents- ja konfokaalmikroskoopia baasoskused

STIPENDIUMID JA AUTASUD

- Archimedes/DoRa stipendiumid rahvusvahelistel konverentsidel osalemiseks 2009, 2012, 2013

PUBLIKATSIOONID

- Kalda, Mari; Peterson, Pearu; Vendelin, Marko (2015). **Cross-Bridge Group Ensembles Describing Cooperativity in Thermodynamically Consistent Way.** *PLoS ONE*, **10(9)**, e0137438.
- Peterson, Pearu; Kalda, Mari; Vendelin, Marko (2013). **Real-time determination of sarcomere length of a single cardiomyocyte during contraction.** *American Journal of Physiology - Cell Physiology*, **304(6)**, C519-31.
- Kalda, Mari; Peterson, Pearu; Engelbrecht, Jüri; Vendelin, Marko (2013). **A cross-bridge model describing the mechanoenergetics of actomyosin interaction.** *Computer Models in Biomechanics : From Nano to Macro, Springer*, 91 - 102.
- Illaste, Ardo; Kalda, Mari; Schryer, David W.; Sepp, Mervi (2010). **Life of mice - development of cardiac energetics.** *The Journal of Physiology*, **588(23)**, 4617 - 4619.

ETTEKANDED RAHVUSVAHELISTEL KONVERENTSIDEL

2015	**59th Biophysical Annual Meeting**	Baltimore, USA
POSTER	Kalda M, Vendelin M, Peterson P **Cross-Bridge Ensemble Describing Cooperativity in Thermodynamically Consistent Way**	
2013	**57th Biophysical Annual Meeting**	Philadelphia, USA
POSTER	Kalda M, Vendelin M, Peterson P **Real-time determination of sarcomere length of a single cardiomyocyte during contraction**	
2012	**56th Biophysical Annual Meeting**	San Diego, USA
POSTER	Kalda M, Peterson P, Vendelin M **Incorporating cooperativity into Huxley-type cross-bridge models in thermodynamically consistent way**	
2009	**36th International Congress of Physiological Sciences**	Kyoto, Jaapan
POSTER	Kalda M, Vendelin M **Mechanoenergetics of actomyosin interaction analyzed by a cross-bridge model**	
2009	**53rd Biophysical Annual Meeting**	Boston, USA
POSTER	Kalda M, Vendelin M **Mechanoenergetics of actomyosin interaction analyzed by cross-bridge model**	

LISAINFORMATSIOON

Keeled Eesti (emakeel), inglise, vene

APPENDIX

PUBLICATION I

Kalda M, Peterson P, Engelbrecht J, Vendelin M

A Cross-Bridge Model Describing the Mechanoenergetics of Actomyosin Interaction.

Computer Models in Biomechanics : From Nano to Macro, Springer , 2013, 91-102

The rules of the publisher prevent re-reprinting of Publication I. Official committe members and opponents will be given a copy of the publication to enable them to carry out a judicious review of this disseratation.

PUBLICATION II

Kalda M, Peterson P, Vendelin M

Cross-Bridge Group Ensembles Describing Cooperativity in Thermodynamically Consistent Way.

PLoS ONE, 2015, 10(9), e0137438.

Cross-Bridge Group Ensembles Describing Cooperativity in Thermodynamically Consistent Way

Mari Kalda[1], Pearu Peterson[1], Marko Vendelin[1*]

1 Laboratory of Systems Biology, Institute of Cybernetics at Tallinn University of Technology, Akadeemia tee 21, 12618 Tallinn, Estonia

* Corresponding Author markov@sysbio.ioc.ee

Abstract

The aim of this work is to incorporate cooperativity into Huxley-type cross-bridge model in thermodynamically consistent way. While the Huxley-type models assume that cross-bridges act independently from each other, we take into account that each cross-bridge is influenced by its neighbors and cooperativity is induced by tropomyosin movement. For that, we introduce ensembles of cross-bridge groups connected by elastic tropomyosin. By taking into account that the mechanical displacement of tropomyosin induces free energy change of the cross-bridge group ensemble, we develop the formalism for thermodynamically consistent description of the cooperativity in muscle contraction. An example model was composed to test the approach. The model parameters were found by optimization from the linear relation between oxygen consumption and stress-strain area as well as experimentally measured stress dynamics of rat trabecula. We have found a good agreement between the optimized model solution and experimental data. Simulations also showed that it is possible to study cooperativity with the approach developed in this work.

Introduction

In the heart, the mechanical work is tightly linked to energy conversion processes to ensure that the main function of the heart - pumping blood - is always possible. As a manifestation of a tight link between mechanics and energetics in the heart, it has been shown that oxygen consumption (VO_2) of the heart is linearly related to pressure-volume area (PVA) [1]. Pressure-volume area is a specific area in pressure-volume diagram surrounded by end-systolic PV line, the end-diastolic line and the systolic segment of the PV trajectory for heart contraction. As a analog of PVA-VO_2 relationship on tissue level, stress-strain area (SSA)-VO_2 linear relationship has been demonstrated [2] and can be used for estimation of regional VO_2 in the heart [3]. Earlier, we have shown that it is possible to reproduce PVA-VO_2 relationship by the finite element model of the left ventricle [4] if the active properties of myocardium are described by the model that reproduces SSA-VO_2 relationship [5].

As a part of regulatory mechanisms involved in the heart function, cooperative length-dependent activation of actomyosin interaction by calcium has been shown to play a major role in mechanical response of the heart [6]. While numerous mathematical models of heart contraction have been developed, accurate description of the cooperativity turned out to be problematic [7]. Among the developed approaches to model mechanical contraction, the models based on Huxley formalism or molecular dynamics simulations stand out by ability to link development of mechanical force to biochemistry in thermodynamically consistent manner [8, 9]. As a result, it is possible to simulate changes in mechanical force induced by changes in ATP, ADP, and Pi concentrations [10]. When compared with the molecular dynamics based approaches, deterministic nature of Huxley-type models makes them attractive for incorporation into mathematical models of the whole heart. However, while providing a strong theoretical base for linking mechanics and chemistry, Huxley-type models have been lacking description of cooperativity that would be thermodynamically consistent [5, 11]. For example, our earlier models while describing actin and myosin interaction in thermodynamically consistent manner, had a phenomenological description of Ca^{2+} activation to describe the sarcomere length dependency of the contraction [5, 12].

The aim of this work is to incorporate cooperativity of Ca^{2+} activation of actomyosin interaction into Huxley-type cross-bridge models in thermodynamically consistent way. Here, we give a description of theoretical framework of the developed approach that incorporates direct interactions between neighboring cross-bridges. Next, we demonstrate simulations performed by Huxley-type model using thermodynamically consistent description of the cooperative Ca^{2+} activation.

Theory

Huxley-type cross-bridge model

Before introduction of treatment of cooperativity, we give a description of the classical Huxley-type cross-bridge model. For simplicity, let as assume that actomyosin interaction can be described by three different discrete biochemical states, as in Fig. 1A. This simplification is used only in the theoretical description. The considered states are as follows. In state T (unbound state), the myosin binding site on actin is “blocked” by tropomyosin. In state W (unbound active state), Ca^{2+} is bound to troponin-C and the binding site is “open” for myosin head to bind to actin. Finally, in state S (strong binding state), myosin head is strongly bound to the actin. The state S is only state where myosin head is able to generate force. As in [8], a cross-bridge is defined as a myosin head projection to binding sites on actin characterized by the above mentioned states.

In Huxley-type single-site model [8, 9], the force produced by attached cross-bridge is assumed to be elastic and it depends on the axial position x of the nearest actin site, relative to model-defined

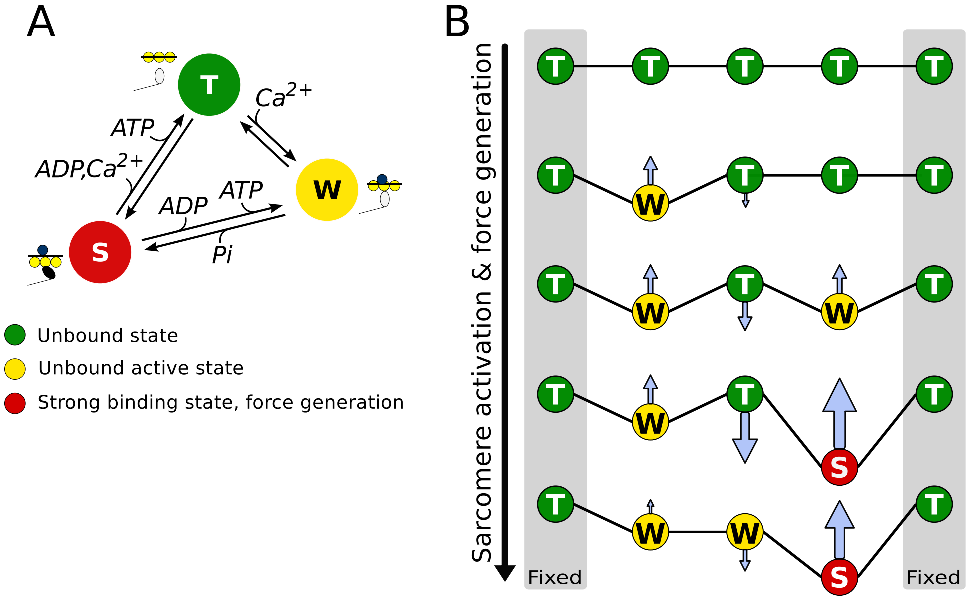

Figure 1: Computational model of the cross-bridge interaction. (A) Kinetic scheme of actin and myosin interaction used in three-state Huxley-type cross-bridge model. (B) Incorporating cooperativity into half-sarcomere activation and force generation. We consider an ensemble of five consecutive cross-bridges (binding states), out of which the first and the last ones are always in unbound state as boundary conditions. Arrows indicate the influences the neighboring binding states due to elastic deformation on tropomyosin, that connects all cross-bridges in a group, on binding of Ca^{2+} (transition from T to W) or force generation (transition from W to S).

origin. For example, the origin could correspond to the position at which cross-bridge does not produce force in one of the force-producing states. Since cross-bridge and the nearest actin site have one-to-one correspondence, for brevity, the position of the nearest actin site will be referred as cross-bridge position in the following text. If d is the length of one regulatory unit (RU — one troponin-tropomyosin complex and the seven associated actins [13]) of thin filaments, then x is defined in the range between $-d/2$ and $d/2$; $d \approx 36\mathrm{nm}$ [9]. According to T. Hill [8], the force F produced by the cross-bridge at position x is related to the free energy G of a particular state: $F = \partial G/\partial x$. Linear dependency of force on x leads to quadratic dependence for free energy, an assumption that we use throughout of this paper. Regarding this model, as there is no force associated with the states T and W ($F_{\mathrm{T}} = F_{\mathrm{W}} = 0$), the corresponding free energy functions are constant with respect to x.

Such relationship between mechanical force and free energy provides a unifying link between chemical reactions and mechanics. Namely, the ratio of the reaction rate constants is determined by the difference in free energies. For first order transitions between states, say, A and B, described by forward and reverse rate constants $k_{A,B}$ and $k_{B,A}$, respectively, the ratio is as follows:

$$\frac{k_{A,B}(x)}{k_{B,A}(x)} = \exp\left(-\frac{G_B(x) - G_A(x)}{RT}\right), \tag{1}$$

where R and T stand for universal gas constant and absolute temperature, respectively. For the considered model in Fig. 1A, A is either T, W, or S. For values of x, where $G_\mathrm{S} < G_\mathrm{W}$ (model in Fig. 1A), the strongly bound state is thermodynamically favorable; otherwise the unattached state is more favorable.

To describe the contraction of the muscle, we use kinetic formalism developed by T. Hill [8]. According to Hill's formalism, cross-bridges can be divided into ensembles (called subensembles in [8]) parameterized by the position x: cross-bridges are in the same ensemble if their positions are within the range x and $x + dx$. For the fixed dx, the number of cross-bridges in ensembles is assumed to be the same and constant for any x due to the lack of register between myosin and actin. In a given ensemble (labeled by x), we define $n_A(x,t)$ as a fraction of those cross-bridges that at time t are in a state A. We have:

$$n_\mathrm{T}(x,t) + n_\mathrm{W}(x,t) + n_\mathrm{S}(x,t) = 1. \tag{2}$$

Changes in cross-bridge states are induced either by chemical transition from one state to another or by sliding of actin and myosin filaments relative to each other with the rate $v = v(t)$ of half-sarcomere lengthening. For example, for state T, this would result in the following governing equation for $n_\mathrm{T}(x;t)$:

$$\frac{\partial n_\mathrm{T}}{\partial t} + \frac{\partial n_\mathrm{T}}{\partial x} v \quad = \quad k_\mathrm{S,T} n_\mathrm{S} + k_\mathrm{W,T} n_\mathrm{W} - \left(k_\mathrm{T,S} + k_\mathrm{T,W}\right) n_\mathrm{T}, \tag{3}$$

where $k_{A,B} = k_{A,B}(x)$ are the first order kinetic rate constants for transition from state A to state B. Similar equations are found for $n_\mathrm{W}(x,t)$ and $n_\mathrm{S}(x,t)$.

The integral properties of the muscle, such as developed stress and ATPase rate are found from integration over ensembles [8]. For instance, the Cauchy stress σ_a developed by cross-bridges in a half-sarcomere is an integral force of all cross-bridge states in all ensembles [14]:

$$\sigma_a(t) = \frac{ml}{d} \int_{-\frac{d}{2}}^{\frac{d}{2}} \left(n_\mathrm{T}(x,t)F_\mathrm{T}(x) + n_\mathrm{W}(x,t)F_\mathrm{W}(x) + n_\mathrm{S}(x,t)F_\mathrm{S}(x)\right)\, dx, \tag{4}$$

where the m is the number of cross-bridges in the unit volume and l is the length of the half-sarcomere. Taking into account the force relations of the current model, $F_\mathrm{T} = F_\mathrm{W} = 0$ and $F_\mathrm{S}(x) = K_\mathrm{S}(x - x_\mathrm{S}^\mathrm{eq})$, we have

$$\sigma_a(t) = \frac{mlK_\mathrm{S}}{d} \int_{-\frac{d}{2}}^{\frac{d}{2}} n_S(x,t)(x - x_\mathrm{S}^\mathrm{eq})\, dx, \tag{5}$$

where K_{S} and $x_{\mathrm{S}}^{\mathrm{eq}}$ are force constant and cross-bridge equilibrium position, respectively, corresponding to force generating state S.

The average cross-bridge ATP consumption rate is

$$V_{\mathrm{ATP}}(t) = \frac{1}{d} \int\limits_{-\frac{d}{2}}^{\frac{d}{2}} (k_{\mathrm{S,W}}(x) n_{\mathrm{S}}(x,t) + k_{\mathrm{S,T}}(x) n_{\mathrm{S}}(x,t) \\ - k_{\mathrm{W,S}}(x) n_{\mathrm{W}}(x,t) - k_{\mathrm{T,S}}(x) n_{\mathrm{T}}(x,t))\, dx \qquad (6)$$

leading to the total ATP consumption per cross-bridge during a beat

$$V_{\mathrm{ATP}}^{\mathrm{beat}} = \int\limits_{0}^{t_b} V_{\mathrm{ATP}}(t)\, dt, \qquad (7)$$

where t_b is the time period of one beat.

Note that while the thermodynamic considerations limit the ratio of rate constants (Eq. 1), the choice of one of the rate constant is not limited by the given equilibrium relationship. Thus, $k_{A,B}$ can depend on position x, half-sarcomere length l, time t, and some other parameters as long as $k_{A,B}/k_{B,A}$ ratio satisfies Eq. 1.

Cooperativity in Huxley-type model

General principles. For treatment of cooperativity in the model, we assume that the cooperativity is induced by tropomyosin movement. When Ca^{2+} binds to troponin-C, tropomyosin will shift to expose a binding site on actin [15]. Binding of myosin to the exposed binding site will shift the tropomyosin even further [16]. Since tropomyosin is a spiral protein wrapped around actin helix, movement of tropomyosin influences its movement in the neighboring RU binding sites as well. Assuming that tropomyosin is an elastic string, the movement of tropomyosin induced by binding of Ca^{2+} or myosin head requires mechanical work. The amount of required mechanical work depends on the states of the neighboring RU binding sites on actin as these states carry also the displacement information of tropomyosin at these binding sites. In essence, our treatment of cooperativity involves formulation of free energy functions for a set of neighboring cross-bridges that includes energy required to move tropomyosin from its initial state to a new state taking into account the displacements of tropomyosin at neighboring RUs.

For simplicity, we assume that the cross-bridges are connected by an elastic string representing tropomyosin (Fig. 1B). Attachment of $\mathrm{Ca}^{2+}$to troponin-C (transition from state T to W) or attachment of myosin head to binding site on actin (transition from state W to S) deforms the string altering its stress state. As a result of tropomyosin deformation, depending on the state of neighbor cross-bridges, attachment (or any other transition of states) can be either less or more thermodynamically favorable due to the elastic forces induced by deformation of tropomyosin before and after attachment.

For illustration, let us consider the transitions of a short sequence of cross-bridges connected with tropomyosin as shown in Fig. 1B. During attachment of Ca^{2+} by a troponin-C (transition from the top to the second row), tropomyosin is elongated between the first and the third cross-bridge (from the left). Such elongation requires additional mechanical work to be performed on the system leading to the increase of tropomyosin free energy after attachment. Same applies to the consecutive attachment of Ca^{2+} and transition to the strong binding state by one of cross-bridges (the third and forth rows from the top). However, attachment of Ca^{2+} to the central troponin-C is simplified due to the forces induced by tropomyosin deformation (transition to the last row). Thus, as it is shown in the example, changes in the cross-bridge states can be either hindered or facilitated due to the elastic deformation of tropomyosin induced by the neighbor cross-bridges.

To introduce cooperativity into Huxley-type model in thermodynamically consistent way, we assume that the muscle contraction can be described by ensembles of cross-bridge groups. In the classical Huxley-type models, cross-bridges are grouped into ensembles according to the position of the nearest actin binding site, as described in previous subsection. Cooperativity between cross-bridges is taken into account by generalizing the definition of ensembles by including the influence (state) of neighboring cross-bridges to a particular ensemble of cross-bridges. For that, let us assume that the states of q subsequent cross-bridges are related, that is, the transition of the state of one of these cross-bridges depends on the states of other cross-bridges. Ideally, q should be equal to the number of cross-bridges that are influenced by the same tropomyosin. This would ensure one-to-one correspondence between the mathematical model and the muscle mechanics. In practice, however, such a model would be difficult to realize because of its enormous size. Let us define a ensemble of cross-bridge groups consisting of q cross-bridges such that the positions of cross-bridges, $(x_1, x_2, \ldots, x_q)$, are in a range between $(x_1, \ldots, x_q)$ and $(x_1 + dx_1, \ldots, x_q + dx_q)$ for all members of the ensemble. We denote the states of cross-bridges in a group by $A = (\alpha_1, \ldots, \alpha_q)$, where α_i corresponds to the states of individual cross-bridges. We denote the set of individual cross-bridge states by $\mathbb{S}$. In our example $\mathbb{S} = \{\mathrm{T}, \mathrm{W}, \mathrm{S}\}$. To describe the state of cross-bridge group ensembles, we introduce the ensemble state density function $N_A(x_1, \ldots, x_q; t)$, such that

$$N_A(x_1, \ldots, x_q; t)\, dx_1 \cdots dx_q \tag{8}$$

gives the fraction of ensembles at time t in group state A and its cross-bridge positions in a range between $(x_1, \ldots, x_q)$ and $(x_1 + dx_1, \ldots, x_q + dx_q)$ among all possible ensemble configurations in terms of group states and cross-bridge position ranges:

$$\sum_A \int\limits_{-\frac{d}{2}}^{\frac{d}{2}} \cdots \int\limits_{-\frac{d}{2}}^{\frac{d}{2}} N_A(x_1, \ldots, x_q; t)\, dx_1 \cdots dx_q = 1, \tag{9}$$

where summation is taken over all possible states of cross-bridges in a group, that is $A \in \mathbb{S}^q$.

Because the cooperativity between cross-bridges is determined by the movement of the tropomyosin and q is going to be much smaller than the number of cross-bridges that are influenced by the same tropomyosin, we need to define also the states of cross-bridges that are immediate left and right neighbors of the specified q cross-bridges. In this work we assume that the corresponding boundary cross-bridges are in unbound inactive state and tropomyosin is in the initial relaxed state, i.e. the boundary cross-bridge is always in state T. In Fig. 1B, the example corresponds to ensembles formed by $q = 3$ cross-bridges with the additional boundary cross-bridges highlighted by gray areas. Although, the requirement of the boundary conditions ruins the one-to-one correspondence property of the model and the view of muscle, we presume that the cooperativity effects can be noticed within the possible artifacts introduced by these boundary conditions.

As for cross-bridges in the Huxley-type models, transitions between states of cross-bridge groups are driven by chemical reactions and the corresponding free energy profiles. It is assumed that all transformations in the cross-bridge group happen as separate reactions at different time moments for different cross-bridges within a group. Thus, as elementary processes of the considered system, chemical reactions involve only one cross-bridge or troponin-C. For example, only one Ca^{2+} attachment can take place at some time moment, not two calcium molecules binding simultaneously to the group.

The kinetics and force generation of the cross-bridge group is driven by the free energy change. Free energy G_A of the group in state A is defined as a sum of free energies of all cross-bridges (G_{α_i}) in the group and free energy of tropomyosin influencing them (U_A):

$$G_A(x_1, \ldots, x_q) = U_A + \sum_{i=1}^{q} G_{\alpha_i}(x_i). \tag{10}$$

In our formulation, we assume that tropomyosin is connected to actin at the locations of troponin complexes with the same spatial period d as RUs have. For example, when Ca^{2+} binds, the tropomyosin moves only at the corresponding connection point with the resulting elastic deformation of tropomyosin accommodating to the new configuration. In general, the location of myosin head is stochastic process, so is also subsequent tropomyosin deformation. For simplicity, we assume that the change of tropomyosin free energy in transition from W to S does not depend on the binding location of myosin head. With this assumption, we can compute the free energy of tropomyosin (U_A) as if the myosin head always binds at the location of tropomyosin connection points. As a result, free energy of tropomyosin depends only on cross-bridge group state A and not on position of each of the cross-bridges ($x_1, \ldots, x_q$). This is a manifestation of U_A not depending on ($x_1, \ldots, x_q$) in Eq. 10. The free energy of tropomyosin, with the group of cross-bridges in state A, is a sum of free energies of all tropomyosin fragments in the group:

$$U_A = U_{\mathrm{T};\alpha_1} + U_{\alpha_1;\alpha_2} + \ldots + U_{\alpha_q;\mathrm{T}}, \tag{11}$$

where $U_{\alpha;\beta}$ denotes the free energy of a tropomyosin string fragment between two neighboring cross-bridges being in respective states α and β. Thus, we have to define the free energies of all possible fragments to determine the system. An example of the free energy formulation is given in the Methods section as a part of the description of implemented model.

The shortening or lengthening of the half-sarcomere would lead to the same displacement of the cross-bridges in the group from the closest actin binding sites. This important property of the system has to be taken into account when considering permissive changes of cross-bridge groups within the q-dimensional space. As a result, and taking into account Eq. 10, the mechanical force produced by the group of cross-bridges is the sum of the forces produced by cross-bridges in the group:

$$F_A(x_1,\ldots,x_q) = \left.\frac{\partial G_A(x_1+\xi,\ldots,x_q+\xi)}{\partial \xi}\right|_{\xi=0} = \sum_{i=1}^{q} \frac{\partial G_{\alpha_i}(x_i)}{\partial x_i} = \sum_{i=1}^{q} F_{\alpha_i}(x_i), \tag{12}$$

where partial derivative of G_A is taken with the respect of the permissive changes in the q-dimensional space.

Taking into account that the cross-bridges groups can undergo transitions induced either by chemical reaction or changes in half-sarcomere length, the kinetics of cross-bridge cycling is described by the following system of partial differential equations for ensemble state density function $N_A(x_1,\ldots,x_q,t)$:

$$\frac{\partial N_A}{\partial t} + \left.\frac{\partial N_A(x_1+\xi,\ldots,x_q+\xi,t)}{\partial \xi}\right|_{\xi=0} v = \sum_B \left(k_{B,A}N_B - k_{A,B}N_A\right), \tag{13}$$

where $k_{A,B} = k_{A,B}(x_1,\ldots,x_q,t)$ is the rate constant for transition of the group from state A to B, and $v = v(t)$ is the rate of the half-sarcomere lengthening.

Taking into account that only one cross-bridge can perform a transition at any given time, as specified earlier in the definition of considered elementary processes, $k_{A,B}$ is non-zero only for such pair of group states A and B where only one cross-bridge is changed (for example, transition from state TTT to TWT): $B = (\alpha_1,\ldots,\beta_j,\ldots,\alpha_q)$ where $A = (\alpha_1,\ldots,\alpha_j,\ldots,\alpha_q)$ and j is the index of cross-bridge undergoing a state change. As before,

$$\frac{k_{A,B}(x_1,\ldots,x_q,t)}{k_{B,A}(x_1,\ldots,x_q,t)} = \exp\left(-\frac{G_B(x_1,\ldots,x_q) - G_A(x_1,\ldots,x_q)}{RT}\right). \tag{14}$$

Taking into account the considered elementary processes and partitioning of the free energy of the group (Eqs. 10 and 11), it is easy to show that the free energy difference between states A and B depends only on one cross-bridge position and not on positions of other cross-bridges in the group. In particular,

$$G_B - G_A = G_{\beta_j}(x_j) - G_{\alpha_j}(x_j) + U_{\alpha_{j-1},\beta_j} + U_{\beta_j,\alpha_{j+1}} - U_{\alpha_{j-1},\alpha_j} - U_{\alpha_j,\alpha_{j+1}} \tag{15}$$

where x_j is the position of the cross-bridge involved in the reaction.

From N_A, the mechanical stress produced by a half-sarcomere can be found similar to the classical Huxley-type models (Eq. 4). For Cauchy stress σ_a, the following integral has to be found:

$$\sigma_a(t) = ml \int_{-\frac{d}{2}}^{\frac{d}{2}} \cdots \int_{-\frac{d}{2}}^{\frac{d}{2}} \sum_A N_A(x_1, \ldots, x_q, t)\, F_A(x_1, \ldots, x_q)\, dx_1 \cdots dx_q. \tag{16}$$

To solve the system Eq. 13 for N_A, we introduce distribution function of cross-bridge groups γ and the fraction of cross-bridge groups n_A in state A among groups forming ensemble at $(x_1, \ldots, x_q)$:

$$\begin{aligned} \gamma(x_1, \ldots, x_q, t) &= \sum_A N_A(x_1, \ldots, x_q, t), && (17) \\ N_A(x_1, \ldots, x_q, t) &= \gamma(x_1, \ldots, x_q, t) n_A(x_1, \ldots, x_q, t), && (18) \\ \sum_A n_A(x_1, \ldots, x_q, t) &= 1. && (19) \end{aligned}$$

As shown in Appendix (Aim 1), the distribution function γ has the following general form:

$$\begin{aligned} \gamma(x_1, \ldots, x_q, t) &= \gamma_0(x_1 - a(t), \ldots, x_q - a(t)), && (20) \\ a(t) &= \int_{t_0}^{t} v(\tau) d\tau, && (21) \end{aligned}$$

where γ_0 is an initial distribution of the groups at $t = t_0$. Thus, cross-bridge group position in q-dimensional space is altered only through the changes in half-sarcomere length.

In addition, as shown in Appendix (Aim 2), n_A obeys

$$\frac{\partial n'_A}{\partial t} + \frac{\partial n'_A}{\partial x'_1} v = \sum_B (k'_{B,A} n'_B - k'_{A,B} n'_A), \tag{22}$$

after coordinate transformation

$$\begin{aligned} x'_1 &= \frac{1}{q} \sum_{i=1}^{q} x_i, && (23) \\ x'_i &= x_i - x_1, i = 2, \ldots, q, && (24) \end{aligned}$$

with n'_A and $k'_{A,B}$ representing n_A and $k_{A,B}$ in a new coordinate system $(x'_1, \ldots, x'_q)$. Notice that n'_A dynamics can be solved by integrating system of partial differential equations in t and x'_1 while $x'_2, \ldots, x'_q$ are parameters.

By selecting different γ_0, different assumptions regarding cross-bridge groups can be tested. For example, in a classical Huxley-type model, the lack of register between myosin and actin leads to constant γ_0.

Example. To illustrate how cooperativity would influence free energy profile of the group, let us consider the example in Fig. 2A. In this example, cross-bridge group with $q = 3$ performs a series of transformations from unbound state TTT to producing mechanical force in state SSS and returning to state TTT. During this process, three ATP molecules have been hydrolyzed to ADP and Pi. To distinguish the state where the cross-bridge has hydrolyzed ATP, an ’ symbol has been used next to the state (T’ and W’). Let us follow the hypothetical transition trajectory as shown in black in Fig. 2A. In the beginning of the process (states TTT, WTT, and WTW), Ca^{2+} binds to two troponin-C’s in the group, but do not produce any force. As a result, the free energy of the group is independent of cross-bridge position. On the transition to state WTS, one of the cross-bridges produce mechanical force leading to the parabolic relationship between the free energy and cross-bridge position. Further binding of Ca^{2+} to the second troponin-C in the group (state WWS), shifts the free energy downwards, but does not change the steepness of the relationship. However, formation of the second and the third strong-binding cross-bridge state (group in states WSS and SSS) leads to the change in the shape of free energy dependency on cross-bridge position due to the larger force produced by the group. The process is reversed by subsequent unbinding of the cross-bridges and Ca^{2+}. When we follow the changes in free energy of the group in time along this hypothetical trajectory, we can illustrate the role of tropomyosin deformation in free energy of the group (Fig. 2B). Note how addition of tropomyosin deformation component changes the free energy profile (solid line) if compared with the free energy profile of the reaction without tropomyosin deformation (dashed). Several reactions are made either more or less thermodynamically favorable, as it is evident from the changes in steps induced in the free

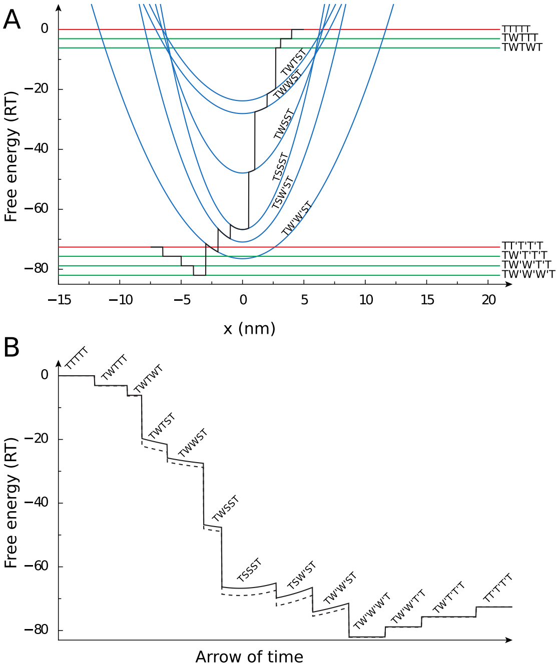

Figure 2: Scheme of free energy profiles and influence of cooperativity. (A) Scheme of one possible set of free energy profiles and transition trajectory (black solid line) from state where all five considered cross-bridges are in the unbound state (TTTTT) to state where three active cross-bridges are in unbound state with three ATP molecules hydrolyzed in reaction (TT’T’T’T). (B) Illustration of tropomyosin deformation influence on free energy of the cross-bridge group ensemble. The change of the free energy during reaction is shown for the simulation that takes into account the tropomyosin deformation (solid line) and for the simulation that does not take it into account (dashed line). Note that when tropomyosin deformation is considered, the change in free energy of the ensemble induced by one of the cross-bridges depend on the states of other cross-bridges in group.

energy during transitions from one state to another.

Simplifications used in the implemented model. There are several simplifications to the general theory presented above that were introduced while implementing the model. To limit the size of the model, as well as to test its influence we considered the cases where q was 1, 3, or 4.

The next set of simplifications reduces the dimensionality of the model. Namely, if each of the cross-bridges can be in any of K states ($K = 3$ for example in Fig. 1 with the state being either T, W, or S) then the system of partial differential equations describing cross-bridge kinetics (Eq. 13) consists of K^q equations. Those equations have to be solved in q-dimensional space to find evolution of $N_A(x_1, \ldots, x_q, t)$ in time. While the solution can be obtained by partitioning equations into a system of 1+1-dimensional partial differential equations with $q - 1$ parameters, as in Eq. 22, the solution of these equations requires extensive computational time. Additionally, as model parameters, multi-dimensional rate constants $k_{A,B}(x_1, \ldots, x_q, t)$ have to be specified. While $k_{A,B}$ are restricted by the free energy difference between states A and B (Eq. 15), this still requires specification of large number of multi-dimensional functions as a model parameters. In practice, such formulation leads to very large computational requirements.

To study the effects of cooperativity induced by tropomyosin displacements, we made several simplifications in the implemented model. First, it is assumed that the rate constants $k_{A,B}(x_1, \ldots, x_q, t)$ depend only on one x_i that corresponds to i-th cross-bridge in the group ongoing the change during the reaction. For example, the rate constant for transition from state TTT to TWT can be written as

$$k_{\mathrm{TTT,TWT}}(x_1, x_2, x_3, t) = k_{\mathrm{TTT,TWT}}(x_2, t). \tag{25}$$

Second, we assumed that all cross-bridges positions in the group are equal $x_i = x_0$. Note that this assumption reduces the dimensionality of the system (Eq. 13) and corresponds to the following choice of γ_0:

$$\gamma_0(x_1, \ldots, x_q) = \frac{1}{d}\,\delta(x_2 - x_1)\cdots\delta(x_q - x_1), \tag{26}$$

with δ denoting Dirac delta function. As shown in Appendix (Aim 2), the model equations are then

$$\frac{\partial n_A(x,t)}{\partial t} + \frac{\partial n_A(x,t)}{\partial x} v(t) = \sum_B \left(k_{B,A}(x,t) n_B(x,t) - k_{A,B}(x,t) n_A(x,t) \right), \tag{27}$$

$$\sigma_a(t) = \frac{ml}{d} \int_{-\frac{d}{2}}^{\frac{d}{2}} \sum_A n_A(x,t)\, F_A(x)\, dx. \tag{28}$$

Results

The following simulations were performed using a five-state model, that detailed description is given in Methods section. When compared with the three-state model (Fig. 1), the five-state model has three force-producing states instead of one. This allows to describe the movement of myosin head by shifting free-energy minima between two force-producing states and detachment of calcium from troponin-C while the cross-bridge is in force-producing state.

The aim of these simulations is to demonstrate that the model can be used in practice to reproduce different dynamic aspects of heart muscle contraction. Here, we fitted the model solutions to (i) reproduce stress developed during isometric contraction at different sarcomere lengths, (ii) relationship between ATP consumption and stress-strain area during isometric and physiologic contractions, and (iii) relationship between end-systolic sarcomere length and stress in isometric and physiologic contractions.

We compared the optimal solutions obtained by the model with and without cooperativity. The model with cooperativity had three cross-bridges in the group ($q = 3$), positioned between unattached cross-bridges, as shown in Fig. 1B. For the model without cooperativity, same model equations were used with $q = 1$ and tropomyosin free energy changes induced by cross-bridge cycling and calcium attachments were set to zero. As a result, that model neglected influence of cooperativity and was equivalent to the model without cooperativity, i.e. classical Huxley-type model formulation.

The optimized simulation results for the model with and without cooperativity are shown in Fig. 3.

During the optimization, the model parameters were varied to fit model solution against measured developed stress in isometric contraction (Fig. 3A), to obtain the same end-systolic relationship for isometric and physiologic contractions (Fig. 3B), and to obtain the same and linear relationship between ATP consumption and stress-strain area (Fig. 3C) for isometric and physiological contractions. The forward rate constants found by fitting for the case with cooperativity are shown in Fig. 4B. As described in Methods, tropomyosin free energy is given in the model through free energies of two tropomyosin segment configurations. The values of the free energies found by fitting of the model solution were $U_{\mathrm{T;W}} = 0.1\mathrm{RT}$ and $U_{\mathrm{W;S}} = 0.05\mathrm{RT}$.

The both models — with and without cooperativity — were able to fit the data reasonably well. The main difference between the models is in the better reproduction of maximal stress dependency on sarcomere length during isometric contractions by the model with cooperativity ($q = 3$) than by the model without cooperativity ($q = 1$) . We have also observed that the isometric relaxation phase is faster when cooperative interaction between cross-bridges is considered (Fig. 3A). However, it could be due to the differences in the model parameter values, such as rate constants, and cannot be solely attributed to the effects of cooperativity.

When simulating the end-systolic relationship between developed stress and half-sarcomere length, the both models had similar end-systolic relationships for isometric and physiologic contractions. As it is clear from Fig. 3B, in these simulations, the model without cooperativity ($q = 1$) obtained the end-systolic relationships that were marginally closer to each other in isometric and physiologic cases, when compared to the model with cooperativity ($q = 3$).

We calculated the amount of ATP molecules hydrolyzed during a contraction by each myosin head and related it to stress-strain area (SSA). For that, ATP consumption by a cross-bridge was found (Fig. 3C) and integrated over time. The simulations were performed at different afterloads (physiological contractions) and different sarcomere lengths (isometric contractions) to obtain ATP consumption corresponding to different SSA values. In accordance with the experimental data [2], the calculated relationship between ATP consumed in a beat and SSA is linear and the same for shortening and isometric contractions (Fig. 3D). The contraction efficiency, as determined by SSA and ATP consumption calculated by the model, was 74.4% and 61.0% for model with and without cooperativity, respectively. To estimate the efficiency, the model solution with the maximal SSA was used and we took into account the myosin ATPase concentration [17] of 0.18 mM (0.18 mol m^{-3})

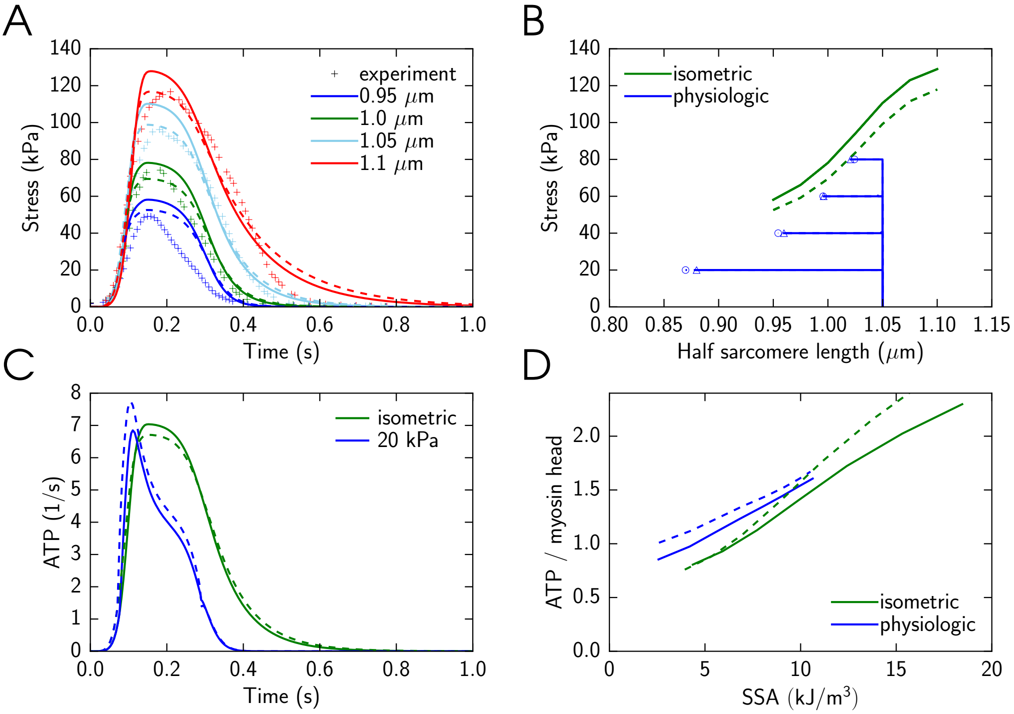

Figure 3: Use of the model with cooperativity between cross-bridges to simulate dynamic properties of the heart muscle contraction. Here, the solutions obtained with three interacting cross-bridges ($q = 3$, solid line) or a single cross-bridge ($q = 1$, dashed line) are shown. In these simulations, the model parameters were found by fitting model solution against the experimental data. A: Isometric contraction as a function of time at different half-sarcomere lengths from 0.95 μm to 1.1 μm compared with experimental measurements [20]. Sarcomere length is encoded in color, as indicated in the inset. B: End-systolic relationship between sarcomere length and stress for the isometric contractions are shown. In addition, changes in sarcomere length and developed stress are shown for physiologic contraction with the end-systolic value indicated by triangle ($q = 3$) or circle ($q = 1$) at different afterloads from 20 kPa to 80 kPa. C: ATP consumption by a cross-bridge during isometric and physiological contractions (20 kPa). Note how the difference in afterload changes ATP consumption by a cross-bridge. Here, simulations are shown for half-sarcomere end-diastolic length of 1.05 μm. D: Total amount of consumed ATP molecules per myosin head during a cardiac cycle as a function of SSA for isometric and physiologic contractions. Note that the both models reproduce the linear relationship between SSA and energy consumption.

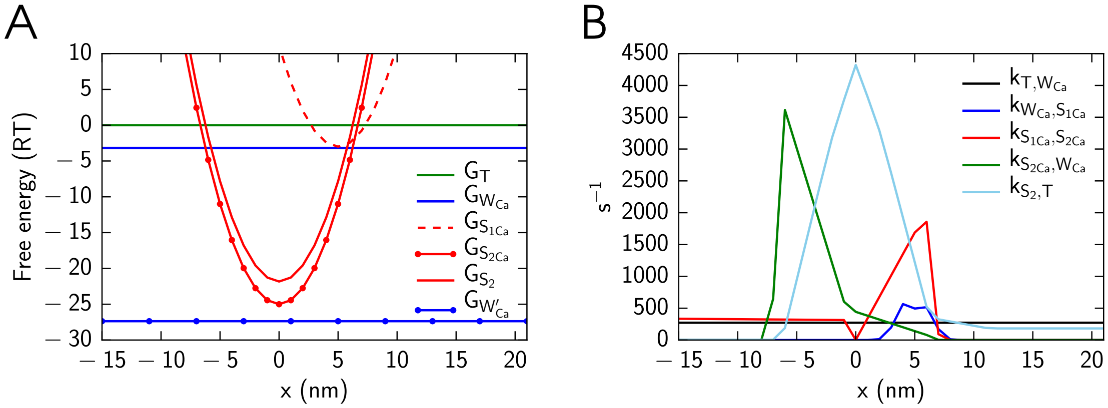

Figure 4: Free energy profiles (A) and cross-bridge forward rate constants (B). The model parameters were found by optimization procedure for the model with cooperativity induced by tropomyosin deformation ($q = 3$).

and free energy change during ATP hydrolysis of 60 kJ mol^{-1} [1,18]. The simulation results are in good agreement with experimental data. Namely, it was found that chemomechanical efficiency of cross-bridge cycling is in the range of 60-70% [1].

To find out whether the differences between model solutions in Fig. 3 are caused by the different model parameters found by the optimization or cooperativity effect, we performed the simulations with the same model parameters for the models with the different number of active cross-bridges in a group: $q = 1$, $q = 3$, and $q = 4$. For comparison, we used the set of parameters found by optimization for the model with cooperativity, $q = 3$ (Fig. 3). Note that in this case, the parameters were found with the non-zero tropomyosin free energies $U_{\mathrm{W;T}}$ and $U_{\mathrm{W;S}}$. Use of these free energies lead to modifications in the free energy profile, as illustrated in Fig. 2. For comparison purposes, we used the same tropomyosin free energies for the model with $q = 1$. Namely, in this case, a single cross-bridge that is able to change its state was located between two fixed cross-bridges. As a result, such case corresponds to non-cooperative model, but it takes into account some changes in free energy profile induced by the deformation of tropomyosin. Note that when we used the same model parameters but with zero tropomyosin free energies, the model solution was significantly disturbed that we attribute to the incompatibility between the rate constants and changes in free energy profile (results not shown).

As shown in Fig. 5, the results are different for different modes of cooperativity. The models with cooperativity ($q = 3$ and $q = 4$) give the solutions that are very similar to each other. In contrast, the model without cooperativity ($q = 1$), the peak isometric force is smaller (Fig. 5A) and sarcomere length has different dynamics during physiologic contractions (Fig. 5B). The contraction efficiency was also different for models with and without cooperativity (Fig. 5D). Thus, this example clearly demonstrates strong effects of interaction between cross-bridges in the same group on model solution indicating that this approach can be used to study cooperativity of muscle contraction.

To demonstrate that the model with multiple cross-bridges can be used to study cooperativity in Ca^{2+}

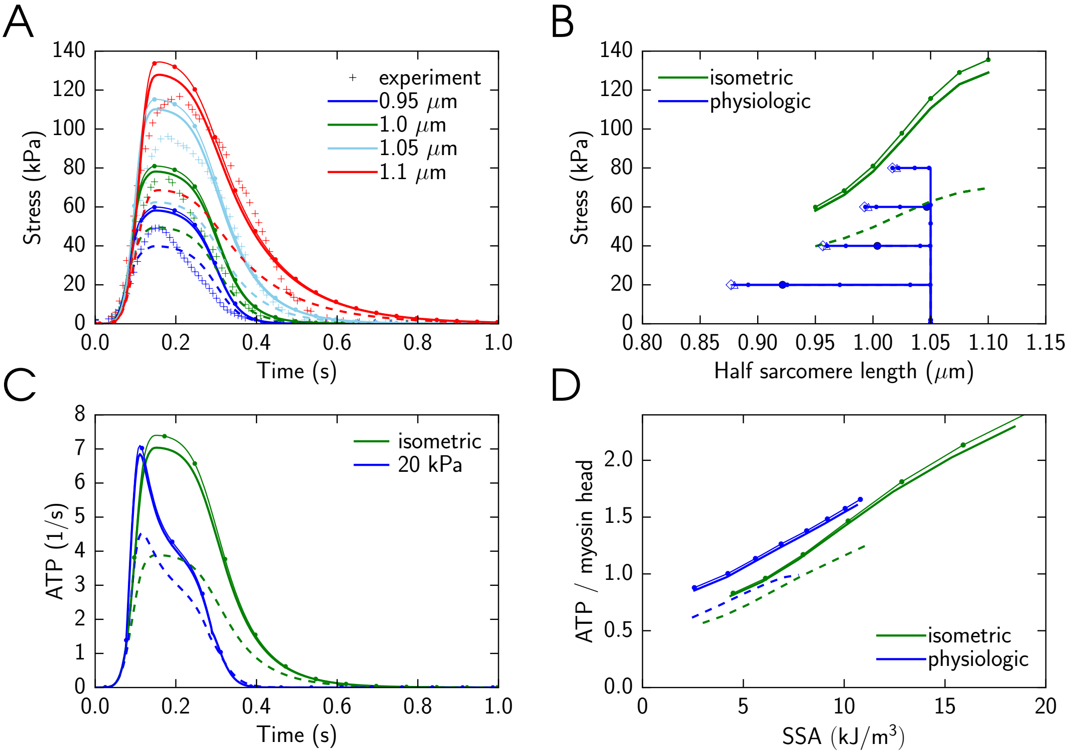

Figure 5: Influence of cross-bridge interaction on force generation and contraction. Here, the number of interacting cross-bridges was varied from one cross-bridge between the fixed ones ($q = 1$), to three and four ($q = 3$ or 4, respectively) active cross-bridges. The simulations were performed with the same model parameters, found by fitting for the model with $q = 3$. The subplots are as in Fig. 3, with the addition of one more solution ($q = 4$) marked by line with dots and the end-systolic value indicated by diamond. Due to lack of influence from the neighboring binding state to free energy profiles, developed stress at the case where $q = 1$ is significantly lower than other two cases. Simulation results for $q = 3$ and $q = 4$ are similar and sometimes overlapping in the figure.

binding, we calculated the force produced by the cross-bridges for different Ca^{2+} concentrations. In these simulations, Ca^{2+} concentration in the cell was taken constant and the steady-state solution was found (Fig. 6). According to our simulations, the cooperativity of calcium binding is rather low in all models with the optimized parameters (Fig. 6A). To check the cooperativity at different levels of calcium, we calculated the slope from the Hill's plot (taking derivative from $\log(F_{norm}/(1 - F_{norm}))$ — $\log[\mathrm{Ca}^{2+}]$ relationship, Fig. 6B). As clearly demonstrated in Fig. 6B, the Hill's coefficient was about 1 for models with optimized model parameters. Note that during our optimization we did not use experimental force-calcium relationships. To see whether the larger Hill coefficients can be observed, we analyzed solutions with the larger interactions between cross-bridges (larger $U_{\mathrm{W;T}}$ and $U_{\mathrm{W;S}}$ values). Some of these solutions are shown for the model with $q = 3$ (solid line) or $q = 4$ (solid line with bullets) in Fig. 6B. Note how the increase in changes in free energy of tropomyosin induced by its stretching leads to increase in Hill's coefficient.

Intriguingly, when the same model parameters were used for the model with $q = 1$ (only one cross-bridge between two fixed cross-bridges, dashed line), the Hill coefficient was always smaller or equal to one (Fig. 6B). In addition, we observed that the Hill coefficient was consistently higher at the lower range of Ca^{2+} concentration (smaller than the concentration required to develop half of the maximal force) than on the higher Ca^{2+} concentrations. This is consistent with the experimental results of Dobesh et al [19] where the similar asymmetry of cooperativity in Ca^{2+} binding was reported. Thus, the simulation results in (Fig. 6) demonstrate that cooperativity can be studied by this approach. However, as all our simulations with calcium binding in steady-state demonstrate, the model has to be developed further by either incorporating more interacting cross-bridges (increasing q) or variation of kinetic constants to reproduce high cooperativity of calcium binding observed in experiments.

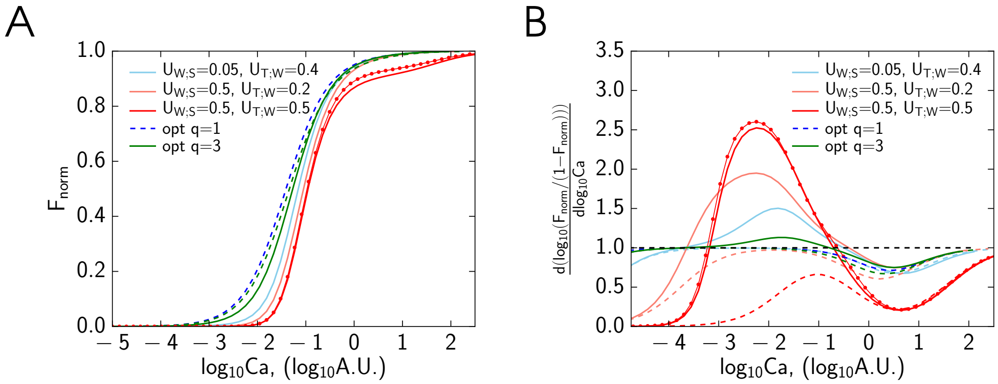

Figure 6: Calcium binding cooperativity measures calculated by the models with the different number of interacting cross-bridges. Here, the steady state solution of models is shown depending on calcium concentration with concentration given in arbitrary units at half-sarcomere length of 1.05 μm. The model solutions are designated by colors with green and blue depending on whether the parameters were found by fitting the data using $q = 3$ or $q = 1$ model, respectively; and by dashed, solid and line with dots, depending on whether the simulations were done using $q = 1$, $q = 3$ or $q = 4$ model, respectively. A: Normalized force-calcium relationship found by the model. All solutions demonstrate the low cooperativity indicating that this aspect of the model has to be refined. B: The Hill coefficient calculated from the slope of force-calcium relationship in log-log scale. For non-cooperative binding, the slope is expected to be 1 (black dashed line). In addition to the solutions found for optimized model parameters, we calculated the Hill coefficient for model solutions with the larger free energy changes induced by tropomyosin deformation (the free energies of the segments are given in the figure legend). Note how the increase in tropomyosin free energy changes induced by cross-bridges and calcium binding leads to the increase of the Hill coefficient in the models with cooperativity effects included ($q = 3$ and 4) in contrast to the model with only one cross-bridge that can change its state ($q = 1$).

Discussion

The main result of this work is the development of thermodynamically consistent approach to incorporate cooperativity between cross-bridges into Huxley-type models. By extending the notation of ensembles to consecutive cross-bridges influenced by the same tropomyosin and taking into account that mechanical deformation of tropomyosin requires mechanical work, we were able to derive equations describing the dynamics of cross-bridge interaction. The equations are based on T.L. Hill formalism and take into account microscopic reversibility. In terms of Razumova et al [13] nomenclature, the developed formalism describes RU-RU, XB-XB, and XB-RU classes of cooperativity, where XB and RU refer to cross-bridge and troponin-tropomyosin regulatory unit, respectively. To illustrate the use of derived formalism, an example model has been constructed and we demonstrate that it is possible to apply such model to study force generation and ATP consumption by heart muscle.

The experiments used in our model simulations were based on the same selection as our earlier simulations [5]. Namely, the model was tested against the data on isometric twitch and ATPase properties of the heart muscle. While multiple models are able to reproduce isometric force generation and many other aspects of mechanical contraction of the heart muscle [21] [11] [22], the link between ATP consumption by cross-bridges and force generation has been difficult to reproduce [23, 24]. According to large body of experimental evidence, at the same inotropic state, oxygen consumption of heart is linearly related to pressure-volume area [1]. On tissue level, the same relationship holds when oxygen consumption is related to stress-strain area [2]. In our earlier models, we were able to reproduce the relationships on tissue and left ventricular levels [4, 5]. However, in these models, the activation of cross-bridges was driven by phenomenological description of troponin-C which included cooperativity effects. While cross-bridge cycling was described in thermodynamically consistent manner taking into account microscopic reversibility, the dynamics of troponin-C activation was given as a function of sarcomere length without detailed kinetic mechanisms involved in calcium activation of the muscle. Such phenomenological description was sufficient for demonstrating that relationship between pressure-volume area and oxygen consumption of the muscle can be reproduced using Huxley-type models and highlighted the importance of twitch duration prolongation with the increase of sarcomere length to reproduce this property [5]. In this work, we seek for a thermodynamically consistent formalism of cooperativity effects that would allow to address the mechanistic aspects of cooperativity in future studies.

Many different approaches, with the varying levels of complexity, have been applied to study cooperativity in the heart muscle contraction [7]. Many models approach cooperativity using phenomenological descriptions [22]. While these models are advantageous to study contraction phenomena, there are always concerns on applicability of the models in the corner cases that were not considered during the model design and parameters estimation. To introduce mechanistic aspects of cooperativity, several spatial models have been constructed which describe muscle contraction using Monte Carlo or Ising approaches [7, 25, 26]. While in many models the description of cooperativity includes variation of forward or reverse rate of one or several reactions depending on the state of the neighboring cross-bridges breaking the microscopic reversibility, several models stand out by tracking the changes in kinetic constants induced by neighbor interactions and ensuring microscopic reversibility of reactions [25, 27]. However, these models have been used only on steady-state conditions to study cooperative calcium binding. In this work, we describe the model that ensures microscopic reversibility of the reactions similar to [25, 27] by taking into account that deformation of tropomyosin requires investment of chemical free energy. By extending the notation of ensembles to group of neighboring cross-bridges, we were able to overcome the difficulties of introducing cooperativity in thermodynamically consistent manner into Huxley-type models [11].

Our approach to introducing cooperativity into the Huxley-type model is similar to the approaches used by Zou and Phillips [28] as well as Campbell et al [29]. In these models, the free energy variations induced by the movement of tropomyosin were taken into account through their modification of the corresponding rate constants in cross-bridge kinetics. As in our study, the state of the neighbor cross-bridges was taken into account when finding the changes in deformation of the tropomyosin induced by the transition of the cross-bridge or troponin-C from one state to another [28, 29]. While there is a similarity in thermodynamically consistent description of cooperativity, there are also clear differences between our approach and the earlier models [28,29]. Namely, by using Huxley-type model and T.L.Hill approach linking the development of mechanical force with the free energy of the cross-bridge [8], the model ensures that mechanical work performed by the muscle is strictly consistent with the energy available to the cross-bridge through ATP hydrolysis. This is in contrast to the models that assume a fixed mechanical force developed by the cross-bridge in force-producing state that is not related to the deformation of the cross-bridge, as in [28, 29]. Through theoretical framework developed in our study, it is possible to model the mechanical contraction of the heart muscle, from cooperative binding of Ca^{2+} and cross-bridges to the force development, in thermodynamically consistent manner.

There are several simplifications that were introduced in formulation of the model. As one of the main simplifications in the model, we assumed that we can describe the position between equilibrium position of myosin heads and closest binding sites using one variable. Here, we assumed for simplicity, that the cross-bridge position is equal for all cross-bridges in the same group. In sarcomere, the same tropomyosin connects actin binding sites that would interact with different myofilaments. As a result, there is no trivial relationship between cross-bridges binding to consecutive actin binding sites and the system of partial differential equations (Eq. 13) has to be solved for q-dimensional fractions N_A. Notice that the system of PDEs can be parameterized using certain coordinate transformation (see Eqs. 22-24) leading to parameterized system of (1+1)-dimensional PDEs that can be numerically integrated in parallel, and hence, solving the full system Eq. 13 is feasible. However, for illustration of the Huxley-type model extension presented in this work, we avoided the parameterization by fixing the cross-bridge positions within one cross-bridge group relative to each other. As common in the field, we used the single binding site assumption. Namely, cross-bridge is assumed to be able to attach only to one site on actin, as in [8]. Multi-site attachment is possible by extending the kinetic schemes of actomyosin interaction as in [30]. However, as opposed to Huxley-type cross-bridge models, we include interaction between cross-bridges leading to the notation of ensembles that involve a group of cross-bridges. The developed formalism can be used for more complicated cases than shown in this work. For example, it is possible to apply the same approach to the case where movement of tropomyosin next to one cross-bridge induces modification along the tropomyosin influencing all cross-bridges in the group.

In our simulations, we fitted only limited dataset of experiments (Fig. 3). As clearly shown in

Fig. 6, the model with the found parameter values does not reproduce cooperativity of Ca^{2+} binding. While higher level of cooperativity has been demonstrated for model solutions with some other parameter sets, further optimization or model modification is needed to reproduce these data by the model.

As an application for the developed formalism and the mathematical models based on it, we envision the use of Huxley-type models for description of muscle active properties in simulations of the heart mechanics. As we have demonstrated earlier [4], it is possible to incorporate Huxley-type model into finite element model of the left ventricle. The numerical formulation of the finite element models of the heart requires finding elastic deformation of the heart wall and, if the active stress is described using the models that depend on rate of sarcomere shortening, finding the rate of deformation. Finding elastic deformation and the rate of deformation of the heart wall requires solution of a system of non-linear equations with deformation and the rate of the different parts of the wall influencing each other. As a part of iterative process usually used to find heart wall deformation, the developed active stress has to be calculated when given the deformation and its rate as an input. While use of Huxley-type models would make this part of calculations condiderably larger than a use of a small system of ordinary differential equations to describe active stress generation by sarcomeres, it is possible to run this part of calculations in parallel by calculating the active stress for each of the finite element nodes separately. With the increase of computational capacities available for researcher, usually in form of larger computer clusters, we think that the use of thermodynamically consistent Huxley-type models can help to study the cases where chemical environment in the cell, such as concentrations of ATP, ADP, inorganic phosphate and pH, is significantly different from control conditions.

In summary, we present extension of Huxley-type models that describes cooperativity of cross-bridge dynamics in thermodynamically consistent manner. The developed formalism demonstrates that it is possible to use deterministic models such as the model described in this work to study cooperativity of the muscle contraction.

Methods

Model description

Cross-bridge states. In our simulations we consider five-state cross-bridge mathematical model ($\mathbb{S} = \{\mathrm{T}, \mathrm{W}_{\mathrm{Ca}}, \mathrm{S}_{1\mathrm{Ca}}, \mathrm{S}_{2\mathrm{Ca}}, \mathrm{S}_2\}$) with the kinetic scheme for each of the cross-bridges shown in Fig. 7. In this mathematical model we have two biochemical states where no force is generated (T and W_{Ca}) and three force-generating states ($\mathrm{S}_{1\mathrm{Ca}}$, $\mathrm{S}_{2\mathrm{Ca}}$, and S_2). Out of these states, W_{Ca}, $\mathrm{S}_{1\mathrm{Ca}}$, and $\mathrm{S}_{2\mathrm{Ca}}$ have Ca^{2+} bound to associated troponin-C.

Tropomyosin displacement and associated free energy changes. As described in theory, cooperativity of cross-bridges is introduced by taking into account that the binding of calcium or cross-bridge leads to a displacement of tropomyosin. Since tropomyosin connects all cross-bridges in a group,

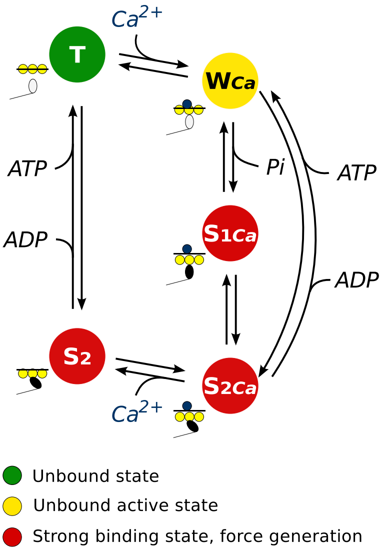

Figure 7: Scheme of five-state cross-bridge model. There are two biochemical states where no force is generated: unbound state T, unbound active state $\mathrm{W_{Ca}}$, where Ca^{2+} is bound to troponin-C. The strong binding state S is splited into three biochemical states where force is generated: $\mathrm{S_{1Ca}}$, $\mathrm{S_{2Ca}}$, where Ca^{2+} is bound to troponin-C and $\mathrm{S_2}$, where Ca^{2+} is unbound.

the elastic deformation of tropomyosin will influence the free energy of the group as well as reaction kinetics. Assuming linear relationship between elastic force and deformation, the elastic energy of tropomyosin fragment in between neighboring cross-bridge sites that are in state A and B, respectively, is

$$E_{A;B} = U_{tr} + \int_{d}^{l_{A;B}} (\xi - d)\,\mathcal{N}_A\, K_{tr} d\xi = U_{tr} + \frac{1}{2}\mathcal{N}_A\, K_{tr}\,(l_{A;B} - d)^2, \tag{29}$$

where $l_{A;B}$ is the length of tropomyosin fragment, d is minimal possible length of the fragment that is equal to the distance between neighboring actin binding sites (36 nm), K_{tr} is stiffness of single tropomyosin (21.6 pN/nm, [31]), $\mathcal{N}_A$ is Avogadro constant, and U_{tr} is elastic energy of relaxed tropomyosin:

$$U_{tr} = \frac{\mathcal{N}_A K_{tr} d^2}{2}. \tag{30}$$

At 37C, $U_{tr} \sim 3400$RT. In the considered five-state cross-bridge model, there are three different positions where tropomyosin can shift, we denote those positions as T, W, S. We have

$$\begin{aligned} E_{\mathrm{T;W}} &= U_{tr} + U_{\mathrm{T;W}}, \\ E_{\mathrm{T;S}} &= U_{tr} + U_{\mathrm{T;S}}, \\ E_{\mathrm{W;S}} &= U_{tr} + U_{\mathrm{W;S}}. \end{aligned} \tag{31}$$

We assume that the lengthening of tropomyosin is related to tropomyosin displacement by

$$d^2 + < displacement >^2 = < length >^2, \tag{32}$$

and that the displacement for transition T → S is equal to the sum of displacements for transitions T → W and W → S, see Fig. 8 :

$$\sqrt{l^2_{\mathrm{T;S}} - d^2} = \sqrt{l^2_{\mathrm{T;W}} - d^2} + \sqrt{l^2_{\mathrm{W;S}} - d^2}. \tag{33}$$

Combining Eqs. 31 and 33, shows that the free energy component $U_{\mathrm{T;S}}$ can be calculated from

$$U_{\mathrm{T;S}} = U_{tr} \left(\sqrt{1 + \left(\sqrt{\frac{U_{\mathrm{T;W}}}{U_{tr}} + 2\sqrt{\frac{U_{\mathrm{T;W}}}{U_{tr}}}} + \sqrt{\frac{U_{\mathrm{W;S}}}{U_{tr}} + 2\sqrt{\frac{U_{\mathrm{W;S}}}{U_{tr}}}} \right)^2} - 1 \right)^2 . \tag{34}$$

Since free energies $U_{\mathrm{T;W}}$ and $U_{\mathrm{W;S}}$ are significantly smaller than U_{tr}, the following approximation can be used to find $U_{\mathrm{T;S}}$:

$$U_{\mathrm{T;S}} = \left(\sqrt[4]{U_{\mathrm{T;W}}} + \sqrt[4]{U_{\mathrm{W;S}}} \right)^4 . \tag{35}$$

Cross-bridge kinetics. Cross-bridge formation in muscle fiber, that is the attachment and detachment of myosin head to actin binding site, is covered by Eq. 27. The force generation was modulated by calcium, leading to the mix of the first and second order reactions in the model. Thus, Eq. 27 was rewritten in general form as follows:

$$\begin{aligned} \frac{\partial n_A(x,t)}{\partial t} \quad + \quad & \frac{\partial n_A(x,t)}{\partial x} v(t) = \\ & \sum_B \left(k_{B,A}(x,t)\, n_B(x,t)\, C_{B,A}(t) - k_{A,B}(x,t) n_A(x,t)\, C_{A,B}(t) \right) , \end{aligned} \tag{36}$$

where $C_{A,B}(t)$ will be defined below. As described in general theory, only transitions involving a state change of only one cross-bridge in the group are allowed. Hence, the summation in

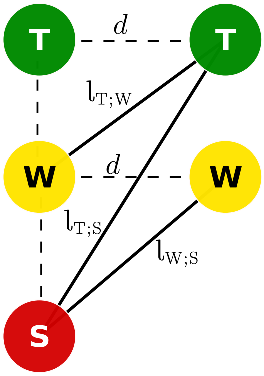

Figure 8: Scheme of possible conformations of tropomyosin between two cross-bridges. Here d is the length of one regulatory unit (36 nm), l_{TW}, l_{TS} and l_{WS} are the lengths of tropomyosin at different conformations.

Eq. 36 involves only group indexes in the following form: $B = (\alpha_1, \dots, \beta_j, \dots, \alpha_q)$ where $A = (\alpha_1, \dots, \alpha_j, \dots, \alpha_q)$.

Factor $C_{A,B}(t)$ depends only on α_j and β_j and can be written as

$$C_{\alpha_j,\beta_j}(t) = \begin{cases} Ca(t) & \text{if } (\alpha_j, \beta_j) \in \{(\mathrm{T}, \mathrm{W_{Ca}}), (\mathrm{S_2}, \mathrm{S_{2Ca}})\}, \\ 1 & \text{if } (\alpha_j, \beta_j) \in \{(\mathrm{W_{Ca}}, \mathrm{S_{1Ca}}), \\ & (\mathrm{S_{1Ca}}, \mathrm{S_{2Ca}}), (\mathrm{W_{Ca}}, \mathrm{S_{2Ca}}), (\mathrm{T}, \mathrm{S_2})\}, \\ 0 & \text{otherwise.} \end{cases} \tag{37}$$

Here, $Ca(t)$ describes Ca^{2+} transient as follows

$$Ca(t) = \begin{cases} \left(\frac{t}{T_p}\right)^4 & \text{if } t < T_p, \\ e^{-\left(\frac{t-T_p}{T_d}\right)^2} & \text{otherwise,} \end{cases} \tag{38}$$

where T_p is the time to peak of Ca^{2+}, T_d is characteristic duration time as in [5]. In simulations model with cooperativity and without cooperativity, we used the same parameters to describe Ca^{2+} transient (Fig. 9).

The rate constants were partitioned into components describing contribution of tropomyosin free energy change in reaction $h_{A,B}(x)$, dependence on cross-bridge position $f_{\alpha_j,\beta_j}(x)$ and sarcomere length $p_{\alpha_j,\beta_j}(l(t))$, as follows:

$$k_{A,B}(x,t) = e^{-\frac{G_{\beta_j} - G_{\alpha_j}}{2RT}} h_{A,B}(x)\, f_{\alpha_j,\beta_j}(x)\, p_{\alpha_j,\beta_j}(l(t)). \tag{39}$$

Note that the first term in the product corresponds to the contribution of the free energy change of the cross-bridge undergoing the state change in the reaction.

The free energy difference of tropomyosin during transition from A to B and its contribution to rate constants was taken into acount through $h_{A,B}(x)$. Tropomyosin influence was incorporated

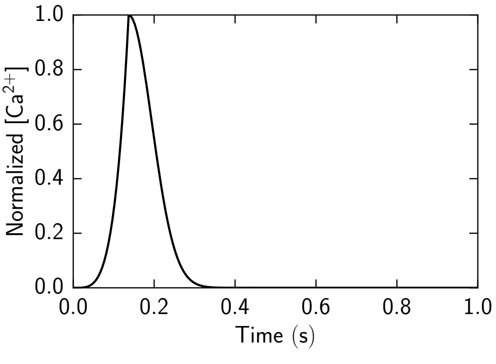

Figure 9: Normalized Ca^{2+} concentration transient used in simulations.

into the rate constants by increasing the free energy of the product state of the forward reaction:

$$h_{A,B}(x) = e^{-\frac{U_{\alpha_{j-1},\beta_j}+U_{\beta_j,\alpha_{j+1}}-U_{\alpha_{j-1},\alpha_j}-U_{\alpha_j,\alpha_{j+1}}}{RT}} \tag{40}$$

if $(\alpha_j, \beta_j) \in \{(\mathrm{W_{Ca}}, \mathrm{T}), (\mathrm{S_{1Ca}}, \mathrm{W_{Ca}}), (\mathrm{S_{2Ca}}, \mathrm{S_{1Ca}}), (\mathrm{W_{Ca}}, \mathrm{S_{2Ca}}), (\mathrm{S_{2Ca}}, \mathrm{S_2}), (\mathrm{T}, \mathrm{S_2})\}$, otherwise $h_{A,B}(x) = 1$.

The dependence of the rate constant on cross-bridge position and sarcomere length are symmetric:

$$f_{\alpha_j,\beta_j}(x) = f_{\beta_j,\alpha_j}(x), \tag{41}$$

$$p_{\alpha_j,\beta_j}(l(t)) = p_{\beta_j,\alpha_j}(l(t)). \tag{42}$$

The dependence of the rate constant on cross-bridge position $f_{\alpha_j,\beta_j}(x)$ was either constant (for reactions involving calcium binding) or continuous piecewise linear with given nodal points. The values of the nodal points were found by fitting. The location of the nodal points were as follows. For transitions between $\mathrm{W_{Ca}}$ and $\mathrm{S_{1Ca}}$, the nodal points were the boundary points $d/2$ and $-d/2$, $\mathrm{S_{1Ca}}$ free energy minimum, and the locations at which free energies of T and $\mathrm{S_{1Ca}}$ intersect. For transitions between $\mathrm{S_{1Ca}}$ and $\mathrm{S_{2Ca}}$, the nodal points were the boundary points $d/2$ and $-d/2$, $\mathrm{S_{2Ca}}$ free energy minimum ($x = 0$), the location at which $\mathrm{S_{1Ca}}$ and T free energies intersect after $\mathrm{S_{1Ca}}$ free energy minimum. For transitions between $\mathrm{S_{2Ca}}$ and $\mathrm{W_{Ca}}$, the same nodal points were used as for transitions between $\mathrm{S_{1Ca}}$ and $\mathrm{S_{2Ca}}$. For transitions between $\mathrm{S_{2Ca}}$ and T, the nodal points were the boundary points $d/2$ and $-d/2$, $\mathrm{S_{2Ca}}$ free energy minimum, the locations at which free energies of $\mathrm{W_{Ca}}$ and $\mathrm{S_{2Ca}}$ intersect, and the location found as a sum of $\mathrm{S_{1Ca}}$ free energy minimum location and the positive location at which $\mathrm{S_{2Ca}}$ and $\mathrm{W_{Ca}}$ free energies intersect.

Sarcomere length dependence $p_{\alpha_j,\beta_j}(l(t))$ was introduced only for calcium binding reactions (transitions between T and $\mathrm{W_{Ca}}$, and between $\mathrm{S_2}$ and $\mathrm{S_{2Ca}}$) and myosin binding reaction to actin (transition between $\mathrm{W_{Ca}}$ and $\mathrm{S_{1Ca}}$). For all other transitions, $p_{\alpha_j,\beta_j}(l(t))$ was taken equal to one. For transitions between T and $\mathrm{W_{Ca}}$ as well as between $\mathrm{S_2}$ and $\mathrm{S_{2Ca}}$, $p_{\alpha_j,\beta_j}(l(t))$ was in the form

$$p_{\alpha_j,\beta_j}(l) = 1 + p^{L1}_{\alpha_j,\beta_j} \frac{l_{max} - l}{l - l_{min}}, \tag{43}$$

where $p^{L1}_{\alpha_j,\beta_j}$ was optimized model parameter, l_{max} and l_{min} were 1.1 μm and 0.8 μm, respectively. For transition between $\mathrm{W_{Ca}}$ and $\mathrm{S_{1Ca}}$, we defined

$$p_{\mathrm{W_{Ca}},\mathrm{S_{1Ca}}}(l) = \exp\left(p^{L2}_{\mathrm{W_{Ca}},\mathrm{S_{1Ca}}} \left(\frac{l - l_{min}}{l_{max} - l_{min}}\right)^4\right) + 1, \tag{44}$$

where $p^{L2}_{\mathrm{W_{Ca}},\mathrm{S_{1Ca}}}$ was optimized model parameter.

Total force and ATP consumption. According to our assumption that only strong binding states produce force, the Cauchy stress σ_a developed by the cross-bridges in half-sarcomere is calculated according to the following equation:

$$\sigma_a = \frac{ml}{2d} \sum_A \int_{-\frac{d}{2}}^{\frac{d}{2}} n_A F_A dx. \tag{45}$$

The ATP consumption is given by the cross-bridge cycling rate:

$$V_{ATP} = \frac{1}{d} \sum_{A} \int_{-\frac{d}{2}}^{\frac{d}{2}} \delta_{ATP}(A, B) \left(k_{B,A} n_B - k_{A,B} n_A \right) dx, \tag{46}$$

where

$$\delta_{ATP}(B, A) = \delta_{ATP}(A, B) = \begin{cases} 1 & \text{if index } j \text{ exists such that} \\ & (\alpha_j, \beta_j) \in \{(\mathrm{T}, \mathrm{S_2}), (\mathrm{W_{Ca}}, \mathrm{S_{2Ca}})\}, \\ 0 & \text{otherwise.} \end{cases} \tag{47}$$

Then, the total ATP consumption during a cycle is:

$$V_{ATP}^{beat} = \frac{1}{d} \sum_{A} \int_{0}^{T_c} \int_{-\frac{d}{2}}^{\frac{d}{2}} \delta_{ATP}(A, B) \left(k_{B,A} n_B - k_{A,B} n_A \right) dx, \tag{48}$$

where T_c is the period of a beat.

Sarcomere dynamics. In the mechanical protocols where the sarcomere is allowed to shorten or lengthen, the sarcomere lengthening rate $v(t)$ is found by solving the equation

$$\sigma_a(t) =< predefined\, stress\, state > \tag{49}$$

for $v(t)$ at each integration time step of Eq. 27. For example, for physiological contraction, $v(t)$ is found such that the force produced by the sarcomere is the same as an afterload during the shortening phase. In isotonic phase, $\sigma_a(t) = const$. In isometric phase, the rate $v(t)$ is set to zero.

Fitting

Residuals. Model parameters were found by fitting the model solution to experimental data [20] with the goodness of the fit estimated by the least squares residuals. The least squares residuals were divided into three parts. The first part was obtained by comparing model solution to measured isometric force transients during a beat at different sarcomere lengths :

$$R_I = \sum_{i=1}^{N_{isom}} \left(\frac{P_{co}(l_i, t_i) - P_{ex}(l_i, t_i)}{(P_{max} - P_{co}(l_i, t_i)) \sqrt{N_{isom}}/10} \right)^2, \tag{50}$$

where P_{co} and P_{ex} are computed and measured stress, respectively; l_i is half-sarcomere length; t_i is the time moment for measurement point i; N_{isom} is the number of measurement points.

The second part of residuals was obtained by comparing the end-systolic points of physiological contraction at different afterloads with the end-systolic points of isometric contraction. Here, the physiological contractions were calculated by the model, and end-systolic points of isometric contraction were taken from Janssen et al measurements [20]:

$$R_{II} = \sum_{i=1}^{N_{isot}} \left(\frac{l^{es}_{isom}(i) - l^{es}_{phy}(i)}{(l_{phy} - l_{min})\sqrt{N_{isot}}/5} \right)^2 , \tag{51}$$

where l^{es}_{isom} and l^{es}_{phy} are end-systolic half-sarcomere lengths for isometric and physiological contractions, respectively; l_{phy} is an end-diastolic half-sarcomere length for the physiological contraction (1.05 nm); l_{min} is the minimum length of half-sarcomere (0.8 nm); and N_{isot} is the number of different afterloads used in optimization.

The third part of residuals was obtained by comparing the total amount of consumed ATP molecules per myosin head during a cardiac cycle found by the model with the amount expected from SSA assuming 65% efficiency [5]. This comparison was done for isometrical and physiological contractions:

$$R_{III} = \sum_{i=1}^{N_{SSA}} \left(\frac{V^{beat}(i)_{ATP}/SSA(i) - \eta}{\eta\sqrt{N_{SSA}}} \right)^2 , \tag{52}$$

where V^{beat} and SSA are the total ATP consumption and stress-strain area, respectively; η is 0.142 kJ^{-1} m^3 [5]; and N_{SSA} is the number of different afterloads and sarcomere lengths used in optimization.

Optimization parameters. In the optimization procedure, the model parameters are split into two sets. In the first set, the model parameter values were preset to certain values and all possible combinations of these parameter values were considered. For each of the combination of the model parameter values in the first set, the model parameter values in the second parameters set (see below) were optimized by the optimization algorithm. The optimal solution was found as one that had the smallest residual for all considered parameter sets.

The model parameters were divided into the two sets as follows. The first set consisted of five parameters describing free energy profiles shown at Fig. 4A: $G^{min}_{\mathrm{S}_1}$, x_1 defines the value and location (relative to the S_2 minimum) of minimal free energy in state $\mathrm{S}_{1\mathrm{Ca}}$; $G^{min}_{\mathrm{S}_2}$ is the minimal free energy in state S_2; $U_{\mathrm{W;S}}$ and $U_{\mathrm{T;W}}$ are components determining the tropomyosin free energy. For simulations with $q = 1$, $U_{\mathrm{W;S}}$ and $U_{\mathrm{T;W}}$ were set to zero.

The second set consisted of parameters describing piecewise linear functions of rate constants of the cross-bridge transformation reactions ($f_{\alpha,\beta}$, Eqs. 41). Without the influence of tropomyosin and taking into account microscopic reversibility (Eqs. 14), we have six independent cross-bridge cycling rates for every cross-bridge position. In addition, we assumed that Ca^{2+} association and dissociation rate constants are the same regardless to whether cross-bridge is in strong or weak binding state (transitions between W_{Ca} and T or $\mathrm{S}_{2\mathrm{Ca}}$ and S_2). As an example, rate profiles found after optimization are shown in Fig. 4B.

Optimized parameters for model with $q = 1$ were used as an initial solution for model with $q = 3$.

Numerical methods

The partial differential equations were discretized in cross-bridge position by the first order finite-difference method. The resulting system of ordinary differential equations was solved by using the DVODE package [32]. To speed up simulations, the original DVODE routines were modified to take into account the sparsity of the system and the parts of Jacobian matrix that were constant during a simulation.

For physiological contractions, the sarcomere lengthening rate $v(t)$ was found by assuming that the rate is constant for each integration time interval. The rate was varied by hybrd solver from MINPACK package [33] until the calculated stress at the end of the time interval was the same as the given afterload. The procedure was repeated for the next time interval by taking the solution found for the end of the previous time interval as an initial condition. The time interval was taken initially to 1 ms and was reduced in the case of failure of nonlinear solver by 4 times.

The model parameters were found by minimizing the least squares residuals. The optimization was performed using the Levenberg-Marquardt algorithm [34] interfaced with the main program using F2PY [35]. Simulations were performed on the cluster of Linux/Intel Xeon E5-2630L computers.

Supporting Information

Appendix. This appendix derives several equations describing cross-bridge dynamics. The appendix uses the same notations as the main text with only few new notations defined here.

Aim 1. Derivation of the equation describing dynamics of cross-bridge groups distribution function γ.

Derivation. The cross-bridge group cycling is described by dynamics of cross-bridge group density function $N_A(x_1, \ldots, x_q, t)$ with

$$\sum_A \int N_A(x_1, \ldots, x_q, t) dx_1 \cdots dx_q = 1, \tag{A.1}$$

$$\begin{aligned} \frac{\partial N_A(x_1, \ldots, x_q, t)}{\partial t} &+ \frac{\partial N_A(x_1 + \xi, \ldots, x_q + \xi, t)}{\partial \xi}\Big|_{\xi=0} v(t) \\ &= \sum_B (k_{B,A} N_B(x_1, \ldots, x_q, t) - k_{A,B} N_A(x_1, \ldots, x_q, t)), \end{aligned} \tag{A.2}$$

where $k_{A,B} = k_{A,B}(x_1, \ldots, x_q, t)$ are rate constants between biochemical states, $v(t)$ is the rate of the contractile element lengthening.

Let us define

$$\begin{aligned} N_A(x_1,\ldots,x_q,t) &= \gamma(x_1,\ldots,x_q,t)n_A(x_1,\ldots,x_q,t), && \text{(A.3)}\\ \sum_A n_A(x_1,\ldots,x_q,t) &= 1. && \text{(A.4)}\end{aligned}$$

Using this notation, we can rewrite Eq. A.2 as

$$\begin{aligned} \frac{\partial\,\gamma(x_1,\ldots,x_q,t)n_A(x_1,\ldots,x_q,t)}{\partial\,t} &+ \qquad \text{(A.5)}\\ \frac{\partial\,\gamma(x_1+\xi,\ldots,x_q+\xi,t)n_A(x_1+\xi,\ldots,x_q+\xi,t)}{\partial\,\xi}\bigg|_{\xi=0} v(t) &= \\ \sum_B (k_{B,A}\gamma(x_1,\ldots,x_q,t)n_B(x_1,\ldots,x_q,t) &- \\ k_{A,B}\gamma(x_1,\ldots,x_q,t)n_A(x_1,\ldots,x_q,t)) & \quad . \end{aligned}$$

To find γ, we sum up all the equations over all $A \in \mathbb{S}^q$. Taking into account property of n_A (Eq. A.4) and that the sum of all reaction rates is zero (there are no sources or sinks for cross-bridges), dynamics of $\gamma(x_1,\ldots,x_q)$ is described by

$$\frac{\partial\,\gamma(x_1,\ldots,x_q,t)}{\partial\,t} + \frac{\partial\,\gamma(x_1+\xi,\ldots,x_q+\xi,t)}{\partial\,\xi}\bigg|_{\xi=0} v(t) = 0. \tag{A.6}$$

The solution for Eq. A.6 with initial condition

$$\gamma(x_1,\ldots,x_q,t_0) = \gamma_0(x_1,\ldots,x_q) \tag{A.7}$$

is

$$\gamma(x_1,\ldots,x_q,t) = \gamma_0(x_1-a(t),\ldots,x_q-a(t)) \tag{A.8}$$

with

$$a(t) = \int_{t_0}^{t} v(\tau)d\tau. \tag{A.9}$$

Aim 2. Here we derive equations used to simulate dynamics of cross-bridge groups in the implemented model.

Derivation. In the implemented model, for the choice of γ_0 (in main text Eq. 26), γ is time independent and

$$\frac{\partial\gamma(x_1+\xi,\ldots,x_q+\xi,t)}{\partial\xi}\bigg|_{\xi=0} = 0. \tag{A.10}$$

The Eq. A.5 simplifies to

$$\begin{aligned}\frac{\partial n_A(x_1,\ldots,x_q,t)}{\partial t} \quad &+ \quad \frac{\partial n_A(x_1+\xi,\ldots,x_q+\xi,t)}{\partial \xi}\Big|_{\xi=0} v(t) \\ &= \sum_B (k_{B,A} n_B(x_1,\ldots,x_q,t) - k_{A,B} n_A(x_1,\ldots,x_q,t)).\end{aligned} \tag{A.11}$$

The following coordinate transformation

$$x'_1 = \frac{1}{q}\sum_{i=0}^{q} x_i, \tag{A.12}$$

$$x'_2 = x_2 - x_1, \tag{A.13}$$

$$\ldots$$

$$x'_q = x_q - x_1, \tag{A.14}$$

turns Eq. A.11 in to $1+1$ dimensional PDE:

$$\frac{\partial n'_A}{\partial t} + \frac{\partial n'_A}{\partial x'_1} v(t) = \sum_B (k'_{B,A} n'_B - k'_{A,B} n'_A), \tag{A.15}$$

with n'_A and $k'_{A,B}$ representing n_A and $k_{A,B}$ in a new coordinate system $(x'_1,\ldots,x'_q)$.

Acknowledgments

The authors are grateful to MSc P. Simson for useful discussions.

Funding

This research was supported by the European Union through the European Regional Development Fund (CENS Estonian Center of Excellence in Research). The funders had no role in study design, data collection and analysis, decision to publish, or preparation of the manuscript

References

1. Suga H. Ventricular energetics. Physiol Rev. 1990;70(2):247–277.
2. Hisano R, Cooper G. Correlation of force-length area with oxygen consumption in ferret papillary muscle. Circ Res. 1987;61(3):318–328.
3. Delhaas T, Arts T, Prinzen FW, Reneman RS. Regional fibre stress-fibre strain area as an estimate of regional blood flow and oxygen demand in the canine heart. J Physiol (Lond). 1994;477 (Pt 3):481–496.

4. Vendelin M, Bovendeerd PH, Engelbrecht J, Arts T. Optimizing ventricular fibers: uniform strain or stress, but not ATP consumption, leads to high efficiency. Am J Physiol Heart Circ Physiol. 2002;283(3):H1072–H1081.
5. Vendelin M, Bovendeerd PHM, Arts T, Engelbrecht J, Campen DHv. Cardiac mechanoenergetics replicated by cross-bridge model. Ann Biomed Eng. 2000;28(6):629–640.
6. de Tombe P. Cardiac myofilaments: mechanics and regulation. J Biomech. 2003;36(5):721–730.
7. Rice J, de Tombe P. Approaches to modeling crossbridges and calcium-dependent activation in cardiac muscle. Prog Biophys Mol Biol. 2004;85(2-3):179–195.
8. Hill TL. Theoretical formalism for the sliding filament model of contraction of striated muscle. Part I. Prog Biophys Mol Biol. 1974;28:267–340.
9. Eisenberg E, Hill TL, Chen Y. Cross-bridge model of muscle contraction. Quantitative analysis. Biophys J. 1980;29(2):195–227.
10. Pate E, Cooke R. A model of crossbridge action: the effects of ATP, ADP and Pi. J Muscle Res Cell Motil. 1989;10(3):181–196.
11. Månsson A. Actomyosin-ADP States, Interhead Cooperativity, and the Force-Velocity Relation of Skeletal Muscle. Biophys J. 2010;98(7):1237–1246.
12. Kalda M, Peterson P, Engelbrecht J, Vendelin M. A Cross-Bridge Model Describing the Mechanoenergetics of Actomyosin Interaction. In: Holzapfel GA, Kuhl E, editors. Computer Models in Biomechanics. Springer Netherlands; 2013. p. 91–102.
13. Razumova M, Bukatina A, Campbell K. Different Myofilament Nearest-Neighbor Interactions Have Distinctive Effects on Contractile Behavior. Biophys J. 2000;78(6):3120–3137.
14. Zahalak GI, Ma SP. Muscle activation and contraction: constitutive relations based directly on cross-bridge kinetics. J Biomech Eng. 1990;112(1):52–62.
15. Xu C, Craig R, Tobacman L, Horowitz R, Lehman W. Tropomyosin Positions in Regulated Thin Filaments Revealed by Cryoelectron Microscopy. Biophys J. 1999;77(2):985–992.
16. Behrmann E, Müller M, Penczek P, Mannherz H, Manstein D, Raunser S. Structure of the Rigor Actin-Tropomyosin-Myosin Complex. Cell. 2012;150(2):327–338.
17. Velden Jv, Moorman AF, Stienen GJ. Age-dependent changes in myosin composition correlate with enhanced economy of contraction in guinea-pig hearts. J Physiol (Lond). 1998;507 (Pt 2):497–510.
18. Gibbs CL, Barclay CJ. Cardiac efficiency. Cardiovasc Res. 1995;30(5):627–634.
19. Dobesh D, Konhilas J, de Tombe P. Cooperative activation in cardiac muscle: impact of sarcomere length. Am J Physiol Heart Circ Physiol. 2002;282(3):H1055 –H1062.
20. Janssen PM, Hunter WC. Force, not sarcomere length, correlates with prolongation of isosarcometric contraction. Am J Physiol. 1995;269(2 Pt 2):H676–H685.
21. Campbell S, Hatfield PC, Campbell K. A Mathematical Model of Muscle Containing Heterogeneous Half-Sarcomeres Exhibits Residual Force Enhancement. PLoS Comput Biol. 2011;7(9):e1002156.
22. Rice J, Wang F, Bers D, Tombe Pd. Approximate Model of Cooperative Activation and Crossbridge Cycling in Cardiac Muscle Using Ordinary Differential Equations. Biophys J. 2008;95(5):2368–2390.
23. Taylor TW, Goto Y, Hata K, Takasago T, Saeki A, Nishioka T, et al. Comparison of the cardiac force-time integral with energetics using a cardiac muscle model. J Biomech. 1993;26(10):1217–1225.
24. Taylor TW, Goto Y, Suga H. Variable cross-bridge cycling-ATP coupling accounts for cardiac mechanoenergetics. Am J Physiol. 1993;264(3 Pt 2):H994–1004.
25. Rice J, Stolovitzky G, Tu Y, de Tombe P. Ising Model of Cardiac Thin Filament Activation with Nearest-Neighbor Cooperative Interactions. Biophys J. 2003;84(2):897–909.

26. Tanner BW, Daniel T, Regnier M. Filament Compliance Influences Cooperative Activation of Thin Filaments and the Dynamics of Force Production in Skeletal Muscle. PLoS Comput Biol. 2012;8(5):e1002506.
27. Smith DA, Geeves MA. Cooperative Regulation of Myosin-Actin Interactions by a Continuous Flexible Chain II: Actin-Tropomyosin-Troponin and Regulation by Calcium. Biophys J. 2003;84(5):3168–3180.
28. Zou G, Phillips GN. A cellular automaton model for the regulatory behavior of muscle thin filaments. Biophys J. 1994;67(1):11–28.
29. Campbell S, Lionetti F, Campbell K, Mcculloch A. Coupling of Adjacent Tropomyosins Enhances Cross-Bridge-Mediated Cooperative Activation in a Markov Model of the Cardiac Thin Filament. Biophys J. 2010;98(10):2254–2264.
30. Hill TL. Theoretical formalism for the sliding filament model of contraction of striated muscle. Part II. Prog Biophys Mol Biol. 1975;29(2):105–59.
31. Kojima H, Ishijima A, Yanagida T. Direct measurement of stiffness of single actin filaments with and without tropomyosin by in vitro nanomanipulation. PNAS. 1994;91(26):12962 –12966.
32. Brown PN, Byrne GD, Hindmarch AC. VODE: a variable coefficient ODE Solver. SIAM J Sci Stat Comput. 1989;10:1038–1051.
33. Moré JJ, Sorensen DC, Hillstrom KE, Garbow BS. The MINPACK Project. In: Cowell WJ, editor. Sources and Development of Mathematical Software. Prentice-Hall; 1984. p. 88–111.
34. Powell MJD. A Hybrid Method for Nonlinear Equations. In: Rabinowitz P, editor. Numerical Methods for Nonlinear Algebraic Equations. Gordon and Breach; 1970. p. 87–114.
35. Peterson P. F2PY: a tool for connecting Fortran and Python programs. Int J Comput Sci Eng. 2009;4(4):296 – 305.

PUBLICATION III

Peterson P, Kalda M, Vendelin M

Real-time determination of sarcomere length of a single cardiomyocyte during contraction.

American Journal of Physiology - Cell Physiology, 2013, 304(6), C519–531.

Am J Physiol Cell Physiol 304: C519–C531, 2013.
First published December 19, 2012; doi:10.1152/ajpcell.00032.2012.

Real-time determination of sarcomere length of a single cardiomyocyte during contraction

Pearu Peterson, Mari Kalda, and Marko Vendelin
Laboratory of Systems Biology, Institute of Cybernetics, Tallinn University of Technology, Tallinn, Estonia

Submitted 27 January 2012; accepted in final form 17 December 2012

Peterson P, Kalda M, Vendelin M. Real-time determination of sarcomere length of a single cardiomyocyte during contraction. *Am J Physiol Cell Physiol* 304: C519–C531, 2013. First published December 19, 2012; doi:10.1152/ajpcell.00032.2012.—Sarcomere length of a cardiomyocyte is an important control parameter for physiology studies on a single cell level; for instance, its accurate determination in real time is essential for performing single cardiomyocyte contraction experiments. The aim of this work is to develop an efficient and accurate method for estimating a mean sarcomere length of a contracting cardiomyocyte using microscopy images as an input. The novelty in developed method lies in *1*) using unbiased measure of similarities to eliminate systematic errors from conventional autocorrelation function (ACF)-based methods when applied to region of interest of an image, *2*) using a semianalytical, seminumerical approach for evaluating the similarity measure to take into account spatial dependence of neighboring image pixels, and *3*) using a detrend algorithm to extract the sarcomere striation pattern content from the microscopy images. The developed sarcomere length estimation procedure has superior computational efficiency and estimation accuracy compared with the conventional ACF and spectral analysis-based methods using fast Fourier transform. As shown by analyzing synthetic images with the known periodicity, the estimates obtained by the developed method are more accurate at the subpixel level than ones obtained using ACF analysis. When applied in practice on rat cardiomyocytes, our method was found to be robust to the choice of the region of interest that may *1*) include projections of carbon fibers and nucleus, *2*) have uneven background, and *3*) be slightly disoriented with respect to average direction of sarcomere striation pattern. The developed method is implemented in open-source software.

heart muscle; sarcomere length; microscopy image analysis; autocorrelation analysis; fundamental period

AS AN EXPERIMENTAL MODEL, isolated cardiomyocytes provide unique opportunities to study electrophysiology, mechanics, and bioenergetics. To bring this experimental model closer to the in vivo environment, mechanical contraction of cardiomyocytes can be induced through electrical stimulation and controlled by attached carbon fibers (23, 22). To induce a mechanical loading protocol on a single cardiomyocyte, carbon fibers can be moved leading to isometric or shortening contractions. However, similar to isometric contraction of the muscle fiber (10), it has been demonstrated that there is a shortening of sarcomeres in the middle of cardiomyocyte while the distance between carbon fibers or cell length stays constant (16, 5). Due to several technical difficulties in performing isosarcometric contraction experiments using real-time feedback, adaptive feed-forward control systems are commonly used to control the distance between carbon fibers leading to an inability to perform isosarcometric contraction experiments (16, 5). One of the technical problems in achieving real-time feedback control for isosarcometric experiments is the determination of the mean sarcomere length, the problem that is addressed in this work. While several methods exist, many of them suffer from inaccuracies. As demonstrated in this work and earlier by others (see below), methods based on autocorrelation function (ACF) and spectral analysis of microscopy images have several drawbacks that preclude their use in the real-time estimation of sarcomere length for feedback control of the contraction where the accuracy of control input such as the sarcomere length is of importance.

Whatever experimental technique is used for capturing data with sarcomere length information, various signal analysis methods have to be applied to estimate the mean sarcomere length of a cardiomyocyte under a microscope. A common task for all methods is to quantify some measure of repetition contained in captured data and relate this measure to the sarcomere length. For simplicity, we assume that the captured data are in the form of microscopy images acquired with a high-speed camera. This is also a practical simplification as transmission images with sarcomere length information additionally contain carbon fiber positional information that is needed for mechanical loading protocols. This information would not be readily available when using, for instance, laser-light diffraction-based techniques (7, 9, 11).

There are several requirements for the method of sarcomere length determination to make it useful in real-time control of cardiomyocyte contraction. First, it must be accurate at subpixel resolution to allow the usage of faster cameras that have smaller resolution parameters. Second, the method must be robust to a selection of region of interest (ROI) size. Using smaller ROI facilitates localized estimation of the mean sarcomere length as well as consumes less computational resources that may be essential for real-time control protocols. Because of the exact alignment of ROI to the sarcomere striation pattern is practically impossible due to continuous variations of the sarcomere orientations during contraction, the method must also be robust to the selection of ROI orientation. Third, the method must be robust in regions of ROI where the sarcomere signal is weak or even absent due to nonfavorable optical conditions and cell morphology or due to the presence of some external objects such as carbon fibers holding a cardiomyocyte. Finally, the method must have efficient implementation to ensure that the mean sarcomere length is determined before the next image frame from a high-speed camera arrives.

The sarcomeres appear in a transmission image of a cardiomyocyte as repeating patterns of darker and lighter regions of Z-disks and I-A-bands, respectively, forming a sarcomere striation pattern. The mean sarcomere length is defined as the spatial period of this pattern.

Address for reprint requests and other correspondence: P. Peterson, Laboratory of Systems Biology, Institute of Cybernetics, Tallinn Univ. of Technology, Akadeemia 21, 12618 Tallinn, Estonia (e-mail: pearu@sysbio.ioc.ee).

ISSN 0363-6143.

Several systems exist that can measure the mean sarcomere length from microscopy images in real time. The software SarcLen provided by IonOptix employs a fast Fourier transform (FFT) to determine the mean frequency of sarcomere spacing (Sarclen Algorithm, Technical Report, IonOptix, 2010). The software HVSL by Aurora Scientifica implements similar FFT-based algorithm as well as two ACF-based algorithms (Instruction Manual: Model 901A, Aurora Scientific, 2008). In the ACF-based algorithms, the sarcomere spatial frequency is determined either by applying an FFT-based algorithm to the ACF or by fitting it with a sine function with the frequency corresponding to the mean sarcomere spatial frequency. Both systems can measure sarcomere length at subpixel resolution by using quadratic approximation at the peak of the discrete frequency spectrum. However, in the FFT-based methods, the accuracy of the mean sarcomere length estimate strongly depends on a mismatch of pixel values at ROI ends due to the extension of ROI into periodic function, as FFT-based methods inherently do. In addition, the mismatch of pixel values at ROI boundaries changes during the cardiomyocyte contraction making it impossible to compensate such boundary effects, for example, by varying the signal length. These boundary effects can be observed, for example, in the mean sarcomere length evolution during the contraction: the sarcomere length rate may contain spurious peaks (Instruction Manual: Model 901A, Aurora Scientific, 2008), especially when measuring sarcomere length from a relatively small ROI. To suppress the boundary effects of the FFT-based methods, one can select a longer ROI that contains more sarcomeres and use Hann window filtering (4) or use ACF-based methods, as the above-mentioned commercial systems do.

The aim of this work is to develop an accurate and efficient computational method for determining the mean sarcomere length from transmission images of a single contracting cardiomyocyte and provide its implementation in an open-source software package. The developed method is first evaluated on using artificial signals with know periodicity and then is applied to a sequence of microscopy images of a cardiomyocyte taken during the contraction. Various sensitivity properties of the mean sarcomere length are analyzed to estimate the applicability of the developed method in practice. Finally, two example experiments are provided where the mean sarcomere length is estimated while varying preload and stimulation conditions.

GENERAL DESCRIPTION OF THE MEAN SARCOMERE LENGTH DETECTION ALGORITHM

There are different kinds of errors that determine the accuracy of the mean sarcomere length estimated from a microscopy image: *1*) imperfect objective field caused by uneven illumination and presence of objects other than sarcomeres, *2*) restrictions and uncertainties in acquisition process leading to sampling errors and noisy data, and *3*) systematic errors from used algorithms.

This work aims at establishing the best algorithm that is robust to errors in input data and is exact for perfectly periodic input data, that is, the best algorithm must have no systematic errors.

Main Algorithm

In simplified notation, as a basic algorithm to determine the mean sarcomere length of a cardiomyocyte, we propose to use least squares difference between the image and its shifted copy. Indeed, in the ideal case with the periodic signal on the image, shifting the image by one period would lead no difference between the original and shifted copy. In reality, we expect that the minima of the least squares difference will be obtained when the shift between image and its copy is close to the mean sarcomere length value. In the following text, we will denote the proposed algorithm as a "method of current work."

For comparison of the results of current work we use two other conventional methods for estimating the mean sarcomere length.

The first method, labeled as the "Fourier spectrum" method, is based on calculating the power spectrum of a signal. The maximum point of the power spectrum is related to the fundamental spatial frequency of the signal, which, in turn, is inversely proportional to the fundamental period, i.e., the mean sarcomere length when applied on the transmission image of a cardiomyocyte. The second method, labeled as the "ACF" method, is based on calculating the ACF. The first positive maximum point of the ACF is related to the fundamental period of the signal and can be used to estimate the mean sarcomere length.

The main difference between the algorithm proposed in this work, and "Fourier spectrum" and "ACF" methods, is in the treatment of the boundaries of the image. Let us assume that the sarcomeres are aligned along the image lines. As it will be demonstrated in RESULTS, "Fourier spectrum" and "ACF" methods suffer from the difference of the signal on the opposing boundaries of the image leading to the systematic error in the mean sarcomere length estimation.

Subpixel Resolution

In addition to the performance of the underlying algorithm, the accuracy of the mean sarcomere length is strongly influenced *1*) by the size of pixels of microscopy images and *2*) by the number of pixels containing sarcomere striation pattern data. These parameters are especially important because microscopy imaging provides a rather sparse representation of the sarcomere striation pattern. For example, in a typical microscopy image of a rat cardiomyocyte (see MATERIALS AND METHODS), a single sarcomere unit is represented only by four or five pixel values per image line as determined be the ratio of a typical sarcomere length (1.8 μm) and pixel size (0.4 μm). On the other hand, the area within a microscopy image of cardiomyocyte where sarcomere striation pattern is more-or-less uniform and well visible, is always restricted, first, by the overall size of a cell; second, by variable morphology of the cell; and finally, by the presence of external objects such as carbon fibers used to fix the cell. Under these restriction of data acquisition, we aim at resolving the mean sarcomere length of a cardiomyocyte with subpixel resolution. For that we use piecewise linear representation of the object field under microscopy; compare this to the actual piecewise constant representation of the object field where the neighboring pixels are considered unrelated. By using linear interpolation we could derive analytical equations that allow us to estimate the mean sarcomere length with subpixel resolution using all three methods considered in this work.

Image Filtering by Detrending

Assuming that the cardiomyocyte is aligned along the image lines, a typical line profile of a microscope transmission image of a cardiomyocyte contains variations that have different origins: sarcomere striation patterns, nuclei, external objects, etc. For our analysis, it is important to separate variations in *1*) image intensity induced by periodic intracellular structures and *2*) background. To decompose a sample sequence into the corresponding oscillatory and slowly varying parts, we use a simple but efficient method that takes advantage of knowing the spatial period of oscillations, that is, the initial estimate of the mean sarcomere length. For that, images are blurred with the kernel that has a half-width of ~1/10 of sarcomere length, and through processing of local maxima, the oscillatory part is extracted. The performance of the algorithm is described in RESULTS and details are given in APPENDIX.

MATERIALS AND METHODS

This study develops a method for estimating the mean sarcomere length of a cardiomyocyte from a transmission image in real time. Here, experimental and numerical methods are described. A mathematically rigors description of the algorithms is given in APPENDIX.

Ethics Statement

Animal procedures were approved by the Estonian National Committee for Ethics in Animal Experimentation (Estonian Ministry of Agriculture).

Cardiomyocyte Isolation

Adult outbred Wistar rats of both sexes weighing between 300 and 500 g were used in the experiments. Cardiomyocytes are isolated as described by Sepp et al. (20) with modifications from Jepihhina et al. (8).

Solutions

Cells were imaged in a HEPES-Tyrode solution containing the following (in mM): 137 NaCl (71379; Sigma-Aldrich), 5.4 KCl (P5405; Sigma-Aldrich), 2.0 $CaCl_2$ (21097; Sigma-Aldrich), 0.5 $MgCl_2$ (63068; Sigma-Aldrich), 0.33 NaH_2PO_4 (Fluka Analytical; 71633), 5 HEPES (H3375; Sigma-Aldrich), and 5 glucose (158968; Sigma-Aldrich), pH 7.4 adjusted by NaOH (30531; Fluka Analytical) at 25°C.

Imaging

Microscope experiments were performed on an inverted Nikon Eclipse Ti-U microscope (Nikon, Amstelveen, The Netherlands) equipped with a high-speed CCD camera (IPXVGA210-LMCN; ImperX), with a ×40 long working distance objective (CFI S Plan Fluor ELWD 40×/0.6; Nikon).

To ensure the immobility of cardiomyocytes during contraction we used a carbon fiber technique (22) with bidirectional control setup (5). Carbon fibers (Tsukuba Material Information Laboratory) that were mounted in glass capillaries (TW150–3; WPI, Sarasota, FA) were attached to an isolated cardiomyocyte using two micromanipulators (PatchStar Micromanipulator; Scientifica, East Sussex, UK). For manipulating carbon fibers, nanopositioners (Nano-OP100; MCL) were mounted to micromanipulators. For field stimulation, we used stimulator (module 2100; A-M Systems). For example experiments, the carbon fibers were coated with a biological adhesive, MyoTak (IonOptix, Dublin, Ireland), to improve their attachment to cardiomyocytes.

Solution with cells was placed on a cover glass of 0.15 mm in thickness (CS-24/50; Warner Instruments, Harvard Apparatus). The cover glass was coated with 2-hydroxyethyl methacrylate (Sigma-Aldrich, P3932) to prevent the adhesion of cardiomyocytes.

Supporting Software

The algorithms for detrending image arrays and estimating the fundamental period of images were implemented in C for efficiency and exposed to Python using f2py (18) for efficient prototyping. The source code is available in the IOCBio Google Code project (http://iocbio.googlecode.com/). The source code of integrals of piecewise polynomial functions was generated using Sympycore (http://sympycore.googlecode.com/). To compute FFT of sequences, we used single threaded double precision FFT routines from the FFTW software library (2).

Hardware

The tests for measuring the timings of the algorithms considered (the mean sarcomere length estimation and FFT) were performed on a Ubuntu Linux computer with a dual-core AMD Phenom(tm) II X2 550 CPU and 4 GB RAM.

RESULTS

In this section we present the following findings of this work: *1*) conventional ACF-based sarcomere length determination methods introduce systematic errors when applied to images; the current work is providing a method that does not produce these systematic deviations. *2*) The method of current work is applied to microscopy images for determining the mean sarcomere length of a contracting cardiomyocyte. We describe the corresponding procedure, analyze sensitivity of the method to different uncertainties that are inherent to the corresponding experimental conditions, and compare the dynamics of the mean sarcomere length time evolutions obtained from different methods: the method of current work and two methods based on discrete ACF and Fourier spectrum analysis, respectively. Finally, we demonstrate the method of current work on estimating sarcomere lengths for two example experiments of cardiomyocytes.

General Properties of Used Algorithms

ACF has a systematic error in sarcomere length estimation. As a simple example, let us assume that sarcomeres induce perfectly periodic image with transmission signal on each line equal to simple sinusoidal function, $f(x) = \sin(2\pi x/P)$. Clearly, the period P corresponds to the sarcomere length. To develop methods for estimating the mean sarcomere length, P_{est}, from an image with periodic content, we consider three approaches: *1*) the method of current work that assumes that image has strictly finite size, *2*) the conventional ACF-based method that inherently assumes that image length is made infinite by zero-padding, and *3*) the conventional periodic ACF-based method that inherently assumes that image length is made infinite by repeating the image periodically in space. (The corresponding similarity measures that define these three methods, are F^E, F^A, and F^A_{periodic}, respectively, all defined in APPENDIX.) As a first example, we will estimate sarcomere length assuming that the signal is known perfectly within every pixel (a pixel carries the signal as a function rather than a single value) and the integrals corresponding to each of the methods can be found analytically. In other words, there are no artifacts induced by pixelation of the image. The defects from pixelation are demonstrated by the second example.

The relative errors of the period estimates are shown in Fig. 1 for three different lengths (N) of image lines. While the length N in the following example will be in pixels, here it is in arbitrary units due to the perfect image resolution used in this example. As seen on the plot Fig. 1*A*, the period estimated by ACF-based methods is modulated. The length is underestimated and overestimated, depending on the relative length of the signal period and the image line. Using the method proposed in the current work, however, always results in an exact period (relative error is identical to zero), regardless of the length of the image line or the choice of signal extension at ROI ends.

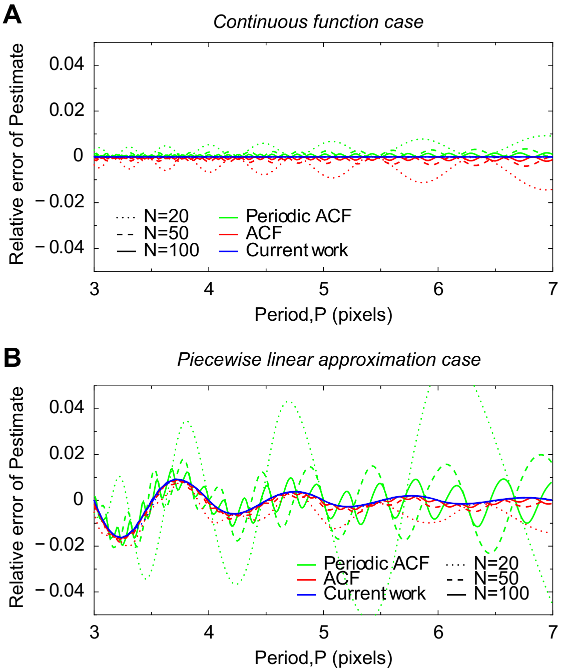

Fig. 1. Sensitivity test of sarcomere length estimation algorithms to boundary conditions of a continuous function (*A*) and its piecewise linear approximation (*B*). Continuous function corresponds to "transmission image" (with length N) intensity having a form $f(x) = \sin(2\pi x/P)$ where P is the exact period and $0 \leq x \leq N - 1$. The continuous function is then approximated with a linear spline having pixel values $f_i = \sin(2\pi i/P)$, $i = 0; \ldots ; N - 1$. *A* and *B* show the relative error of the period estimate P_{est}, $P_{est}/P - 1$, using three different methods, indicated with different line colors, and for different number of single sine waveforms per domain length, defined as the ratio N/P, and on plot indicated with different line styles. *A*: note that with N fixed and varying P the estimates predicated by the autocorrelation function (ACF) and periodic ACF analysis methods have modulated systematic errors due to imposed periodic boundary conditions: when for given N and P, the boundary values and slopes of $f(x)$ at different ends are different, the error will be large, and when they are close, the error will be small. With the method established in this work, the estimated period is equal to the exact period for all N and P values. This indicates that this method is insensitive to the possible mismatch of boundary values at different ends of image lines. *B*: estimated periods from the all considered methods are modulated. For the method established in this work, this modulation diminishes for longer waveforms (larger P) because the linear approximation error will be smaller regardless of the number of waveforms per domain length (lines for different span, N, almost coincide). In contrast, period estimates from ACF and periodic ACF analysis methods have larger modulation amplitudes that will increase for longer waveforms. This is due to the mismatched boundary conditions as shown in *A*.

Note that the increase of modulation amplitude of P_{est} with the increase of P is directly related to the mismatch of signal at the opposing ends of the image line that all ACF-based methods inherently fail to handle. Indeed, from one hand, the number of repetitive patterns in a signal is proportional to N/P, and on the other hand, the contribution of repetitive patterns to the formation of ACF signal is proportional to the number of repetitive patterns; therefore, the relative contribution of mismatching boundary conditions to the ACF signal is greater when the number of repetitive patterns is smaller, or equivalently, P is larger.

Finally, we note that the modulation frequency of P_{est} is increasing when increasing the length of interval N. In linearly varying period P, the modulation frequency will manifest itself as plateaus in the plot of estimated period P_{est} (result not shown).

Defects from image representation by pixels. In practice, image intensity is given at discrete points and exact analytical evaluation of similarity measures used to determine the sarcomere length (as used in Fig. 1*A*) is not possible. To be able to evaluate sarcomere length at subpixel resolution, we use linear interpolation of the signal between pixels. The inaccuracy of piecewise linear approximation, however, introduces specific errors in the estimated sarcomere length. To demonstrate this, we consider again an image represented by sinusoidal function (see above) and use its values determined on N pixels in an image line. Similar to the above approach, we keep the number of pixels fixed and vary P. Note that the corresponding integrals are evaluated using semianalytic, seminumeric approach (see APPENDIX). The relative errors of the corresponding estimates are given in Fig. 1*B* for three different lengths of image lines. We see that the usage of linear interpolation introduces P_{est} oscillations around the expected sarcomere length for all considered methods.

The estimation errors of sarcomere length, manifested by the oscillations of P_{est}, have two components. One is from mismatching boundary conditions that are the cause of increasing modulation amplitude when P is increased (see previous analysis on continuous signal functions). Note that this component is present, and it dominates, in the case of both ACF-based methods. The second component is due to piecewise linear approximation that has greater influence when the number of points per repetitive pattern is small, that is, when the representation of a signal function via piecewise linear interpolation is less adequate. With the increase of P, the errors from piecewise linear approximation decrease because the quality of piecewise linear representation increase. The outcome of this analysis is exemplified in Fig. 1*B* by the curve corresponding to the method of current work.

Applications to Images of Cardiomyocyte

In the following we analyze different methods for estimating the mean sarcomere length of a cardiomyocyte. The methods are applied to microscopy images of a contracting cardiomyocyte that are held in microscope focus using two carbon fibers. Below we analyze in detail the case where the cardiomyocyte has no load applied other than the force generated by the elasticity of deforming carbon fibers. Finally, two example experiments with different preload and stimulation conditions on cardiomyocytes are presented.

Estimating the mean sarcomere length from a microscopy image of a cardiomyocyte. The procedure of estimating the mean sarcomere length of a cardiomyocyte is exemplified in Fig. 2 and explained as follows. The procedure starts with acquiring a transmission image of a cardiomyocyte (Fig. 2*A*) and selecting a ROI (Fig. 2*B*) for subsequent image preprocessing step. The aim of the preprocessing step is to discard any nonperiodic content from the ROI image. For that we use the detrend algorithm (Fig. 2*C*, see APPENDIX for detailed description) that decomposes each line of the ROI image into oscillatory part (Fig. 2*D*) and slowly varying part (Fig. 2*E*). The image analysis continues by applying the sarcomere length estimation algorithm to the oscillatory part of the ROI image (Fig. 2*F*; the slowly varying part is discarded but is shown in Fig. 2*G* for illustration purposes). As explained in detail in APPENDIX, the sarcomere length estimate is defined as the first positive minimum point of a similarity measure; here we use F^E that is similarity measure proposed by the current work and that turns out to be most appropriate for images. When estimating sarcomere length from multiple image lines, such as selected ROI, two approaches are possible: *1*) compute the similarity measure of ROI image as the sum of similarity measures of each image line and then find the minimum point of the similarity measure or *2*) find the minimum points of similarity measures computed for each line and then compute the mean minimum point. Figure 2, *H* and *I*, illustrates that the two approaches lead to slightly different results. In this particular case, the approach with the superposition of similarity measures of ROI lines (blue line in Fig. 2*H*) leads to a sarcomere length equal to 4.32 pixels, while the average of all minimum points (red crosses in Fig. 2*I*) of similarity measures is 4.33 pixels. For the rest of this study, we choose to use the first approach as it appears to be more robust in practice. For instance, it is possible that a few lines in a ROI image contain no sarcomere striation pattern information, and therefore, the estimation of fundamental period on those lines is impossible and the second approach becomes less reliable. Finally, taking into account the pixel size of the microscopy image, we obtained the mean sarcomere length. In our microscope setup, the pixel size is 0.411 μm, and therefore, the mean sarcomere length is estimated to be $4.32 \times 0.411\ \mu m \approx 1.775\ \mu m$ for the given time moment of cardiomyocyte contraction.

Sensitivity analysis of the choice of ROI. In practice, the results of the mean sarcomere length estimation procedure (Fig. 2) may strongly depend on the choice of ROI either because of heterogeneity of sarcomere striation patterns within a single cardiomyocyte or because of various experimental conditions that may influence the visibility of sarcomeres. Therefore, understanding the sensitivity of the choice of ROI is important when selecting the ROI for sarcomere length analysis. In general, the choice of ROI is characterized by its location, size, and orientation with respect to the original image. In the following we analyze how each parameter of ROI influences the estimation of the mean sarcomere length when applied to the same microscopy images of a cardiomyocyte. Due to extensive computations, use of full sensitivity analysis in real time is probably impossible, unless some specialized computational techniques are utilized.

Figure 3 shows how the mean sarcomere length estimate depends on the size of ROI and its location in an overall image. Usage of smaller ROI sizes reveals a slight heterogeneity of the mean sarcomere length within a cardiomyocyte microscopy image. This heterogeneity can be explained by the heterogeneous morphology of cardiomyocyte that partly appears in the form of dislocations of the repeating patterns in the microscopy image. With larger ROI sizes, this heterogeneity is averaged out and the mean sarcomere length is stable with respect to the choice of ROI location, even in the proximity of attached carbon fibers. On the other hand, a selection of larger ROI increases the computational requirements of the mean sarcomere length estimation, although this increase has no practical influence as the typical acquisition frame time is an order of magnitude larger than the typical time of sarcomere length estimation [for a typical 54 × 31 (length × height) ROI size it takes ~16 ns to estimate the mean sarcomere length on our computer platform].

Figure 4 illustrates how different ROI orientations affect the result of the mean sarcomere length estimation. Because the original image data are given on a rectangular grid, we use bilinear interpolation to compute the ROI image data on the rotated rectangular grid. Notice that the mean sarcomere length estimate is approximately inversely proportional to the cosine of ROI orientation angle. This follows from a general consideration of cutting a *P*-periodic lattice of lines at the orientation angle α leading to the formula $P/\cos(\alpha - \alpha_0)$ that defines the period of the cut structure. Here α_0 corresponds to the optimal orientation of the periodic lattice. In other words, by estimating sarcomere length from ROI where the sarcomeres are not aligned along the lines, the estimated sarcomere length is by $1/\cos(\alpha - \alpha_0)$ larger than the length corresponding to the cardiomyocyte. Such analysis could be used to eliminate the small deviation in the mean sarcomere length estimate due to the imperfect choice of ROI orientation. In the given example, the optimal orientation of ROI is found to be at the angle $-4.72°$ and the improved estimate to the mean sarcomere length is obtained by multiplying the original estimate of the mean sarcomere length with a correction factor $\cos 4.72° \approx 0.997$. Below we also report how the contraction of a cardiomyocyte affects the optimal orientation of a ROI and how the estimate of the mean sarcomere length is influenced by that.

Time evolution of the mean sarcomere length in a contracting cardiomyocyte. The time evolution of the mean sarcomere length estimate during one cardiomyocyte contractions is shown in Fig. 5. The plot is produced from CCD camera images recorded at 200 Hz (time resolution is 5 ms). At *top*, the mean sarcomere length estimates from three different methods are shown. The ROI size in all cases is 54 × 31.

First, the method based on Fourier spectrum analysis provides worst estimates as during the evolution of the mean sarcomere length smooth plateaus appear. When selecting a longer ROI with more sarcomeres in the image line, the steps between the plateau levels will the decrease (result not shown for brevity). Note that this behavior is manifestation of systematic modulation frequency in sarcomere length estimation methods that are based on Fourier spectrum analysis (see Fig. 1*A*). Therefore, to suppress these artificial plateaus, one should increase the length of a ROI.

Second, when using the quadratic approximation of averaged ACF of ROI image lines, the phenomenon of plateaus in

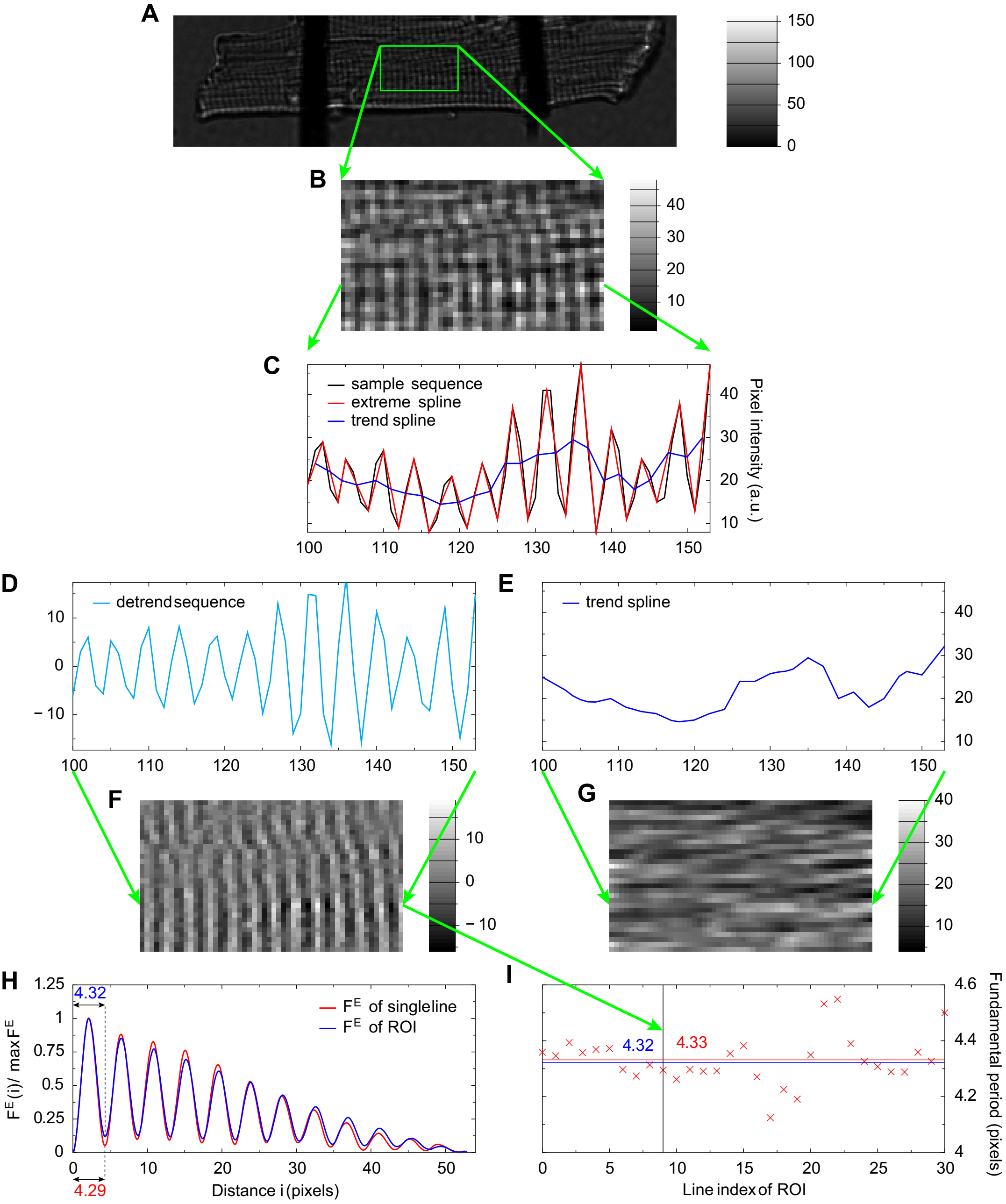

Fig. 2. Determination of the mean sarcomere length from a regions of interest (ROI) of the microscopy image of a cardiomyocyte (*A*). The detrend algorithm is applied to each line of ROI (*B*, size is 54 × 31) that decomposes the line signal to oscillating and slowly varying parts. These parts correspond to sarcomere striation pattern and uneven background, respectively. *C-E*: decomposition of the 10th line of the ROI. *F* and *G*: results of the detrend algorithm applied to all lines in the ROI image. Next, the fundamental period (i.e., sarcomere length) of the sarcomere striation pattern is estimated as the minimum point of the similarity measure (F^E) shown in *H* for the 10th line and for the whole ROI. *I*: illustrates how the sarcomere length estimates from single lines (red crosses, average is 4.33) relate to the estimate from the ROI image (blue level line at 4.32).

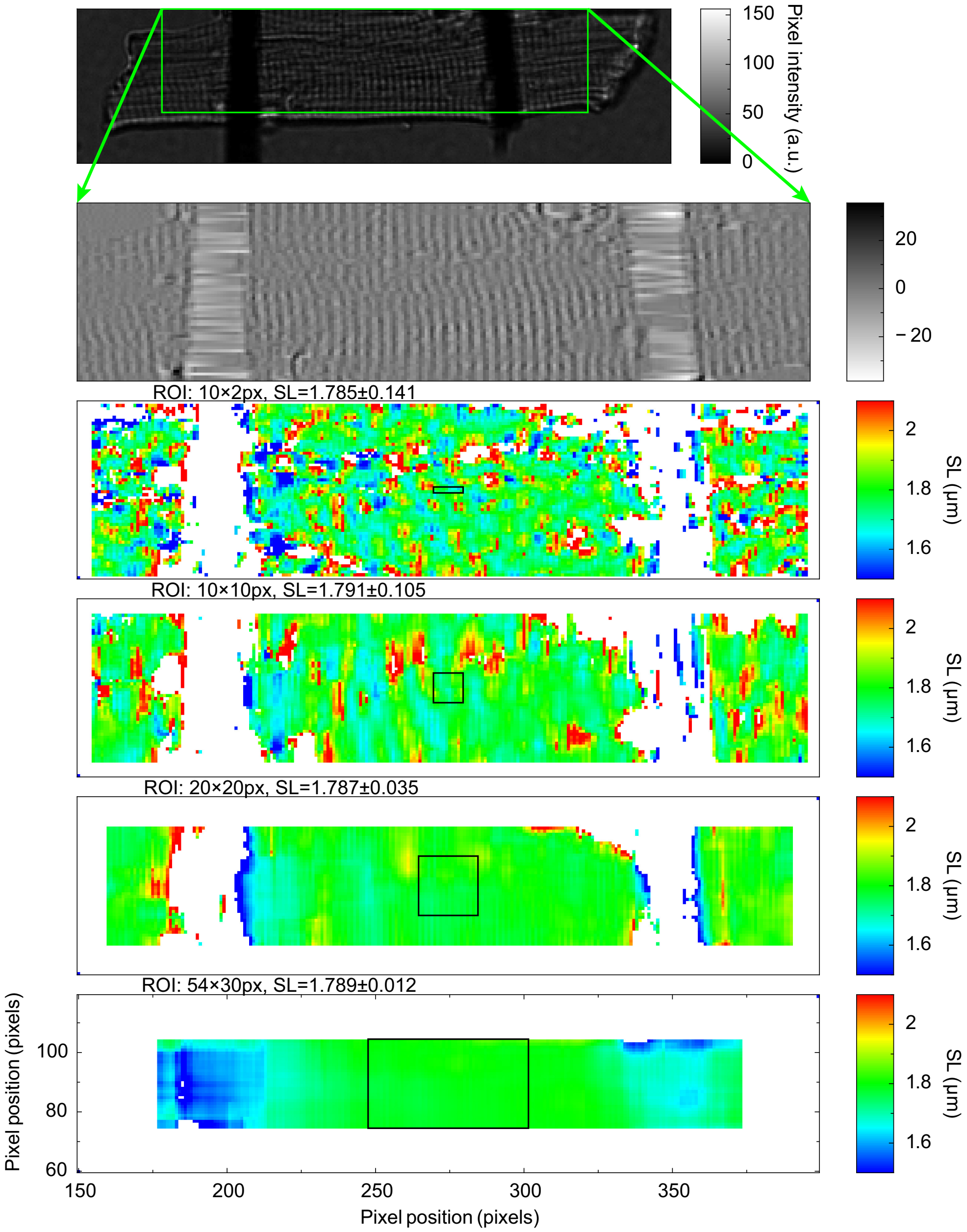

Fig. 3. Sensitivity analysis of sarcomere length (SL) estimation to ROI size and location. A periodic content of a region in a transmission image of a cardiomyocyte is found (*top two plots*). The mean sarcomere length is computed for each point of the region using different ROI sizes (*bottom four plots*). The ROI size used is illustrated with a black box. White pixels denote regions where the sarcomere length could not be computed due to a lack of sarcomere signal or due to the presence of carbon fibers. Each pixel value, indicated by color bar at *right*, corresponds to the mean sarcomere length estimate obtained from a ROI that center is located at the given pixel position and that has specified size. For small ROIs, heterogeneity of sarcomere length within the cardiomyocyte is notable (*top two color plots*). Usage of larger ROIs provides the mean sarcomere length that is insensitive to the position of the ROI (*bottom two color plots*).

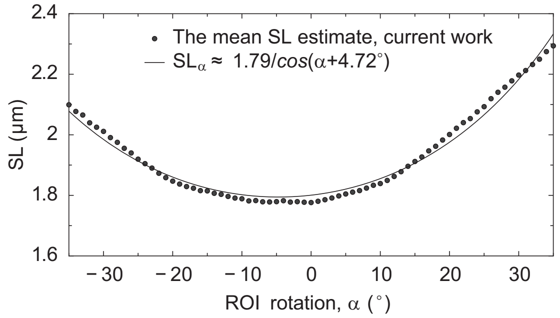

Fig. 4. Sensitivity analysis of the mean sarcomere length estimation to the selection of ROI orientation. The mean sarcomere length estimate is inversely proportional to the cosine of ROI orientation angle. The minimum point corresponds to ROI orientation that coincides with the orientation of sarcomeres and, hence, leads to a corrected estimate of the mean sarcomere length.

sarcomere length evolution is somewhat reduced but still notable. We suspect that these plateaus have the same origin as in the method based of Fourier spectrum analysis.

Third, the method developed in the current work (see APPENDIX) gives sarcomere length estimates with no apparent artifacts other than small noise. Notice that the mean sarcomere length estimates differ from each other up to 2.5% in both directions. For instance, at the resting state the Fourier spectrum estimate is ~2.5% larger than the estimates from methods using ACF or of current work; at the maximal contraction moment it is ~2.5% smaller than the estimate from the method of current work. This difference is in agreement with the analysis of estimating the period of a discrete sine function where the relative error of the estimates can be up to 2% (in Fig. 1*B*, consider the curve corresponding to the periodic ACF-based method and $N = 50$, which is closest to considered ROI image length 54; the relative error is estimated around the point 4.3). Therefore, we conclude that the differences in the mean sarcomere length estimates are due to *1*) boundary artifacts and *2*) piecewise linear interpolation approximation of the intensity field. The former dominates the latter in the case of Fourier spectrum and ACF analysis-based methods, while for the method of current work it is not present, and only the latter can cause relative errors up to 1%. We note that estimating the relative errors of the mean sarcomere length based on Fig. 1*B* is plausible if the amplitude of the signal is constant, as in the artificial examples in Fig. 1. Otherwise, the amplitude variations such as demonstrated in Fig. 2*D*, contribute to the uncertainty of the mean sarcomere length estimates.

Figure 5, *bottom*, shows the rate estimates of the mean sarcomere length (computed as 3-point finite difference of the corresponding sarcomere length sequences) for each of the three methods. Here, the plateau artifacts from spectral and ACF-based methods appear as spurious peaks in the sarcomere length rate evolution. In summary, Fig. 5, *A* and *B*, demonstrates the inherit problems in using spectral and ACF approaches and the reliability of our method for estimating the mean sarcomere length and its rate.

Finally, we note that the orientation of sarcomeres may change during the contraction of a cardiomyocyte. This orientation change can be determined using a sensitivity analysis of sarcomere length to ROI orientation (see Fig. 4) applied to each microscopy image of the cardiomyocyte, although not in real time due to extensive computational requirements. Figure 6, *top*, shows the evolution of an optimal ROI angle, or equivalently, the average orientation angle of sarcomeres during the contraction. Figure 6, *bottom*, shows the evolution of the estimated mean sarcomere length, accompanied with two sarcomere length estimates from correcting the ROI orientation with two methods: *1*) using the time-dependent optimal ROI angle and *2*) using fixed optimal ROI angle from the first microscopy image. Clearly, the mismatch of ROI orientation to the variable sarcomere orientation has only a small effect on the mean sarcomere length estimates when comparing with the case without orientation correction (ROI angle = 0°).

Invariance of the mean sarcomere length to the ROI selection in the case of a homogeneous contraction of cardiomyocytes. We have analyzed the sensitivity of the mean sarcomere length estimate to ROI size and location at different stages of cardiomyocyte contraction: at the resting stage $t = 0$ *s* (in Fig. 3 for largest considered ROI size the mean sarcomere length over a region between carbon fibers is SL = 1.789 ± 0.012, using the method of current work on all possible ROIs between carbon fibers), at the beginning of contraction $t \approx 0.32$ s (SL = 1.784 ± 0.010), at the most rapid stage of contraction $t \approx 0.34$ s (SL = 1.709 ± 0.007), at the shortest sarcomere length stage $t \approx 0.42$ s (SL = 1.640 ± 0.008), and at the relaxation stage $t \approx 0.48$ s (SL = 1.715 ± 0.009, all time points present in Fig. 5). For small ROI sizes that resolve the small heterogeneity of sarcomeres within the cardiomyocyte we have not observed that certain regions would contract more rapidly than others (results not shown). From these results we conclude that the contraction is uniform over a particular cardiomyocyte (at the

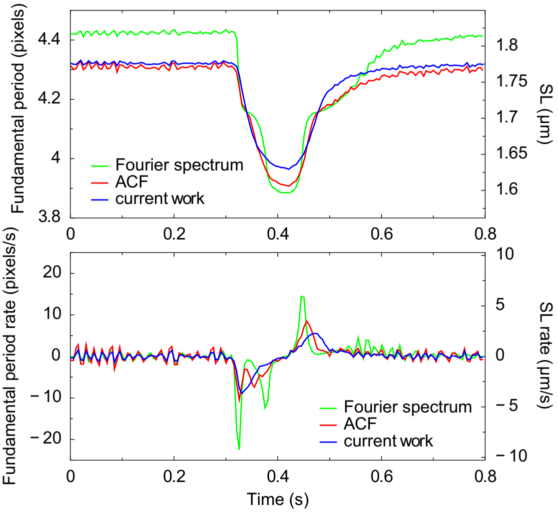

Fig. 5. Determination of sarcomere length in a contracting rat cardiomyocyte. *Top*: time evolution of the mean sarcomere length estimated by three methods. Microscopy images of a cardiomyocyte are recorded at rate 200 Hz and the same ROI, as in Fig. 2, is used. The methods based on Fourier spectrum and ACF analysis clearly demonstrate modulation defects: plateaus in the mean sarcomere length curve and spurious peaks in the mean sarcomere length rate curve (*bottom*). The mean sarcomere length estimate from the method of current work does not have these artifacts.

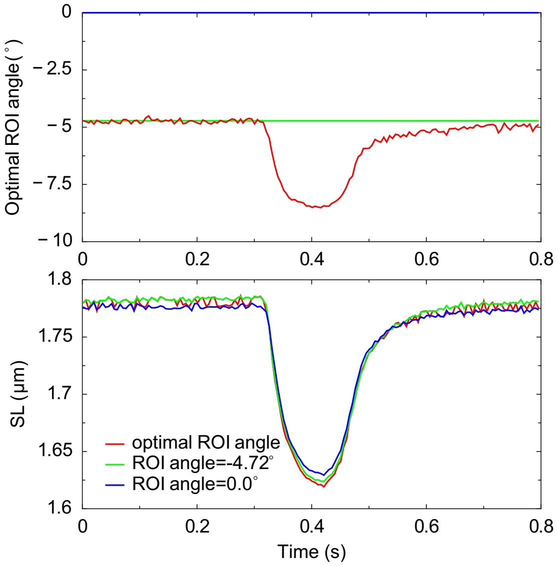

Fig. 6. Correction of ROI orientation in the determination of mean sarcomere length in a contracting rat cardiomyocyte. *Top*: orientation of ROI as a function of time. The optimal ROI orientation is defined as the average orientation of sarcomere striation pattern that is determined form the sarcomere length sensitivity analysis to ROI selection (see Fig. 4 and RESULTS). ROI angle −4.72° corresponds to the optimal ROI orientation of the first image where cardiomyocyte is at relaxed state. ROI angle 0° corresponds to initial ROI orientation selected visually by operator. *Bottom*: mean sarcomere length estimates computed from the three ROI orientation selections where one is time dependent. Notice that the mean sarcomere length estimate with no ROI orientation correction is rather close to the estimates that take into account the cardiomyocyte orientation variations during contraction.

acquisition rate of 200 Hz) and the mean sarcomere length estimate does not depend on the position of ROI even during the contraction. This conclusion is in agreement with the results from Gannier et al. (3). Note, however, our study is performed on cardiomyocyte images where nuclei are far from the focal plane, and therefore, no signs of significant sarcomere length variations were detected. Although in the proximity of nuclei, the variations of sarcomere length could be expected (19). Also note that the cardiomyocyte under study is almost unloaded; only the elasticity of fibers load the cardiomyocyte during contraction.

Example experiments. In the following we provide two examples of experiments on single cardiomyocytes that illustrate the response of sarcomere length estimates to changing preload conditions and to switching stimulation frequencies, both represented in Fig. 7. Increasing the preload level of a cardiomyocyte by two attached carbon fibers leads to an increase of contraction extent as seen on the time series of the mean sarcomere length. This is a manifestation of the Frank-Starling law at a single cardiomyocyte sarcomere level. Switching stimulation frequency also leads to changes in contraction extent but with a longer transition period characterizing the adoption of cardiomyocyte to new loading conditions.

DISCUSSION

In this work we developed a computationally efficient and practical method for estimating the mean sarcomere lengths of a single contracting cardiomyocyte. Input to the method is a microscopy image of a cardiomyocyte (or ROI image) that is assumed to contain sarcomere striation patterns. Uneven background due to possibly visible nuclei, external carbon fibers, or otherwise unfavorable optical conditions is filtered out in image preprocessing step by using the introduced detrend algorithm. The preprocessed image is compared with its own shifted copy to find the smallest nonzero shift at which the two images have the closest match. We define a similarity measure to quantify such a match. Since the optimal shift is a continuous parameter as opposed to the grid of microscopy image, we use piecewise linear approximation of the image to achieve the estimate of the mean sarcomere length at subpixel resolution. While conventional methods based on Fourier spectrum and ACF analysis could use a similar approach, our method takes into account the fact that microscopy images have finite extent, and as a result, the mean sarcomere length estimates are not artificially modulated by boundary conditions that are the main source of systematic errors in the mentioned conventional methods. We have performed the sensitivity analysis of the proposed method to uncertainties such as ROI size, location, and orientation that are all common when executing experimental protocols on contracting cardiomyocytes that are controlled, for instance, by attached carbon fibers.

Measurement of the mean sarcomere length is essential for many experimental protocols. For example, as a prerequisite of carrying out experiments that use cardiomyocytes, the quality of the cell must be assessed. The cell quality can be characterized by the size of diastolic sarcomere length as well as by the extent of cardiomyocyte contraction that is quantified via sarcomere length. Sarcomere length of a cardiomyocyte can be determined via microscope imaging and using specialized image processing technique, such as one developed in this study. Measurement of sarcomere length is crucial for experimental protocols that measure the mechanical properties of cardiomyocytes. For example, cardiomyocyte mechanical properties are studied by determining the force and length relationship of cardiomyocyte under a variety of mechanical conditions such as isometric and physiological conditions (16, 5) or by determining differences in the contractile properties of control and diseased animal models (15). In addition, cell stretching is used to study the mechanoelectrical feedback of cardiomyocyte where recording of sarcomere length is important (14, 6). Real-time measurement of sarcomere length has also been used for measuring muscle performance in vivo (13) to investigate neuromuscular disorders.

In the present study we developed a method for estimating the mean sarcomere length from microscopy images obtained with a high-speed camera capturing transmission light. The same method could be applied to fluorescence microscopy images where sarcomere locations are revealed with quantum dots (21) or using, for instance, two-photon excitation microscopy (1). Other approaches exists for estimating the mean sarcomere length of cardiomyocytes. For instance, the analysis of X-ray or laser-light diffraction patterns gives accurate sarcomere length estimates on both the muscle fiber level (12, 7) and cell level (9, 11). With the advances in CCD/CMOS

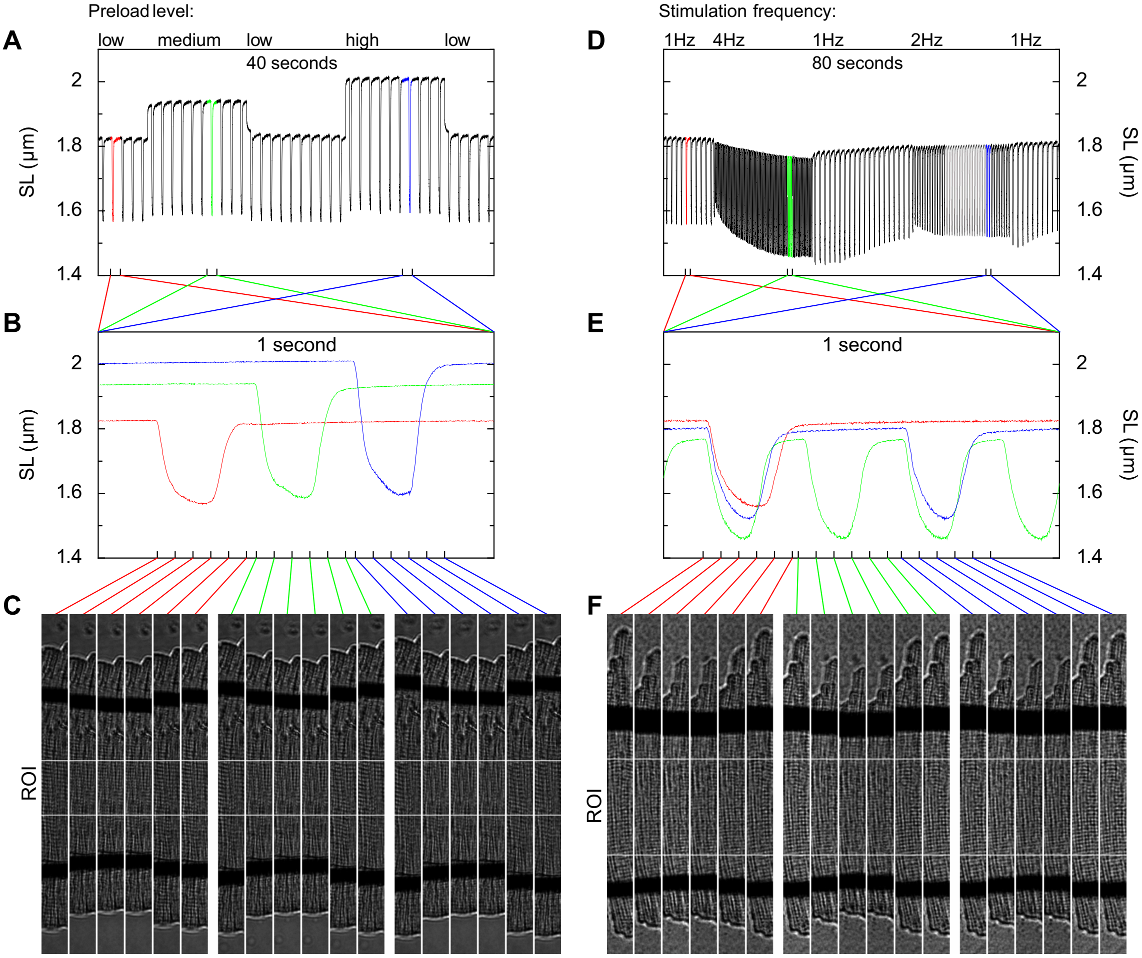

Fig. 7. Determination of sarcomere lengths in single rat cardiomyocyte experiments with different preload levels (*left*) and different stimulation frequencies (*right*). *A* and *D*: time series of sarcomere lengths over experiment periods 40 and 80 s, respectively. During the experiment periods the preload and stimulation conditions are varied. *B* and *E*: sarcomere lengths over a 1-s period as recorded during different loading conditions. *C* and *F*: transmission images of cardiomyocytes at time moments indicated with connecting lines between the *B* and *E* and *C* and *F*. The region between lines of white pixels indicates the ROI that is used for determining the mean sarcomere lengths for each captured image of cardiomyocytes.

technology and image processing techniques, the analysis of microscopy images from high-speed cameras provides alternative techniques to diffraction-based methods with potentially similar accuracy and performance properties, while at the same time being simple and cost-effective.

The mean sarcomere length is defined as the spatial fundamental period of repeating patterns of sarcomeres in a microscopy image of a cardiomyocyte. The technique developed in this study for estimating the mean sarcomere length uses a number of novel approaches. *1*) From the inherit reality of measuring signals with finite length, the underlying mathematical theory for the sarcomere length estimation technique considers functions on finite interval and proposes an unbiased measure of similarities for a pair of functions. We have shown that the ACF, which provides a popular measure of similarities due to its efficient evaluation via FFT, is biased: for otherwise uniformly changing sarcomere length, the sarcomere length estimate from ACF analysis is always modulated. In addition, because FFT-based methods impose periodic boundary conditions to otherwise finite signal sequences, the modulations of sarcomere length estimates are then amplified even more due to the mismatch between the period imposed by FFT to the overall signal and the fundamental period, such as sarcomere length, within the signal. Although practical tricks exist to reduce this modulation defect, in our approach, however, these artificial constraints are avoided. *2*) Our technique uses a semianalytical, seminumerical approach for evaluating the measures of similarities efficiently. With the use of a piecewise linear representation of otherwise discrete signals, the integrals in similarity measures are resolved analytically. As a result, the similarity measure is a piecewise cubic polynomial whose nodal values are a finite series of signal samples. From that, the mean sarcomere length is estimated analytically as the minimum point of one of the cubic polynomials in this piecewise polynomial representation of the similarity measure. Such an approach enabled us to implement a numerical algorithm for the mean sarcomere length estimation that has superior computational performance to FFT-based methods. *3*) We have introduced an image preprocessing detrend algorithm that extracts periodic variations from a microscopy image with possibly nonuniform background. This algorithm can be used in combination with ACF-based methods where preprocessing of images to a zero-average condition is also needed. As discussed below, the detrend algorithm improves the stability of sarcomere length estimates in experiments.

Our sarcomere length estimation algorithm is closely related to ACF-based algorithms for determining fundamental periods in images. In fact, if the image of sarcomeres would be perfectly periodic, then both methods would return exactly the same estimates. ACF-based algorithms can take advantage of both the detrend algorithm and the used approach to achieve estimates at subpixel resolution. However, when the image has limited size, as it is common in practice, the estimate from a ACF-based algorithm is biased due to the mismatch of image intensities at the boundaries: the maximum point of ACF, which determines the estimated value, is slightly shifted from the exact value. Depending on how the image of sarcomeres is cut off at boundaries, the estimate can be either smaller or larger than the exact value. The extent of this deviation will decrease when longer sarcomere sequences are included to the image, say, by increasing the length of ROI. In contrast, the method developed in this work is unbiased to the image boundary conditions.

To summarize, the accuracy of the developed method is limited only by the following practical restrictions: *1*) the subpixel accuracy of the mean sarcomere length estimate is limited by the finite image resolution, and *2*) apparent inhomogeneous distribution of sarcomeres, both in length and orientation, will increase the uncertainty of sarcomere length estimates and makes introduction of the notation of the mean sarcomere length unavoidable. In theory, our method determines the fundamental period exactly when the object field has a unique periodic component and finite size. Thus our method circumvents one of the practical limitations of conventional methods based on ACF or Fourier spectrum analysis. With the use of the conventional methods, the mean sarcomere length estimate will always be artificially modulated during the contraction of cardiomyocyte because of the finite size of microscopy images.

The technique developed in this study has been successfully tested on microscopy images of rat cardiomyocytes. The sarcomere length sensitivity analysis to ROI selection showed that the method is robust to a variety of experimental constraints such as uneven field of illumination (resolved by the detrend algorithm), existence of external objects (such as carbon fibers) in the field of view, and uncertainty of choosing the orientation of ROI with respect to variable orientation of sarcomeres (also during contraction). While the speed of sarcomere length estimation was more than enough for our experimental protocols (maximal line rate of our CCD camera is ~1 kHz while the rate of sarcomere length estimation with full 120 × 60 ROI in between carbon fibers was ~15 kHz), with recent and future advances in high-speed camera technologies and with larger ROI selections one could optimize the sarcomere length estimation rate even further, for example, by implementing the sarcomere length estimation algorithm in a field-programmable gate array chip. According to our tests, a more than doubled rate of sarcomere length determination is achieved when disabling the detrend algorithm. This, however, requires that images have an uniform background field and no external objects such as carbon fibers exist within the ROI. Another approach would be to use a parallelized implementation of the proposed algorithm.

To obtain meaningful sarcomere length estimates, selection of computational methods and ROI positions is of importance. In this study, we showed that ACF and Fourier spectrum analysis-based methods modulate the estimates of the sarcomere length considerably when the number of sarcomeres per ROI length is relatively small. The method provided by the current work eliminates this modulation defect. We have also showed that the misalignment of ROI orientation to sarcomere striation pattern will produce overestimates to the mean sarcomere length. The location of ROI within the cardiomyocyte image is also important. Depending on the used attachment techniques of cardiomyocyte ends and applied loading (17, 16, 5), ROI should be placed to location where sarcomere striation pattern is uniform and as far as possible from attachment points. When using the carbon fiber attachment technique, the distribution of sarcomeres is found to be fairly homogeneous between carbon fibers as well as between different sides of a cardiomyocyte (5). The size of ROI should be as large as possible to increase the amount of information on the periodic variations of sarcomere striation patterns but not larger than the local uniformity of the striation patterns would allow.

In summary, the developed algorithm for the mean sarcomere length estimation is proposed as a superior algorithm to popular ACF and spectral analysis-based sarcomere length estimation techniques. In fact, the developed algorithm can be used for determining the fundamental periods of any signals, and hence, the algorithm has much wider applications. The C and Python source code of developed methods are available in the IOCBio Google Code project (http://iocbio.googlecode.com/) under the Open Source Initiative BSD-2 License.

APPENDIX

Here, a mathematically rigor description of the algorithms is given.

Similarity Measures

To find the mean sarcomere length of a cardiomyocyte, we use image and its shifted copy. The mean sarcomere length is assumed to correspond to the shift that leads to the smallest difference, i.e., largest similarity, of the image and its shifted copy. In this section we define three possible functionals that measure similarity of a given function and its shifted counterpart. These functionals are used as objective functions to a minimization problem that solution corresponds to the fundamental period of the given function.

First, as a basic tool of the current work, we define a similarity measure between the function $f(x)$ and its shifted counterpart $f(x + y)$ as follows:

$$\mathrm{F}^{\mathrm{E}}[f](y) = \int [f(x + y) - f(x)]^2 dx, \qquad (1)$$

where the integration interval depends on the type of functions: for periodic functions the integration is carried out over an interval with the length of a period and for functions on a finite interval over a subinterval where $f(x + y)$ and $f(x)$ are defined simultaneously. Clearly, the measure F^{E} has a local minimum at the fundamental period and we can use it as objective function for finding the fundamental period estimate of a quasiperiodic function $f = f(x)$: $P^{\mathrm{E}}_{\mathrm{est}}[f] = \mathrm{argmin}_{y>0}\, \mathrm{F}^{\mathrm{E}}[f](y)$, where $P = \mathrm{argmin}_{y>0}\, F(y)$ means that P is a positive minimum point of a function $F(y)$.

Expansion of the integrand in *Eq. 1* yields

$$\mathrm{F}^{\mathrm{E}}[f](y) = \int f(x+y)^2 dx + \int f(x)^2 dx - 2\mathrm{ACF}[f](y), \quad (2)$$

where

$$\mathrm{ACF}[f](y) = \int f(x) f(x+y) dx \quad (3)$$

is the ACF of $f(x)$. For periodic functions, the first two terms in *Eq. 2* are shift variable y independent, and hence, all local minima of F^{E} coincide with the corresponding local maxima of the ACF. For functions on finite interval, however, the locations of these minima and maxima are different because all three terms in *Eq. 2* depend on the shift variable. Hence, functional ACF cannot be used as an unbiased measure of similarities for functions on finite interval, although it is unbiased measure for periodic functions. The functional F^{E}, however, is an unbiased measure for all considered types of functions.

To demonstrate how biased measures, such as ACF, influence the accuracy of estimated fundamental period when functions are defined on finite interval, we define an ACF-based functional

$$\mathrm{F}^{\mathrm{A}}[f](y) = -\int_0^{L-y} f(x) f(x+y) dx, \quad (4)$$

and the corresponding fundamental period estimate: $P^{\mathrm{A}}_{\mathrm{est}}[f] = \mathrm{argmin}_{y>0}$ FA[f](y). To demonstrate the same with the class of periodic functions, we define

$$\mathrm{F}^{\mathrm{A}}_{\mathrm{periodic}}[f](y) = -\int_0^{L-y} f(x) f(x+y) dx - \int_{L-y}^{L} f(x) f(x+y-L) dx. \quad (5)$$

Note that this functional is equivalent to the conventional ACF of periodic functions that can be efficiently computed using the convolution theorem and FFT algorithm.

Semianalytical, Seminumerical Evaluation of Similarity Measures

Given a signal as a sequence of signal values $\mathbf{f} = \{f_i\}_{i=0}^{N-1}$, we define a piecewise polynomial function, a so-called signal function, as follows:

$$f(x) = \sum_{i=0}^{N-2} [0 \le x - i < 1] S(x - i;\, \mathbf{f},\, i), \quad (6)$$

where S denotes a low order polynomial defined for the interval $[I, i + 1]$ such that $S(0; \mathbf{f}, i) = f_i$ with additional continuity conditions on the derivatives of $f(x)$ when possible; S can be a basic spline function, for instance. The square brackets in *Eq. 6* denote an indicator function: when the condition within the brackets is satisfied then the value of the indicator function is 1; otherwise 0. The signal function $f(x)$ is defined on the interval $[0, L]$ where the length of the interval, L, is related to the number of signal values N: $L = N - 1$. In this study, we use linear polynomials for S because then the minimum points of considered functionals may locate within integer intervals, which is a prerequisite for resolving fundamental periods at subpixel resolution. In addition, the minimum conditions are quadratic equations that are easy to solve.

To evaluate the integral in similarity measure *Eq. 1*, we use the following general result: if $G[f(x), f(x + y)]$ is a polynomial function of signal functions $f(x)$ and $f(x + y)$, then

$$\int_0^{L-y} G[f(x), f(x+y)] dx = \sum_{i=0}^{N-2-\lfloor y \rfloor} \int_0^{1-\{y\}} G\big[S(s;\ \mathbf{f},\ i), S(s + \{y\};\ \mathbf{f},\ i + \lfloor y \rfloor)\big] ds + \sum_{i=0}^{N-3-\lfloor y \rfloor} \int_{1-\{y\}}^{1} G\big[S(s;\ \mathbf{f},\ i), S(s + \{y\} - 1;\ \mathbf{f},\ i + \lfloor y \rfloor + 1)\big] ds, \quad (7)$$

where $\lfloor y \rfloor$ and $\{y\}$ denote integer floor and remainder of y, respectively, such that $y = \lfloor y \rfloor + \{y\}$. When evaluating the integrals in *Eq. 7* analytically, the result will be a polynomial in $\{y\}$with coefficients expressed as series depending on $\lfloor y \rfloor$. For example, for linear polynomials, $S(s; \mathbf{f}, i) = (1 - s)f_i + sf_{i+1}$, the integral in *Eq. 1* can be evaluated using

$$\mathrm{F}^{\mathrm{E}}[f](y) = e_0(\lfloor y \rfloor)/3 + e_1(\lfloor y \rfloor)\{y\} + e_2(\lfloor y \rfloor)\{y\}^2 + e_3(\lfloor y \rfloor)/3\{y\}^3, \quad (8)$$

where

$$\begin{aligned} e_0(j) = {} & f_{N-2}^2 + f_{N-1}(f_{N-1} + f_{N-2}) + f_{N-j-1}(f_{N-j-1} - f_{N-2} - 2f_{N-1}) + f_{N-j-2}(f_{N-j-1} + f_{N-j-2} - f_{N-1} - 2f_{N-2}) \\ & + \sum_{i=0}^{N-3-j} f_i(f_i - f_{i+j+1} - 2f_{i+j}) + f_{i+1}(f_{i+1} + f_i - f_{i+j} - 2f_{i+j+1}) + f_{i+j}(f_{i+j+1} + f_{i+j}) + f_{i+j+1}^2, \\ e_1(j) = {} & +f_{N-2}(f_{N-j-2} - f_{N-2}) - f_{N-j-2}f_{N-1} + f_{N-j-1}(f_{N-2} + f_{N-1} - f_{N-j-1}) \\ & + \sum_{i=0}^{N-3-j} f_{i+j}(f_{i+1} + f_i - f_{i+j}) + f_{i+j+1}(f_{i+j+1} - f_{i+1} - f_i), \\ e_2(j) = {} & +f_{N-2}(f_{N-2} - f_{N-1}) + f_{N-j-2}f_{N-1} + f_{N-j-1}(f_{N-j-1} - f_{N-j-2} - f_{N-2}) \\ & + \sum_{i=0}^{N-3-j} f_{i+j}^2 + (-f_{i+j} - f_{i+j+2})f_{i+1} + f_{i+j+1}(2f_{i+1} + f_{i+j+2} - f_{i+j} - f_{i+j+1}), \\ e_3(j) = {} & -f_{N-1}^2 + f_{N-2}(2f_{N-1} - f_{N-2}) + f_{N-j-2}(f_{N-1} - f_{N-j-2} - f_{N-2}) + f_{N-j-1}(2f_{N-j-2} + f_{N-2} - f_{N-j-1} - f_{N-1}) \\ & + \sum_{i=0}^{N-3-j} f_{i+j+2}(f_{i+1} + f_{i+j+2} - f_i) + f_{i+j}(f_{i+1} - f_i - f_{i+j}) + 2f_{i+j+1}(f_i + f_{i+j} - f_{i+1} - f_{i+j+2}). \end{aligned}$$

Similar expressions can be derived for $\mathrm{F}^{\mathrm{A}}[f]$ and $\mathrm{F}^{\mathrm{A}}_{\mathrm{periodic}}[f]$. The corresponding computational routines are provided in *Supporting Software*.

Determination of the Fundamental Period

In this work, the fundamental period of a signal is estimated as the first positive minimum point of a similarity measure (F^{E}, F^{A}, and $\mathrm{F}^{\mathrm{A}}_{\mathrm{periodic}}$). By introducing a piecewise linear signal function, the similarity measure is a piecewise cubic polynomial and its minimum point is found as the second positive zero point of its derivative (the first one corresponds to local maxima). In general, the computational complexity of finding the fundamental period of a signal is $O[(N - \lfloor P \rfloor)\lfloor P \rfloor]$, where N and P are the length and the fundamental period of the signal, respectively. Compare this to the computational complexity $O(N \log N)$ of the FFT algorithm.

In the case of a microscopy image that is represented as a two-dimensional array of signal sequences, we define an average similarity measure computed as the average of similarity measures of all lines in the image ROI. The fundamental period estimate of the image array is defined as the first positive minimum point of the average similarity measure. Alternatively, one could compute the fundamental period estimate for each line of the image ROI and then by averaging over all lines find the mean fundamental period estimate. In general, the estimates of both approaches will be slightly different. We prefer the first one because it turns out to be more robust to images where sarcomere related intensity variations are weak.

Detrending a Signal

The detrend algorithm consists of four steps. In the first step, random noise in a signal sequence is suppressed using convolution with a uniform kernel that has a half-width of ~1/10 of the fundamental period. In the second step, all local extrema are found from the obtained noise-suppressed sequence. The graph of these local extrema are connected with line segments constituting a linear spline that we denote as an extreme spline. In the third step, the middle points of the line segments of the extreme spline are connected with lines. The result constitutes another linear spline that we denote as a trend spline. Finally, the oscillatory part of the signal sequence (including random noise) is obtained by subtracting the trend spline from the original signal sequence. This method of extracting the oscillatory part of a sequence is implemented in a computer program using a single loop and thus has computational complexity $O(N)$. The corresponding routine is available in *Supporting Software*. For microscopy images, this procedure is applied for each line of image ROI (see Fig. 2, *B–G*, for illustration).

Details of Other Conventional Methods

For comparison of the results of current work, we use two other conventional methods for estimating the fundamental period of a signal.

The first method, labeled as the "Fourier spectrum" method, is based on calculating the power spectrum, here defined as the square of modulo of Fourier spectrum, of a signal. The maximum point of the power spectrum is related to the fundamental spatial frequency of the signal, which, in turn, is inversely proportional to the fundamental period of the signal. For discrete signals, the power spectrum is discrete as well meaning that the fundamental period can be estimated at the pixel size resolution. To obtain fundamental period estimates at subpixel resolution, we use piecewise quadratic interpolation of the discrete power spectrum.

The second method, labeled as the "ACF" method, is based on calculating the ACF, here defined as inverse Fourier transform of the power spectrum, of a signal. The first positive maximum point of the ACF is related to the fundamental period of the signal. Similarly to the Fourier spectrum method, the fundamental period estimates are obtained at subpixel resolution by using piecewise quadratic interpolation of the discrete ACF.

In both methods, we use FFT for calculating the discrete Fourier spectra of signals. In comparison analysis of different methods we always use detrended signals as input signals to *1*) minimize boundary artifacts and *2*) ensure equal conditions for all considered methods. When applied to images, we use the mean power spectrum calculated as the average of power spectra over all image lines. The corresponding computational routines are available in Supporting Software.

ACKNOWLEDGMENTS

We thank Mervi Sepp, Natalja Jepihhina, and Rikke Birkedal for providing cardiomyocytes and Merle Mandel for technical assistance (all from Laboratory of Systems Biology, Institute of Cybernetics, Tallinn University of Technology, Estonia).

GRANTS

This work was supported by the Wellcome Trust Fellowship No. WT081755 and Estonian Science Foundation Grant No. 7344 and 8041 (PhD stipend to M. Kalda).

DISCLOSURES

No conflicts of interest, financial or otherwise, are declared by the author(s).

AUTHOR CONTRIBUTIONS

Author contributions: P.P., M.K., and M.V. conception and design of research; P.P. analyzed data; P.P., M.K., and M.V. interpreted results of experiments; P.P. prepared figures; P.P. drafted manuscript; P.P., M.K., and M.V. edited and revised manuscript; P.P., M.K., and M.V. approved final version of manuscript; M.K. performed experiments.

REFERENCES

1. **Bub G, Camelliti P, Bollensdorff C, Stuckey DJ, Picton G, Burton RAB, Clarke K, Kohl P.** Measurement and analysis of sarcomere length in rat cardiomyocytes in situ and in vitro. *Am J Physiol Heart Circ Physiol* 298: H1616–H1625, 2010.
2. **Frigo M, Johnson SG.** The design and implementation of FFTW3. *Proc IEEE Inst Electr Electron Eng* 93: 216–231, 2005.
3. **Gannier F, Bernengo JC, Jacquemond V, Garnier D.** Measurements of sarcomere dynamics simultaneously with auxotonic force in isolated cardiac cells. *IEEE Trans Biomed Eng* 40: 1226–1232, 1993.
4. **Harris FJ.** On the use of windows for harmonic analysis with the discrete Fourier transform. *Proc IEEE Inst Electr Electron Eng* 66: 51–83, 1978.
5. **Iribe G, Helmes M, Kohl P.** Force-length relations in isolated intact cardiomyocytes subjected to dynamic changes in mechanical load. *Am J Physiol Heart Circ Physiol* 292: H1487–H1497, 2007.
6. **Iribe G, Kohl P.** Axial stretch enhances sarcoplasmic reticulum Ca^{2+} leak and cellular Ca^{2+} reuptake in guinea pig ventricular myocytes: experiments and models. *Prog Biophys Mol Biol* 97: 298–311, 2008.
7. **Iwazumi T, Pollack G.** On-line measurement of sarcomere length from diffraction patterns in muscle. *IEEE Trans Biomed Eng* BME-26: 86–93, 1979.
8. **Jepihhina N, Beraud N, Sepp M, Birkedal R, VendelinM.** Permeabilized rat cardiomyocyte response demonstrates intracellular origin of diffusion obstacles. *Biophys J* 101: 2112–2121, 2011.
9. **Krueger J, Forletti D, Wittenberg B.** Uniform sarcomere shortening behavior in isolated cardiac muscle cells. *J Gen Physiol* 76: 587–607, 1980.
10. **Krueger JW, Pollack GH.** Myocardial sarcomere dynamics during isometric contraction. *J Physiol* 251: 627–643, 1975.
11. **Lieber R, Yeh Y, Baskin R.** Sarcomere length determination using laser diffraction. Effect of beam and fiber diameter. *Biophys J* 45: 1007–1016, 1984.
12. **Linari M, Piazzesi G, Dobbie I, Koubassova N, Reconditi M, Narayanan T, Diat O, Irving M, Lombardi V.** Interference fine structure and sarcomere length dependence of the axial x-ray pattern from active single muscle fibers. *Proc Natl Acad Sci USA* 97: 7226–7231, 2000.
13. **Llewellyn M, Barretto RJ, Delp S, Schnitzer M.** Minimally invasive high-speed imaging of sarcomere contractile dynamics in mice and humans. *Nature* 454: 784–788, 2008.
14. **Nishimura S, Seo K, Nagasaki M, Hosoya Y, Yamashita H, Fujita H, Nagai R, Sugiura S.** Responses of single-ventricular myocytes to dynamic axial stretching. *Prog Biophys Mol Biol* 97: 282–297, 2008.
15. **Nishimura S, Yamashita H, Katoh M, Yamada K, Sunagawa K, Saeki Y, Ohnuki Y, Nagai R, Sugiura S.** Contractile dysfunction of cardiomyopathic hamster myocytes is pronounced under high load conditions. *J Mol Cell Cardiol* 39: 231–239, 2005.
16. **Nishimura S, Yasuda S, Katoh M, Yamada K, Yamashita H, Saeki Y, Sunagawa K, Nagai R, Hisada T, Sugiura S.** Single cell mechanics of rat cardiomyocytes under isometric, unloaded, and physiologically loaded conditions. *Am J Physiol Heart Circ Physiol* 287: H196–H202, 2004.
17. **Palmer RE, Brady AJ, Roos KP.** Mechanical measurements from isolated cardiac myocytes using a pipette attachment system. *Am J Physiol Cell Physiol* 270: C697–C704, 1996.
18. **Peterson P.** F2PY: a tool for connecting Fortran and Python programs. *Int J Comput Sci Eng* 4: 296–305, 2009.
19. **Roos K.** Sarcomere length uniformity determined from three-dimensional reconstructions of resting isolated heart cell striation patterns. *Biophys J* 52: 317–327, 1987.
20. **Sepp M, Vendelin M, Vija H, Birkedal R.** ADP compartmentation analysis reveals coupling between pyruvate kinase and ATPases in heart muscle. *Biophys J* 98: 2785–2793, 2010.
21. **Serizawa T, Terui T, Kagemoto T, Mizuno A, Shimozawa T, Kobirumaki F, Ishiwata S, Kurihara S, Fukuda N.** Real-time measurement of the length of a single sarcomere in rat ventricular myocytes: a novel analysis with quantum dots. *Am J Physiol Cell Physiol* 301: C1116–C1127, 2011.
22. **Sugiura S, Nishimura S, Yasuda S, Hosoya Y, Katoh K.** Carbon fiber technique for the investigation of single-cell mechanics in intact cardiac myocytes. *Nat Protoc* 1: 1453–1457, 2006.
23. **Yasuda S, Sugiura S, Kobayakawa N, Fujita H, Yamashita H, Katoh K, Saeki Y, Kaneko H, Suda Y, Nagai R, Sugi H.** A novel method to study contraction characteristics of a single cardiac myocyte using carbon fibers. *Am J Physiol Heart Circ Physiol* 281: H1442–H1446, 2001.

DISSERTATIONS DEFENDED AT TALLINN UNIVERSITY OF TECHNOLOGY ON *NATURAL AND EXACT SCIENCES*

1. **Olav Kongas**. Nonlinear Dynamics in Modeling Cardiac Arrhytmias. 1998.
2. **Kalju Vanatalu**. Optimization of Processes of Microbial Biosynthesis of Isotopically Labeled Biomolecules and Their Complexes. 1999.
3. **Ahto Buldas**. An Algebraic Approach to the Structure of Graphs. 1999.
4. **Monika Drews**. A Metabolic Study of Insect Cells in Batch and Continuous Culture: Application of Chemostat and Turbidostat to the Production of Recombinant Proteins. 1999.
5. **Eola Valdre**. Endothelial-Specific Regulation of Vessel Formation: Role of Receptor Tyrosine Kinases. 2000.
6. **Kalju Lott**. Doping and Defect Thermodynamic Equilibrium in ZnS. 2000.
7. **Reet Koljak**. Novel Fatty Acid Dioxygenases from the Corals *Plexaura homomalla* and *Gersemia fruticosa.* 2001.
8. **Anne Paju**. Asymmetric oxidation of Prochiral and Racemic Ketones by Using Sharpless Catalyst. 2001.
9. **Marko Vendelin**. Cardiac Mechanoenergetics *in silico*. 2001.
10. **Pearu Peterson**. Multi-Soliton Interactions and the Inverse Problem of Wave Crest. 2001.
11. **Anne Menert**. Microcalorimetry of Anaerobic Digestion. 2001.
12. **Toomas Tiivel**. The Role of the Mitochondrial Outer Membrane in *in vivo* Regulation of Respiration in Normal Heart and Skeletal Muscle Cell. 2002.
13. **Olle Hints**. Ordovician Scolecodonts of Estonia and Neighbouring Areas: Taxonomy, Distribution, Palaeoecology, and Application. 2002.
14. **Jaak Nõlvak**. Chitinozoan Biostratigrapy in the Ordovician of Baltoscandia. 2002.
15. **Liivi Kluge**. On Algebraic Structure of Pre-Operad. 2002.
16. **Jaanus Lass**. Biosignal Interpretation: Study of Cardiac Arrhytmias and Electromagnetic Field Effects on Human Nervous System. 2002.
17. **Janek Peterson**. Synthesis, Structural Characterization and Modification of PAMAM Dendrimers. 2002.
18. **Merike Vaher**. Room Temperature Ionic Liquids as Background Electrolyte Additives in Capillary Electrophoresis. 2002.
19. **Valdek Mikli**. Electron Microscopy and Image Analysis Study of Powdered Hardmetal Materials and Optoelectronic Thin Films. 2003.
20. **Mart Viljus**. The Microstructure and Properties of Fine-Grained Cermets. 2003.
21. **Signe Kask**. Identification and Characterization of Dairy-Related *Lactobacillus.* 2003
22. **Tiiu-Mai Laht**. Influence of Microstructure of the Curd on Enzymatic and Microbiological Processes in Swiss-Type Cheese. 2003.
23. **Anne Kuusksalu**. 2–5A Synthetase in the Marine Sponge *Geodia cydonium*. 2003.
24. **Sergei Bereznev**. Solar Cells Based on Polycristalline Copper-Indium Chalcogenides and Conductive Polymers. 2003.

25. **Kadri Kriis**. Asymmetric Synthesis of C_2-Symmetric Bimorpholines and Their Application as Chiral Ligands in the Transfer Hydrogenation of Aromatic Ketones. 2004.
26. **Jekaterina Reut**. Polypyrrole Coatings on Conducting and Insulating Substracts. 2004.
27. **Sven Nõmm**. Realization and Identification of Discrete-Time Nonlinear Systems. 2004.
28. **Olga Kijatkina**. Deposition of Copper Indium Disulphide Films by Chemical Spray Pyrolysis. 2004.
29. **Gert Tamberg**. On Sampling Operators Defined by Rogosinski, Hann and Blackman Windows. 2004.
30. **Monika Übner**. Interaction of Humic Substances with Metal Cations. 2004.
31. **Kaarel Adamberg**. Growth Characteristics of Non-Starter Lactic Acid Bacteria from Cheese. 2004.
32. **Imre Vallikivi**. Lipase-Catalysed Reactions of Prostaglandins. 2004.
33. **Merike Peld**. Substituted Apatites as Sorbents for Heavy Metals. 2005.
34. **Vitali Syritski**. Study of Synthesis and Redox Switching of Polypyrrole and Poly(3,4-ethylenedioxythiophene) by Using *in-situ* Techniques. 2004.
35. **Lee Põllumaa**. Evaluation of Ecotoxicological Effects Related to Oil Shale Industry. 2004.
36. **Riina Aav**. Synthesis of 9,11-Secosterols Intermediates. 2005.
37. **Andres Braunbrück**. Wave Interaction in Weakly Inhomogeneous Materials. 2005.
38. **Robert Kitt**. Generalised Scale-Invariance in Financial Time Series. 2005.
39. **Juss Pavelson**. Mesoscale Physical Processes and the Related Impact on the Summer Nutrient Fields and Phytoplankton Blooms in the Western Gulf of Finland. 2005.
40. **Olari Ilison**. Solitons and Solitary Waves in Media with Higher Order Dispersive and Nonlinear Effects. 2005.
41. **Maksim Säkki**. Intermittency and Long-Range Structurization of Heart Rate. 2005.
42. **Enli Kiipli**. Modelling Seawater Chemistry of the East Baltic Basin in the Late Ordovician–Early Silurian. 2005.
43. **Igor Golovtsov**. Modification of Conductive Properties and Processability of Polyparaphenylene, Polypyrrole and polyaniline. 2005.
44. **Katrin Laos**. Interaction Between Furcellaran and the Globular Proteins (Bovine Serum Albumin β-Lactoglobulin). 2005.
45. **Arvo Mere**. Structural and Electrical Properties of Spray Deposited Copper Indium Disulphide Films for Solar Cells. 2006.
46. **Sille Ehala**. Development and Application of Various On- and Off-Line Analytical Methods for the Analysis of Bioactive Compounds. 2006.
47. **Maria Kulp**. Capillary Electrophoretic Monitoring of Biochemical Reaction Kinetics. 2006.
48. **Anu Aaspõllu.** Proteinases from *Vipera lebetina* Snake Venom Affecting Hemostasis. 2006.

49. **Lyudmila Chekulayeva**. Photosensitized Inactivation of Tumor Cells by Porphyrins and Chlorins. 2006.
50. **Merle Uudsemaa**. Quantum-Chemical Modeling of Solvated First Row Transition Metal Ions. 2006.
51. **Tagli Pitsi**. Nutrition Situation of Pre-School Children in Estonia from 1995 to 2004. 2006.
52. **Angela Ivask**. Luminescent Recombinant Sensor Bacteria for the Analysis of Bioavailable Heavy Metals. 2006.
53. **Tiina Lõugas**. Study on Physico-Chemical Properties and Some Bioactive Compounds of Sea Buckthorn (*Hippophae rhamnoides* L.). 2006.
54. **Kaja Kasemets**. Effect of Changing Environmental Conditions on the Fermentative Growth of *Saccharomyces cerevisae* S288C: Auxo-accelerostat Study. 2006.
55. **Ildar Nisamedtinov**. Application of ^{13}C and Fluorescence Labeling in Metabolic Studies of *Saccharomyces* spp. 2006.
56. **Alar Leibak**. On Additive Generalisation of Voronoï's Theory of Perfect Forms over Algebraic Number Fields. 2006.
57. **Andri Jagomägi**. Photoluminescence of Chalcopyrite Tellurides. 2006.
58. **Tõnu Martma**. Application of Carbon Isotopes to the Study of the Ordovician and Silurian of the Baltic. 2006.
59. **Marit Kauk**. Chemical Composition of $CuInSe_2$ Monograin Powders for Solar Cell Application. 2006.
60. **Julia Kois**. Electrochemical Deposition of $CuInSe_2$ Thin Films for Photovoltaic Applications. 2006.
61. **Ilona Oja Açik**. Sol-Gel Deposition of Titanium Dioxide Films. 2007.
62. **Tiia Anmann**. Integrated and Organized Cellular Bioenergetic Systems in Heart and Brain. 2007.
63. **Katrin Trummal**. Purification, Characterization and Specificity Studies of Metalloproteinases from *Vipera lebetina* Snake Venom. 2007.
64. **Gennadi Lessin**. Biochemical Definition of Coastal Zone Using Numerical Modeling and Measurement Data. 2007.
65. **Enno Pais**. Inverse problems to determine non-homogeneous degenerate memory kernels in heat flow. 2007.
66. **Maria Borissova**. Capillary Electrophoresis on Alkylimidazolium Salts. 2007.
67. **Karin Valmsen**. Prostaglandin Synthesis in the Coral *Plexaura homomalla*: Control of Prostaglandin Stereochemistry at Carbon 15 by Cyclooxygenases. 2007.
68. **Kristjan Piirimäe**. Long-Term Changes of Nutrient Fluxes in the Drainage Basin of the Gulf of Finland – Application of the PolFlow Model. 2007.
69. **Tatjana Dedova**. Chemical Spray Pyrolysis Deposition of Zinc Sulfide Thin Films and Zinc Oxide Nanostructured Layers. 2007.
70. **Katrin Tomson**. Production of Labelled Recombinant Proteins in Fed-Batch Systems in *Escherichia coli*. 2007.
71. **Cecilia Sarmiento**. Suppressors of RNA Silencing in Plants. 2008.
72. **Vilja Mardla**. Inhibition of Platelet Aggregation with Combination of Antiplatelet Agents. 2008.

73. **Maie Bachmann**. Effect of Modulated Microwave Radiation on Human Resting Electroencephalographic Signal. 2008.
74. **Dan Hüvonen**. Terahertz Spectroscopy of Low-Dimensional Spin Systems. 2008.
75. **Ly Villo**. Stereoselective Chemoenzymatic Synthesis of Deoxy Sugar Esters Involving *Candida antarctica* Lipase B. 2008.
76. **Johan Anton**. Technology of Integrated Photoelasticity for Residual Stress Measurement in Glass Articles of Axisymmetric Shape. 2008.
77. **Olga Volobujeva**. SEM Study of Selenization of Different Thin Metallic Films. 2008.
78. **Artur Jõgi**. Synthesis of 4'-Substituted 2,3'-dideoxynucleoside Analogues. 2008.
79. **Mario Kadastik**. Doubly Charged Higgs Boson Decays and Implications on Neutrino Physics. 2008.
80. **Fernando Pérez-Caballero**. Carbon Aerogels from 5-Methylresorcinol-Formaldehyde Gels. 2008.
81. **Sirje Vaask**. The Comparability, Reproducibility and Validity of Estonian Food Consumption Surveys. 2008.
82. **Anna Menaker**. Electrosynthesized Conducting Polymers, Polypyrrole and Poly(3,4-ethylenedioxythiophene), for Molecular Imprinting. 2009.
83. **Lauri Ilison**. Solitons and Solitary Waves in Hierarchical Korteweg-de Vries Type Systems. 2009.
84. **Kaia Ernits**. Study of In_2S_3 and ZnS Thin Films Deposited by Ultrasonic Spray Pyrolysis and Chemical Deposition. 2009.
85. **Veljo Sinivee**. Portable Spectrometer for Ionizing Radiation "Gammamapper". 2009.
86. **Jüri Virkepu**. On Lagrange Formalism for Lie Theory and Operadic Harmonic Oscillator in Low Dimensions. 2009.
87. **Marko Piirsoo**. Deciphering Molecular Basis of Schwann Cell Development. 2009.
88. **Kati Helmja**. Determination of Phenolic Compounds and Their Antioxidative Capability in Plant Extracts. 2010.
89. **Merike Sõmera**. Sobemoviruses: Genomic Organization, Potential for Recombination and Necessity of P1 in Systemic Infection. 2010.
90. **Kristjan Laes**. Preparation and Impedance Spectroscopy of Hybrid Structures Based on $CuIn_3Se_5$ Photoabsorber. 2010.
91. **Kristin Lippur**. Asymmetric Synthesis of 2,2'-Bimorpholine and its 5,5'-Substituted Derivatives. 2010.
92. **Merike Luman**. Dialysis Dose and Nutrition Assessment by an Optical Method. 2010.
93. **Mihhail Berezovski**. Numerical Simulation of Wave Propagation in Heterogeneous and Microstructured Materials. 2010.
94. **Tamara Aid-Pavlidis**. Structure and Regulation of BDNF Gene. 2010.
95. **Olga Bragina**. The Role of Sonic Hedgehog Pathway in Neuro- and Tumorigenesis. 2010.

96. **Merle Randrüüt**. Wave Propagation in Microstructured Solids: Solitary and Periodic Waves. 2010.
97. **Marju Laars**. Asymmetric Organocatalytic Michael and Aldol Reactions Mediated by Cyclic Amines. 2010.
98. **Maarja Grossberg**. Optical Properties of Multinary Semiconductor Compounds for Photovoltaic Applications. 2010.
99. **Alla Maloverjan**. Vertebrate Homologues of Drosophila Fused Kinase and Their Role in Sonic Hedgehog Signalling Pathway. 2010.
100. **Priit Pruunsild**. Neuronal Activity-Dependent Transcription Factors and Regulation of Human *BDNF* Gene. 2010.
101. **Tatjana Knjazeva**. New Approaches in Capillary Electrophoresis for Separation and Study of Proteins. 2011.
102. **Atanas Katerski**. Chemical Composition of Sprayed Copper Indium Disulfide Films for Nanostructured Solar Cells. 2011.
103. **Kristi Timmo.** Formation of Properties of $CuInSe_2$ and $Cu_2ZnSn(S,Se)_4$ Monograin Powders Synthesized in Molten KI. 2011.
104. **Kert Tamm**. Wave Propagation and Interaction in Mindlin-Type Microstructured Solids: Numerical Simulation. 2011.
105. **Adrian Popp**. Ordovician Proetid Trilobites in Baltoscandia and Germany. 2011.
106. **Ove Pärn**. Sea Ice Deformation Events in the Gulf of Finland and This Impact on Shipping. 2011.
107. **Germo Väli**. Numerical Experiments on Matter Transport in the Baltic Sea. 2011.
108. **Andrus Seiman**. Point-of-Care Analyser Based on Capillary Electrophoresis. 2011.
109. **Olga Katargina**. Tick-Borne Pathogens Circulating in Estonia (Tick-Borne Encephalitis Virus, *Anaplasma phagocytophilum*, *Babesia* Species): Their Prevalence and Genetic Characterization. 2011.
110. **Ingrid Sumeri**. The Study of Probiotic Bacteria in Human Gastrointestinal Tract Simulator. 2011.
111. **Kairit Zovo**. Functional Characterization of Cellular Copper Proteome. 2011.
112. **Natalja Makarytsheva**. Analysis of Organic Species in Sediments and Soil by High Performance Separation Methods. 2011.
113. **Monika Mortimer**. Evaluation of the Biological Effects of Engineered Nanoparticles on Unicellular Pro- and Eukaryotic Organisms. 2011.
114. **Kersti Tepp**. Molecular System Bioenergetics of Cardiac Cells: Quantitative Analysis of Structure-Function Relationship. 2011.
115. **Anna-Liisa Peikolainen**. Organic Aerogels Based on 5-Methylresorcinol. 2011.
116. **Leeli Amon**. Palaeoecological Reconstruction of Late-Glacial Vegetation Dynamics in Eastern Baltic Area: A View Based on Plant Macrofossil Analysis. 2011.
117. **Tanel Peets**. Dispersion Analysis of Wave Motion in Microstructured Solids. 2011.

118. **Liina Kaupmees**. Selenization of Molybdenum as Contact Material in Solar Cells. 2011.
119. **Allan Olspert**. Properties of VPg and Coat Protein of Sobemoviruses. 2011.
120. **Kadri Koppel**. Food Category Appraisal Using Sensory Methods. 2011.
121. **Jelena Gorbatšova**. Development of Methods for CE Analysis of Plant Phenolics and Vitamins. 2011.
122. **Karin Viipsi**. Impact of EDTA and Humic Substances on the Removal of Cd and Zn from Aqueous Solutions by Apatite. 2012.
123. **David Schryer**. Metabolic Flux Analysis of Compartmentalized Systems Using Dynamic Isotopologue Modeling. 2012.
124. **Ardo Illaste**. Analysis of Molecular Movements in Cardiac Myocytes. 2012.
125. **Indrek Reile**. 3-Alkylcyclopentane-1,2-Diones in Asymmetric Oxidation and Alkylation Reactions. 2012.
126. **Tatjana Tamberg**. Some Classes of Finite 2-Groups and Their Endomorphism Semigroups. 2012.
127. **Taavi Liblik**. Variability of Thermohaline Structure in the Gulf of Finland in Summer. 2012.
128. **Priidik Lagemaa**. Operational Forecasting in Estonian Marine Waters. 2012.
129. **Andrei Errapart**. Photoelastic Tomography in Linear and Non-linear Approximation. 2012.
130. **Külliki Krabbi**. Biochemical Diagnosis of Classical Galactosemia and Mucopolysaccharidoses in Estonia. 2012.
131. **Kristel Kaseleht**. Identification of Aroma Compounds in Food using SPME-GC/MS and GC-Olfactometry. 2012.
132. **Kristel Kodar**. Immunoglobulin G Glycosylation Profiling in Patients with Gastric Cancer. 2012.
133. **Kai Rosin**. Solar Radiation and Wind as Agents of the Formation of the Radiation Regime in Water Bodies. 2012.
134. **Ann Tiiman**. Interactions of Alzheimer's Amyloid-Beta Peptides with Zn(II) and Cu(II) Ions. 2012.
135. **Olga Gavrilova**. Application and Elaboration of Accounting Approaches for Sustainable Development. 2012.
136. **Olesja Bondarenko**. Development of Bacterial Biosensors and Human Stem Cell-Based *In Vitro* Assays for the Toxicological Profiling of Synthetic Nanoparticles. 2012.
137. **Katri Muska**. Study of Composition and Thermal Treatments of Quaternary Compounds for Monograin Layer Solar Cells. 2012.
138. **Ranno Nahku**. Validation of Critical Factors for the Quantitative Characterization of Bacterial Physiology in Accelerostat Cultures. 2012.
139. **Petri-Jaan Lahtvee**. Quantitative Omics-level Analysis of Growth Rate Dependent Energy Metabolism in *Lactococcus lactis*. 2012.
140. **Kerti Orumets**. Molecular Mechanisms Controlling Intracellular Glutathione Levels in Baker's Yeast *Saccharomyces cerevisiae* and its Random Mutagenized Glutathione Over-Accumulating Isolate. 2012.
141. **Loreida Timberg**. Spice-Cured Sprats Ripening, Sensory Parameters Development, and Quality Indicators. 2012.

142. **Anna Mihhalevski**. Rye Sourdough Fermentation and Bread Stability. 2012.

143. **Liisa Arike**. Quantitative Proteomics of *Escherichia coli*: From Relative to Absolute Scale. 2012.

144. **Kairi Otto**. Deposition of In_2S_3 Thin Films by Chemical Spray Pyrolysis. 2012.

145. **Mari Sepp**. Functions of the Basic Helix-Loop-Helix Transcription Factor TCF4 in Health and Disease. 2012.

146. **Anna Suhhova**. Detection of the Effect of Weak Stressors on Human Resting Electroencephalographic Signal. 2012.

147. **Aram Kazarjan**. Development and Production of Extruded Food and Feed Products Containing Probiotic Microorganisms. 2012.

148. **Rivo Uiboupin**. Application of Remote Sensing Methods for the Investigation of Spatio-Temporal Variability of Sea Surface Temperature and Chlorophyll Fields in the Gulf of Finland. 2013.

149. **Tiina Kriščiunaite**. A Study of Milk Coagulability. 2013.

150. **Tuuli Levandi**. Comparative Study of Cereal Varieties by Analytical Separation Methods and Chemometrics. 2013.

151. **Natalja Kabanova**. Development of a Microcalorimetric Method for the Study of Fermentation Processes. 2013.

152. **Himani Khanduri**. Magnetic Properties of Functional Oxides. 2013.

153. **Julia Smirnova**. Investigation of Properties and Reaction Mechanisms of Redox-Active Proteins by ESI MS. 2013.

154. **Mervi Sepp**. Estimation of Diffusion Restrictions in Cardiomyocytes Using Kinetic Measurements. 2013.

155. **Kersti Jääger**. Differentiation and Heterogeneity of Mesenchymal Stem Cells. 2013.

156. **Victor Alari**. Multi-Scale Wind Wave Modeling in the Baltic Sea. 2013.

157. **Taavi Päll**. Studies of CD44 Hyaluronan Binding Domain as Novel Angiogenesis Inhibitor. 2013.

158. **Allan Niidu**. Synthesis of Cyclopentane and Tetrahydrofuran Derivatives. 2013.

159. **Julia Geller**. Detection and Genetic Characterization of *Borrelia* Species Circulating in Tick Population in Estonia. 2013.

160. **Irina Stulova**. The Effects of Milk Composition and Treatment on the Growth of Lactic Acid Bacteria. 2013.

161. **Jana Holmar**. Optical Method for Uric Acid Removal Assessment During Dialysis. 2013.

162. **Kerti Ausmees**. Synthesis of Heterobicyclo[3.2.0]heptane Derivatives *via* Multicomponent Cascade Reaction. 2013.

163. **Minna Varikmaa**. Structural and Functional Studies of Mitochondrial Respiration Regulation in Muscle Cells. 2013.

164. **Indrek Koppel**. Transcriptional Mechanisms of BDNF Gene Regulation. 2014.

165. **Kristjan Pilt**. Optical Pulse Wave Signal Analysis for Determination of Early Arterial Ageing in Diabetic Patients. 2014.

166. **Andres Anier**. Estimation of the Complexity of the Electroencephalogram for Brain Monitoring in Intensive Care. 2014.
167. **Toivo Kallaste**. Pyroclastic Sanidine in the Lower Palaeozoic Bentonites – A Tool for Regional Geological Correlations. 2014.
168. **Erki Kärber**. Properties of ZnO-nanorod/In_2S_3/$CuInS_2$ Solar Cell and the Constituent Layers Deposited by Chemical Spray Method. 2014.
169. **Julia Lehner**. Formation of Cu_2ZnSnS_4 and $Cu_2ZnSnSe_4$ by Chalcogenisation of Electrochemically Deposited Precursor Layers. 2014.
170. **Peep Pitk**. Protein- and Lipid-rich Solid Slaughterhouse Waste Anaerobic Co-digestion: Resource Analysis and Process Optimization. 2014.
171. **Kaspar Valgepea**. Absolute Quantitative Multi-omics Characterization of Specific Growth Rate-dependent Metabolism of *Escherichia coli*. 2014.
172. **Artur Noole**. Asymmetric Organocatalytic Synthesis of 3,3'-Disubstituted Oxindoles. 2014.
173. **Robert Tsanev**. Identification and Structure-Functional Characterisation of the Gene Transcriptional Repressor Domain of Human Gli Proteins. 2014.
174. **Dmitri Kartofelev**. Nonlinear Sound Generation Mechanisms in Musical Acoustic. 2014.
175. **Sigrid Hade**. GIS Applications in the Studies of the Palaeozoic Graptolite Argillite and Landscape Change. 2014.
176. **Agne Velthut-Meikas**. Ovarian Follicle as the Environment of Oocyte Maturation: The Role of Granulosa Cells and Follicular Fluid at Pre-Ovulatory Development. 2014.
177. **Kristel Hälvin**. Determination of B-group Vitamins in Food Using an LC-MS Stable Isotope Dilution Assay. 2014.
178. **Mailis Päri**. Characterization of the Oligoadenylate Synthetase Subgroup from Phylum Porifera. 2014.
179. **Jekaterina Kazantseva**. Alternative Splicing of *TAF4*: A Dynamic Switch between Distinct Cell Functions. 2014.
180. **Jaanus Suurväli**. Regulator of G Protein Signalling 16 (RGS16): Functions in Immunity and Genomic Location in an Ancient MHC-Related Evolutionarily Conserved Synteny Group. 2014.
181. **Ene Viiard**. Diversity and Stability of Lactic Acid Bacteria During Rye Sourdough Propagation. 2014.
182. **Kristella Hansen**. Prostaglandin Synthesis in Marine Arthropods and Red Algae. 2014.
183. **Helike Lõhelaid**. Allene Oxide Synthase-lipoxygenase Pathway in Coral Stress Response. 2015.
184. **Normunds Stivriņš**. Postglacial Environmental Conditions, Vegetation Succession and Human Impact in Latvia. 2015.
185. **Mary-Liis Kütt**. Identification and Characterization of Bioactive Peptides with Antimicrobial and Immunoregulating Properties Derived from Bovine Colostrum and Milk. 2015.
186. **Kazbulat Šogenov**. Petrophysical Models of the CO_2 Plume at Prospective Storage Sites in the Baltic Basin. 2015.

187. **Taavi Raadik**. Application of Modulation Spectroscopy Methods in Photovoltaic Materials Research. 2015.
188. **Reio Põder**. Study of Oxygen Vacancy Dynamics in Sc-doped Ceria with NMR Techniques. 2015.
189. **Sven Siir**. Internal Geochemical Stratification of Bentonites (Altered Volcanic Ash Beds) and its Interpretation. 2015.
190. **Kaur Jaanson**. Novel Transgenic Models Based on Bacterial Artificial Chromosomes for Studying BDNF Gene Regulation. 2015.
191. **Niina Karro**. Analysis of ADP Compartmentation in Cardiomyocytes and Its Role in Protection Against Mitochondrial Permeability Transition Pore Opening. 2015.
192. **Piret Laht**. B-plexins Regulate the Maturation of Neurons Through Microtubule Dynamics. 2015.
193. **Sergei Žari**. Organocatalytic Asymmetric Addition to Unsaturated 1,4-Dicarbonyl Compounds. 2015.
194. **Natalja Buhhalko**. Processes Influencing the Spatio-temporal Dynamics of Nutrients and Phytoplankton in Summer in the Gulf of Finland, Baltic Sea. 2015.
195. **Natalia Maticiuc**. Mechanism of Changes in the Properties of Chemically Deposited CdS Thin Films Induced by Thermal Annealing. 2015.